New Properties of Scalar-Field Dynamics in an Isotropic Cosmological Model on the Brane

A. V. Toporensky[*], P. V. Tret'yakov, and V. O. Ustiansky

Sternberg Astronomical Institute, Universitetskii pr. 13, Moscow, 119992 Russia
Received July 25, 2002

Abstract—We investigate some aspects of the scalar-field dynamics on the brane that differ from the corresponding regimes in standard cosmology. We consider asymptotic solutions near singularity, inflation and rebound conditions, and some features of chaos in the model on the brane. Our results are compared with their analogs in classical cosmology. © *2003 MAIK "Nauka/Interperiodica".*

Key words: *cosmology, scalar field, inflation, chaotic dynamics.*

INTRODUCTION

The idea that we live on a three-dimensional (mem)brane embedded in space with a larger number of dimensions has aroused considerable interest for the last several years. This idea has a long history of its own [see Visser (1985) and references therein] but it owes its recent revival to Randall and Sundrum (1999a, 1999b).

In such models, ordinary matter is confined to the brane, while gravity can pervade the entire space. Extra terms appear in the equations that describe effective four-dimensional gravity; they can play a significant role in cosmology (Binetruy 2000). Brane models predict an extra term on the right-hand sides of the effective Einstein equations that is quadratic in the energy−momentum tensor components, while there are only a linear term in standard general relativity. Another prediction is the existence of a nonlocal term that is the projection of the Weyl tensor onto the brane. For the Friedmann metric on the brane, it enters into the equation in the same manner as radiation. Therefore, despite its geometric nature, this term is occasionally called "dark radiation."

The dynamics of the Universe with hydrodynamic matter on the brane has been the subject of intensive studies in the last three years (see, e.g., Maartens 2000; Campos and Sopuerta 2001a, 2001b). These studies revealed new regimes that were not typical of standard cosmology, such as stable oscillations (Campos and Sopuerta 2001b), the collapse of a flat Universe (Santos *et al.* 2001), the growth of anisotropy in a Bianchi type-I Universe (Toporensky 2001), and an unusual analog of the Einstein static Universe (Gergely and Maartens 2002).

[*]E-mail: lesha@sai.msu.ru

The dynamics in the model with a scalar field is complex even in standard cosmology (Starobinsky 1978). Thus, it comes as no surprise that new interesting dynamical regimes arise on the brane. Some inflation features on the brane were investigated by Maartens *et al.* (2000, 2001) and Copeland *et al.* (2001). The dynamics with exponential scalar-field potentials was described by Mizumo *et al.* (2002) and Goheer and Dunsby (2002). Presently, the scalar-field dynamics on the brane continues to draw considerable attention.

Here, we describe how some well-known regimes of standard cosmology change for the model on the brane. We consider effective four-dimensional cosmological models with the Friedmann metric on the brane with a scalar field φ with potential $V(\varphi)$. Features related to the presence of a quadratic term in the Einstein equations are investigated in the section entitled Dynamics on the Brane at High Energies. Some of the dynamical features related to dark radiation when this term enters into the equations with a negative sign are considered in the section entitled Effects Related to Dark Radiation.

DYNAMICS ON THE BRANE AT HIGH ENERGIES

The effective four-dimensional equations of motion [in this form, they can be easily derived from the equations presented in Binetruy *et al.* (2000)] are

$$\frac{\dot{a}^2}{a^2} + \frac{k}{a^2} = \frac{\tilde{\kappa}^2}{3}\left(\frac{1}{2}\dot{\varphi}^2 + V\right) \qquad (1)$$

$$+ \frac{\kappa^4}{36}\left(\frac{1}{2}\dot{\varphi}^2 + V\right)^2 + \frac{C}{a^4},$$

$$\frac{\ddot{a}}{a} + \frac{2\dot{a}^2}{a^2} + \frac{2k}{a^2} = \tilde{\kappa}^2 V + \frac{\kappa^4}{48}(4V^2 - \dot{\varphi}^4) + \frac{C}{a^4}, \quad (2)$$

$$\ddot{\varphi} = -3\frac{\dot{a}}{a}\dot{\varphi} - V', \quad (3)$$

where the dot and prime denote differentiation with respect to time and φ, respectively; $\tilde{\kappa}^2 = 8\pi/M_{(4)}^2$; and $\kappa^2 = 8\pi/M_{(5)}^3$. Here, $M_{(5)}$ is the fundamental five-dimensional Planck mass and $M_{(4)}$ is the effective four-dimensional Planck mass on the brane. The latter is related to $M_{(5)}$ and to the brane tension λ by (Maartens *et al.* 2000)

$$M_{(4)} = \sqrt{\frac{3}{4\pi}} \left(\frac{M_{(5)}^2}{\sqrt{\lambda}}\right) M_{(5)}. \quad (4)$$

The brane tension λ must be positive in order that the gravity on the brane have the correct sign. The dark-radiation constant C can be positive and negative.

A distinctive feature of Eq. (1) is the presence of a term quadratic in the scalar-field energy density. The contribution of this term must be small at low energies in order to be consistent with the standard cosmological scenario (Cline *et al.* 1999; Binetruy *et al.* 2000), but this term dominates at high energies. Therefore, let us consider the system of equations (1)–(3) in the high-energy approximation. Recall that the scalar-field dynamics significantly depends on whether the Universe is in a contraction or an expansion stage. In the standard cosmological scenario (in the standard case, we use the system of quantities $M_{(4)}/\sqrt{8\pi} = 1$, while in the nonstandard case, we explicitly write out all dimensional parameters), if the scalar-field potential $V(\varphi)$ at the contraction stage increases more slowly than $V(\varphi) \sim \exp\sqrt{6}\varphi$, then we have the same regime as that for $V(\varphi) = 0$. In this regime, $a(t) \sim t^{1/3}$ and the scalar field diverges as $\varphi(t) \sim t^{-1}$ (Starobinsky 1978). For a steeper potential, scalar-field oscillations arise; the field itself also diverges (Foster 1998).

This pattern significantly changes in the scenario on the brane. Indeed, for $V(\varphi) = 0$, substituting

$$a = At^\alpha, \qquad \varphi = Bt^\beta + \varphi_0$$

into the equations of motion yields the solution

$$a(t) = At^{1/6}, \qquad \varphi(t) = \pm\frac{M_{(5)}^{3/2}}{\sqrt{2\pi}}t^{1/2} + \varphi_0, \quad (5)$$

$$t \to 0,$$

where $A > 0$ and φ_0 are the integration constants. The salient feature of this solution is that the scalar field tends to a constant, while in standard cosmology $\varphi \to \infty$. Although the scalar field remains finite, its derivative diverges. This divergence leads to the equation of state $p = \varepsilon$, as in the case of standard cosmology. On the other hand, since φ remains finite, while $\dot{\varphi} \to \infty$, the kinetic energy of the scalar field always dominates over its potential energy during the contraction near singularity and asymptotics (5) is valid for an arbitrary $V(\varphi)$.

Consider the opposite regime—inflation. Here, one of the problems is the steepness of the scalar-field potential $V(\varphi)$ at which the inflation stage can exist. At this stage, we can disregard spatial curvature and dark radiation in the equations of motion.

The equations for the two slow-roll parameters can be written as [in the limit of high energies; see Maartens *et al.* (2000) for a general form]

$$\epsilon \simeq \frac{3M_{(5)}^6}{16V\pi^2}\left(\frac{V'}{V}\right)^2 \quad (6)$$

and

$$\eta \simeq \frac{3M_{(5)}^6}{16V\pi^2}\left(\frac{V''}{V}\right), \quad (7)$$

where $\simeq$ means equality in the slow-roll approximation. The inflation condition is $|\max(\epsilon, \eta)| < 1$. In standard cosmology, this condition is violated for potentials that increase faster than $V(\varphi) \sim e^{\sqrt{2}\varphi}$. In our case, this condition can be violated only for potentials that increase faster than

$$V(\varphi) \sim (\varphi - \varphi_0)^{-2};$$

in the boundary case

$$V(\varphi) = A/(\varphi - \varphi_0)^2,$$

the condition $|\max(\epsilon, \eta)| < 1$ is violated at $A < 9M_{(5)}^6/(8\pi^2)$.

Thus, for the brane, inflation imposes less stringent conditions on the rate of increase in potential than it does in the standard case, admitting a potential in the form of an infinitely high wall.

The nonstandard dependence in the equations of motion on the energy–momentum tensor components of matter also causes the condition for the existence of chaos to change. In standard cosmology, the dynamics of the closed model ($k = +1$) is chaotic for a broad class of potentials $V(\varphi)$ (Cornish and Shellard 1998; Kamenshchik *et al.* 1997). In this case, the behavior of an arbitrary trajectory appears as follows. Without loss of generality, we can set the initial value of $\dot{a}$ equal to zero. The initial value of $\dot{\varphi}$ can be obtained from Eq. (1). Thus, we have the two-dimensional space of initial values. Numerical calculations indicate that, starting from certain regions in the space of initial values, the phase trajectory can either go to singularity or pass through a local

minimum of the scale factor (this behavior is called a rebound). In the latter case, the scale factor then necessarily passes through a local maximum and we will return to the original picture with two possible outcomes. There is a set of trajectories that undergo an infinite number of rebounds, but the measure of this set is equal to zero.

In the (a, φ) plane, the region where the scale factor can have an extremum is defined by the inequality that follows from Eq. (1):

$$V(\varphi) \leq \frac{3M_{(5)}^3}{4\pi a^2} \left(1 - \frac{C}{a^2}\right). \tag{8}$$

Recall that in standard cosmology, chaos can disappear for exponential or steeper potentials. Toporensky (1999) developed an analytic approach to this problem. It was shown that a simple necessary condition for the existence of chaos can be written using the following two facts established during numerical experiments:

(i) all simple periodic trajectories contain a point at which $\dot{\varphi} = 0$ and $\dot{a} = 0$ located at the boundary of the region defined by inequality (8),

(ii) all the trajectories that have a velocity vector directed inward into region (8) at this point go to singularity and, hence, cannot be periodic.

These two facts can be violated in the so-called strong-chaos regime. However, this regime exists only for much more gently sloping potentials than a quadratic potential (Pavluchenko and Toporensky 2000). Thus, we can use them for sufficiently steep potentials when chaos is on the verge of disappearance.

Let us apply the methods described in Toporensky (1999) to the case on the brane. First, we set $C = 0$. The trajectory with $\dot{\varphi} = 0$ and $\dot{a} = 0$ is directed outward from region (8) if

$$\left|\frac{\ddot{a}}{\ddot{\varphi}}\right| > \left|\frac{da(\varphi)}{d\varphi}\right|, \tag{9}$$

where $a(\varphi)$ is the boundary equation. Substituting $\ddot{a}$ and $\ddot{\varphi}$ from Eqs. (2) and (3) and using (1), we can write this condition as

$$\frac{\kappa^4}{36} V(\varphi)^3 > \left(\frac{dV(\varphi)}{d\varphi}\right)^2. \tag{10}$$

If this condition is violated for all φ, then chaos disappears. This condition is valid for exponential potentials at sufficiently large φ. Moreover, it is also valid for potentials $V \sim \exp(\varphi^2)$. Thus, chaos on the brane can exist for much steeper potentials than those in standard cosmology.

Potentials that violate condition (10) must be in the form of a potential wall. The critical case is

$$V(\varphi) = \frac{A}{(\varphi - \varphi_0)^2}. \tag{11}$$

In this case, as can be easily seen from (10), this condition is violated at any φ for $A < 9M_{(5)}^6/(4\pi^2)$. Our numerical calculations confirm that there is no chaos in this case.

The same analysis can be performed for nonzero C, although the corresponding equations are not so simple. A general property is that positive C make the condition for the existence of chaos more stringent, while negative C relax it. In the limit $C \to -\infty$, we can write a simple analog of (10)

$$\frac{\kappa^4}{9} V(\varphi)^3 > \left(\frac{dV(\varphi)}{d\varphi}\right)^2, \tag{12}$$

which leads to a potential of the form (11) for $A = 9M_{(5)}^6/(16\pi^2)$ in the boundary case.

We summarize our results as follows. In standard cosmology, the scalar-field dynamics is known to significantly differ for potentials that increase more slowly and faster than an exponential. For sufficiently steep potentials, inflation cannot take place, chaos disappears for a positive spatial curvature, and scalar-field oscillations with an increasing amplitude arise during the contraction to singularity. There is no analog of the latter on the brane—the scalar field does not diverge at the contraction stage, irrespective of the potential. However, the first two of the above features also have their analogs on the brane. The boundary potential that separates dynamically distinct cases (similar to an exponential potential in classical cosmology) is a wall-type potential of the form $V(\varphi) \sim 1/(\varphi - \varphi_0)^2$.

EFFECTS RELATED TO DARK RADIATION

Let us consider the effects related to dark radiation. An important feature of dark radiation is that the constant C can be both positive and negative. For negative C, the behavior of the scale factor can be nonmonotonic not only for a positive spatial curvature, but also for a zero and negative curvature. Indeed, as we can see from Eqs. (1)–(3), the terms containing C for $C < 0$ give a contribution of the same sign as a positive curvature. In particular, this gives rise to rebounds in a flat and an open Universe. Moreover, the probability of a rebound increases with $|C|$ and can become significant.

To illustrate the latter assertion, we numerically integrated system (1)–(3) in nonstandard regime ($\rho \gg \lambda$) at the contraction stage starting from a fixed
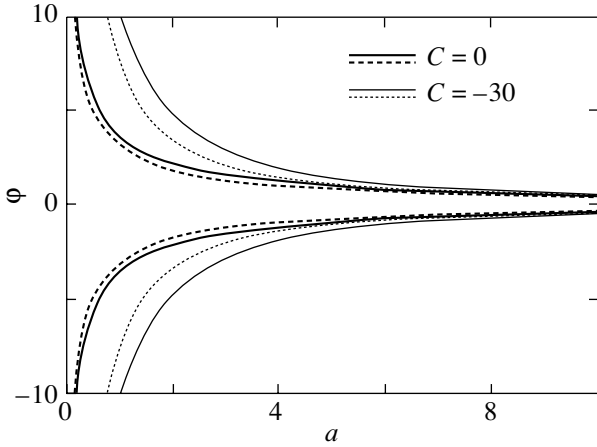
Fig. 1. The region in which the scale factor of a closed Universe can have an extremum is bounded by two solid lines and, for minima, by solid and dashed lines.

Fig. 2. The $\varphi = 0$ section of the space of initial values for various values of C. The initial values at which a rebound occurs are painted black.

initial scale factor. In our numerical calculations, we set $\kappa = 1$. An individual trajectory is defined by specifying two initial values, the scalar field and its derivative. At fixed initial values of φ and $\dot{\varphi}$, the initial value of $\dot{a}$ can be determined from Eq. (1). We investigated a compact region in the plane of initial $(\varphi, \dot{\varphi})$ that satisfied Eq. (1) and the inequality

$$\frac{m^2\varphi^2}{2} + \frac{\dot{\varphi}^2}{2} < 1.$$

Introducing a uniform measure on this compact set of initial conditions, we obtained the following results. For the first set of rebound probabilities P, the scalar-field mass was chosen to be 0.1. Since C and a for a flat Universe enter the equations only in the combination C/a^4, our results are virtually independent of the specific initial scale factor.

C/a^4	-10^{-5}	$-10^{-4.5}$	-10^{-4}	-10^{-3}	-10^{-2}
P	7.4×10^{-4}	2.0×10^{-3}	5.6×10^{-3}	9.2×10^{-2}	3.4×10^{-1}

The dependence of the rebound probability on scalar-field mass m is complex but vanishes for low masses. In this situation, P values for different C and low m ($m < 10^{-3}$) are given below:

C/a^4	-10^{-4}	-10^{-3}	-10^{-2}
P	0.029	0.072	0.195

The transition from the contraction of a flat Universe to its expansion is possible only if there are terms with a negative contribution to the energy in Eq. (1). Cosmology on the brane gives a simple example of this kind. Our numerical calculations indicate that the measure of the initial values that lead to a rebound can be significant at large $|C|$.

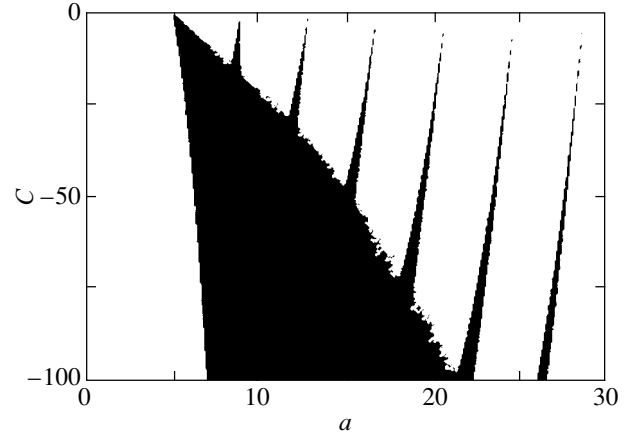For a positive curvature, the dynamics on the brane is more complex. The region in which the scale factor can have extrema shrinks for positive C and chaos disappears for sufficiently large C. The dynamical picture is similar to the picture that arises in standard cosmology in the presence of hydrodynamic matter with the equation of state $p = \epsilon/3$ (Kamenshchik *et al.* 1999). Negative C (in this case, there is no direct analogy with standard cosmology) act in the opposite direction: the region where the scale factor can have extrema grows with absolute value of C and, as we will see below, the chaotic properties of the cosmological dynamics are enhanced. In Fig. 1, the region in which the scale factor can have extrema is bounded by two solid lines, while the region in which the scale factor can have a minimum is bounded by solid and dashed lines. In this figure, the scalar-field potential was chosen in the form $V(\varphi) = m^2\varphi^2/2$, where $m = 0.5$ and the brane tension $\lambda = 1$ (we returned to the units $M_{(4)}/\sqrt{8\pi} = 1$). The thick and thin lines correspond to $C = 0$ and $C = -30$, respectively.

Let us consider the interesting transformation of chaotic dynamics that occurs in standard regime ($\rho \ll \lambda$). Below, we consider a scalar potential in the form $V(\varphi) = m^2\varphi^2/2$. For $C = 0$, the initial values that lead to a rebound form a set of narrow regions separated by wide regions in which the solution is singular. This pattern significantly changes as $|C|$ increases. In Fig. 2, we set the initial value of φ equal to zero and $m = 0.5$. We varied C and a over the ranges from -100 to 0 and from 1 to 30, respectively. The region painted black corresponds to the initial conditions that lead to a rebound at the initial $\dot{a} = 0$, while white corresponds to singular solutions. As we can see, the ranges of initial scale factors that lead to a rebound broaden with increasing absolute value of C and the first two ranges merge for $C \approx -15$.

The solutions that start in the merging region are strongly chaotic. Such solutions can oscillate over a long period, without leaving the region of large spatial curvatures. As the absolute value of C increases further, we observe a successive merging of the ranges and a monotonic increase in the fraction of the initial values that lead to a rebound.

This pattern of strong chaos is similar to the pattern that has been found previously in standard cosmology with a gently sloping potential (Pavluchenko and Toporensky 2000) and in cosmologies that include second-order curvature string corrections (Alexeyev *et al.* 2000). In the scenario on the brane, this effect shows up even for the simplest potential $m^2\varphi^2/2$. Interestingly, in nonstandard regime ($\rho \gg \lambda$), this strong chaos exists only for potentials that increase much more slowly than a quadratic potential.

ACKNOWLEDGMENTS

REFERENCES

1. S. O. Alexeyev, A. V. Toporensky, and V. O. Ustiansky, Class. Quantum Grav. **17**, 2243 (2000).
2. P. Binetruy, C. Deffayet, U. Ellwanger, and D. Langlois, Phys. Lett. B **477**, 285 (2000).
3. A. Campos and C. F. Sopuerta, Phys. Rev. D **63**, 104012 (2001a).
4. A. Campos and C. F. Sopuerta, Phys. Rev. D **64**, 104011 (2001b).
5. J. M. Cline, C. Grojean, and G. Servant, Phys. Rev. Lett. **83**, 4245 (1999).
6. E. J. Copeland, A. R. Liddle, and J. E. Lidsey, Phys. Rev. D **64**, 023509 (2001).
7. N. J. Cornish and E. P. Shellard, Phys. Rev. Lett. **81**, 3571 (1998).
8. S. Foster, gr-qc/9806113 (1998).
9. L. Gergely and R. Maartens, Class. Quantum Grav. **19**, 213 (2002).
10. N. Goheer and P. Dunsby, gr-qc/0204059 (2002).
11. A. Yu. Kamenshchik, I. M. Khalatnikov, and A. V. Toporensky, Int. J. Mod. Phys. D **6**, 673 (1997).
12. A. Yu. Kamenshchik, I. M. Khalatnikov, S. V. Savchenko, and A. V. Toporensky, Phys. Rev. D **59**, 123516 (1999).
13. R. Maartens, Phys. Rev. D **62**, 084023 (2000).
14. R. Maartens, D. Wands, B. A. Bassett, and I. Heard, Phys. Rev. D **62**, 041301 (2000).
15. R. Maartens, V. Sahni, and T. D. Saini, Phys. Rev. D **63**, 063509 (2001).
16. S. Mizumo, K.-I. Maeda, and K. Yamamoto, hep-ph/0205292 (2002).
17. S. A. Pavluchenko and A. V. Toporensky, Grav. Cosmol. **6**, 241 (2000).
18. L. J. Randall and R. Sundrum, Phys. Rev. Lett. **83**, 3370 (1999a).
19. L. J. Randall and R. Sundrum, Phys. Rev. Lett. **83**, 4690 (1999b).
20. M. G. Santos, F. Vernizzi, and P. G. Ferreira, Phys. Rev. D **64**, 063506 (2001).
21. A. A. Starobinsky, Pis'ma Astron. Zh. **4**, 155 (1978) [Sov. Astron. Lett. **4**, 82 (1978)].
22. A. V. Toporensky, Int. J. Mod. Phys. D **8**, 739 (1999).
23. A. V. Toporensky, Class. Quantum Grav. **18**, 2311 (2001).
24. M. Visser, Phys. Lett. B **159B**, 22 (1985).

Translated by V. Astakhov

Effects of Boundary Conditions and Viscous Energy Dissipation on Carbon Burning in Thermonuclear Supernova Models

N. V. Dunina-Barkovskaya* and V. S. Imshennik

Institute of Theoretical and Experimental Physics,
ul. Bol'shaya Cheremushkinskaya 25, Moscow, 117259 Russia
Received August 12, 2002

Abstract—Based on a one-dimensional hydrodynamic model, we investigate carbon burning in a thermonuclear type-Ia supernova in the approximation of unsteady convection. The relatively broad range of convective parameters, $1 \times 10^{-3} \leq \alpha_c \leq 2 \times 10^{-3}$, in which delayed detonation from the edge takes place was found to be preserved only for cases with a low boundary temperature at the presupernova stage, $T_b^{(PS)} = 6.4 \times 10^6$ K, and with a high envelope mass, $m_{ex} \simeq 2 \times 10^{-3} M_\odot$. In cases with a more realistic temperature, $T_b^{(PS)} = 2 \times 10^8$ K, which corresponds to helium burning in the shell source, and with a lower mass m_{ex}, delayed detonation from the edge takes place only at $\alpha_c = 2 \times 10^{-3}$, while at $\alpha_c = 1 \times 10^{-3}$, numerous model pulsations occur during $t \gtrsim 500$ s. Artificial viscosity is shown to give a determining contribution to the increase in entropy in outer model shells, which is caused by the generation of weak shock waves during pulsations. We also show that the entropies calculated by two independent methods are equal. © *2003 MAIK "Nauka/Interperiodica"*.

Key words: *supernovae and supernova remnants; plasma astrophysics, hydrodynamics, and shock waves; detonation and deflagration.*

INTRODUCTION

Recently, because of the progress made in modeling the light curves of type-Ia supernovae (Sorokina *et al.* 2000), a demand has arisen for new supernova models that could explain isolated events with a large ^{56}Ni mass (Cappellaro *et al.* 1997). The model with delayed detonation from the edge described (for various boundary conditions) previously (Dunina-Barkovskaya *et al.* 2001; Dunina-Barkovskaya and Imshennik 2000) could presumably be such a model. Nevertheless, it is first necessary to analyze the dependence of this burning regime on model boundary conditions and on the parameter of artificial viscosity. The latter describes shock-front smearing and also affects the increase in entropy in the outer layers of a carbon−oxygen core as weak shock waves propagate in them. This is the goal of our study. Concurrently, we justify our previous results (Dunina-Barkovskaya *et al.* 2001) regarding the increase in entropy in the near-surface layers of a carbon−oxygen core during a supernova explosion through additional calculations of the equation for entropy production.

*E-mail: `dunina@vitep1.itep.ru`

BASIC EQUATIONS FOR THE CONVECTIVE HYDRODYNAMIC MODEL

As in our previous studies, we calculated the evolution of a presupernova and supernova explosion by solving the system of hydrodynamic equations

$$\frac{\partial r}{\partial t} = v, \tag{1}$$

$$\frac{\partial v}{\partial t} = -\frac{Gm}{r^2} - 4\pi r^2 \frac{\partial (P + Q)}{\partial m}, \tag{2}$$

$$\frac{\partial T}{\partial t} = \left[\varepsilon_{\text{nucl}} - \varepsilon_\nu - \frac{4\pi \partial (r^2 F_{\text{conv}})}{\partial m} - \frac{4\pi \partial (r^2 F_{\text{rad}})}{\partial m} - 4\pi \frac{\partial (r^2 v)}{\partial m} (T(\partial P / \partial T)_\rho + Q) \right] / (\partial E / \partial T)_\rho, \tag{3}$$

$$\frac{\partial X_C}{\partial t} = -X_C^2 r_{CC} + \left(\frac{\partial X_C}{\partial t} \right)_{\text{conv}}, \tag{4}$$

$$\frac{\partial u_c}{\partial t} = \frac{2(v_c^2 - u_c^2)}{l_{\text{mix}}}, \tag{5}$$

where X_C is the mass fraction of ^{12}C; u_c is the velocity of unsteady convection; ε_{nucl} is the specific energy release through nuclear burning (corrected for carbon burning, as was done by Dunina-Barkovskaya *et al.* 2001); r_{CC} is the specific rate of carbon burning, which is uniquely related to ε_{nucl}; ε_ν are the standard neutrino energy losses (from the formulas of Schinder *et al.* 1987); l_{mix}, v_c, and F_{conv} are, respectively, the mixing length, the velocity of steady convection, and the convective energy flux density (see Bisnovatyǐ-Kogan 1989); and Q is the momentum flux density due to quadratic scalar artificial viscosity. The latter is defined in our calculations by the expression

$$Q = A_q \rho \left(\Delta r_i \frac{1}{r^2} \frac{\partial (r^2 v)}{\partial r} \right)^2 \text{ for } \frac{\partial (r^2 v)}{\partial r} < 0, \quad (6)$$

$$Q = 0 \quad \text{for} \quad \frac{\partial (r^2 v)}{\partial r} > 0, \quad (7)$$

where Δr_i is the (radial) thickness of the ith mass zone and the square root of the dimensionless positive coefficient A_q (of the order of unity) gives the number of zones over which the shock front was smeared. Because of condition (7), viscous energy dissipation is possible only in compression shocks (Landau and Lifshitz 1954).

Equation (3) also includes F_{rad}, the energy flux density due to electron and radiative heat conduction. In all but the last zone, it is defined by

$$F_{rad} = -\frac{4\pi a c r^2}{3\kappa} \frac{\partial T^4}{\partial m}. \quad (8)$$

Here, κ is the opacity due to electron and radiative heat conduction in the inner and outer model layers, respectively. In the last zone (for models with a variable boundary temperature), we use the gray-atmosphere approximation (see Bisnovatyi-Kogan 1989) for F_{rad}:

$$F_{rad} = \frac{a c T^4}{2 + 3\tau}, \quad (9)$$

where τ is the optical depth estimated below. This boundary condition closely corresponds to the so-called mixed boundary condition in the radiation hydrodynamics of supernovae at $\tau = 2/3$ [see Imshennik and Nadyozhin (1982) for a review]. However, in our calculations, τ can be large ($\tau \gg 1$).

Note that in Eq. (3), the expression for the term attributable to gravitational contraction (Dunina-Barkovskaya *et al.* 2000) is written explicitly:

$$\varepsilon_g = -4\pi \frac{\partial (r^2 v)}{\partial m} T \left(\frac{\partial P}{\partial T} \right)_\rho.$$

We emphasize that this expression differs from the standard expression for the energy release through gravitational contraction

$$\varepsilon_{gr} = -\left(\frac{\partial E}{\partial t} - \frac{P}{\rho^2} \frac{\partial \rho}{\partial t} \right) = \varepsilon_g - \left(\frac{\partial E}{\partial T} \right)_\rho \frac{\partial T}{\partial t}$$

(Schwarzschild 1958).

To independently control the increase in entropy in our numerical solution, we added the equation for entropy production to system (1)–(5). It is essentially equivalent to the equation for the change in temperature (3), according to the thermodynamic identity

$$\frac{\partial S_{test}}{\partial t} = \frac{1}{T} \left[\varepsilon_{nucl} - \varepsilon_\nu - \frac{4\pi \partial (r^2 F_{conv})}{\partial m} \right. \quad (10)$$
$$\left. - \frac{4\pi \partial (r^2 F_{rad})}{\partial m} - 4\pi Q \frac{\partial (r^2 v)}{\partial m} \right].$$

Our calculations must show a close match between the entropy from Eq. (10) and its value from the equation of state (Ivanova *et al.* 1977). Equation (10) explicitly contains the term of viscous energy dissipation at the shock fronts, including weak compression shock waves.

THE DEVELOPMENT OF A CONVECTIVE CORE AT THE PRESUPERNOVA STAGE

Here, we retain the same rate of increase in the CO-core mass, $\dot{M} = 5 \times 10^{-7} M_\odot \text{ yr}^{-1}$, as that in Dunina-Barkovskaya *et al.* (2001). The following considerations can be added to arguments for this choice of $\dot{M}$ by using data from the review article by Arkhipova (1996) on novae. Thermonuclear models for nova outbursts (see, in particular, Kovetz and Prialnik 1994) lead one to conclude that at $\dot{M} \gtrsim 10^{-7} M_\odot \text{ yr}^{-1}$ no shell ejection takes place but a sub-Chandrasekhar type-Ia SN is formed. In contrast, the model of recurrent nova-type explosions is realized at $\dot{M} < 10^{-7} M_\odot \text{ yr}^{-1}$. These results refer to the accretion of matter with normal chemical composition, i.e., in the presence of hydrogen. For a purely helium accretor (or the companion of a CO core in a binary), Cassisi *et al.* (1998) showed that in a wide $\dot{M}$ range ($10^{-8} M_\odot \text{ yr}^{-1} < \dot{M} < 10^{-6} M_\odot \text{ yr}^{-1}$), the helium layer on a cool CO core can be lost. However, the latter conclusion, according to Yungelson (1998), needs to be verified by a hydrodynamic accretion model. Nevertheless, the chosen value of $\dot{M} = 5 \times 10^{-7} M_\odot \text{ yr}^{-1}$ lies almost outside this $\dot{M}$ range, especially since it satisfies the criterion of Kovetz and Prialnik mentioned above. There is a certain relationship between the models of nova and type-Ia supernova progenitors considered in this

Table 1. Parameters of presupernova models

Model	$\alpha_c, 10^{-3}$	$T_b^{(PS)}$, K	$M_{beg}, M_\odot$	q	N	$m_N, M_\odot$	N_{conv}	$m_{ex}, M_\odot$
H20−181	2.0	2.0×10^8	1.341	0.9324	181	1.36806	87	1.02×10^{-4}
H20−180	2.0	2.0×10^8	1.341	0.9324	180	1.36781	87	3.27×10^{-4}
L20−188	2.0	6.4×10^6	1.335	0.9363	188	1.36762	100	5.58×10^{-5}
L20−180	2.0	6.4×10^6	1.335	0.9363	180	1.36560	100	1.85×10^{-3}
H10−180	1.0	2.0×10^8	1.341	0.9324	180	1.36781	79	3.24×10^{-4}
H10−174	1.0	2.0×10^8	1.341	0.9324	174	1.36586	79	2.02×10^{-3}
L10−188	1.0	6.4×10^6	1.335	0.9363	188	1.36762	100	5.16×10^{-5}
L10−180	1.0	6.4×10^6	1.335	0.9363	180	1.36560	100	1.85×10^{-3}

paper. Note that the mass included in the nonzero boundary condition of the latter, $\Delta M \simeq 3 \times 10^{-3} M_\odot$ [in Dunina-Barkovskaya *et al.* (2001), it was $\Delta M = 2.34 \times 10^{-3} M_\odot$], is close in magnitude to the characteristic mass of ejected nova shells, $\Delta M_{cr} \simeq 10^{30}$ g $\simeq 10^{-3} M_\odot$ (Gorbatskiĭ 1986).

Since the difference models under consideration use mass (Lagrangian) coordinates and take into account mass accretion at the presupernova stage, it would be methodologically appropriate to introduce a nonzero boundary pressure (Dunina-Barkovskaya *et al.* 2001). Clearly, the initial Lagrangian grid is retained in this case. As for the boundary temperature, whose specification is dictated by the parabolic type of Eq. (3), we could just set it equal to a constant. Dunina-Barkovskaya *et al.* (2001) chose the temperature in the last zone to be low, 1.05×10^7 K. This virtually zero boundary temperature was assumed to be constant even during large model pulsations at the explosion stage. However, it would probably be more precise to assume it to be equal to $\sim 2 \times 10^8$ K, because accreted helium [see the evolutionary scenario 2 in Yungelson (1998)] on the surface of a CO core must burn through the Salpeter triple reaction (Frank-Kamenetskiĭ 1959) at exactly this temperature.[1] Such a temperature can even give rise to a positive entropy gradient; i.e., it can restrict the growth of a convective core at the presupernova stage.

Figure 1 shows the temperature distribution in mass at the onset of a supernova explosion (at $T_c = 5 \times 10^9$ K) for the main model H20−180 with $\alpha_c = 2 \times 10^{-3}$ and $T_b = 2 \times 10^8$ K (see Table 1) and for L20−188 and H10−180; the latter differ from the main model by a lower boundary temperature ($T_b =$

6.4×10^6 K) and a smaller convective parameter ($\alpha_c = 1 \times 10^{-3}$), respectively. In the case with $T_b = 6.4 \times 10^6$ K, we had to artificially restrict the growth of convection by the maximum number of convection zones $N_{conv} = 100$ ($M_{conv} = 0.91 M_\odot$), because otherwise convection would grow in the outermost zones and the computational time would significantly increase. For H20−180, we obtained a similar value, $N_{conv} = 87$, because of a positive entropy gradient in the outer core layers. As a result, the temperature profiles in the first 87 mass zones (at $m < 0.8 M_\odot$) essentially coincide for the H20−180 and L20−188 models. For H10−180, however, the temperature profile in these zones lies slightly lower, but at the same time, it almost coincides with the temperature profile from H20−180 outside the convective core (at $m > 0.8 M_\odot$).

Thus, raising the constant boundary temperature T_b actually causes a significant reduction (almost by a factor of 2) in the mass of the convective core. Therefore, the entropy distribution in the outer zones without convection can dramatically change by the onset of explosion. This factor will affect the development of explosion, particularly in the regime of delayed detonation from the surface model layers concerned. Note that it seems appropriate to limit the number of convection zones to $N_{conv} = 100$ ($M_{conv} = 0.91 M_\odot$) if we specify a low boundary temperature, $T_b = 6.4 \times 10^6$ K.

THE DEVELOPMENT OF AN EXPLOSION UNDER A LOW BOUNDARY PRESSURE AND FOR A VARIABLE BOUNDARY TEMPERATURE

The boundary pressure at the explosion time can, in principle, be made extremely low by discretely adding increasingly shallow mass zones to the outer model layers. However, with the assumed uniform

---

[1] We are grateful to Prof. W. Hillebrandt for the remark on the refinement of the boundary temperature.
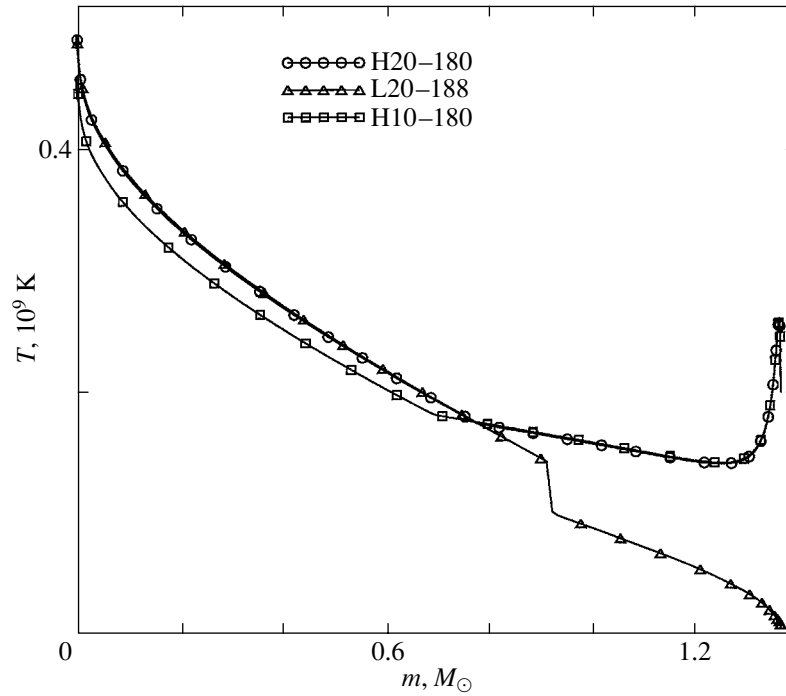
Fig. 1. Temperature profiles at the onset of the explosion ($T_c = 5 \times 10^9$ K) for H20−180, L20−188, and H10−180 from Table 1.
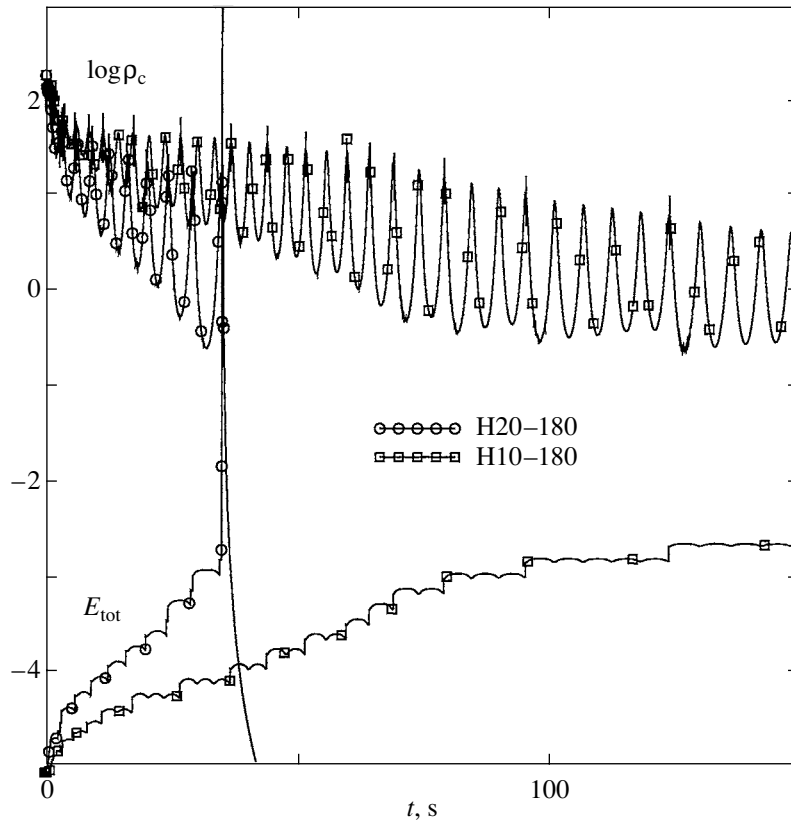

Fig. 2. Total energy (in 10^{50} erg) and logarithm of the central density (in 10^7 g cm^{-3}) versus time for H20−180 and H10−180 from Table 1.

Table 2. The development of a thermonuclear explosion for various presupernova models

Model	t_{expl}, s	n_{puls}	$E_{\text{tot}}^{(\text{max})}$, 10^{50} erg	$T_{\text{b}}^{(\text{end})}$, K	m_{defl}, $M_\odot$	m_{det}, $M_\odot$	N_{det}
H20−181	40.30	11	14.571	3.3×10^7	0.16655	1.3574	161
H20−180	34.99	10	14.627	4.6×10^7	0.15548	1.3609	165
L20−188	35.69	10	14.595	6.4×10^6	0.16523	1.3581	166
L20−180	19.72	7	14.678	6.4×10^6	0.09930	1.3653	179
H10−180	> 518	85	−1.826	1.3×10^6	0.21086	−	−
H10−174	> 543	84	−1.829	1.9×10^6	0.22193	−	−
L10−188	> 520	84	−1.832	6.4×10^6	0.22017	−	−
L10−180	30.90	11	14.664	6.4×10^6	0.07733	1.3653	179

decrease in the masses of the added Lagrangian zones (as a geometric progression), the boundary pressure cannot be made equal to zero, because it is not known in advance exactly at which time an explosion will occur. Here, for the initial model with a total number of zones equal to 150, a mass of $1.341M_\odot$, and a boundary temperature $T_{\text{b}}^{(\text{PS})} = 2.0 \times 10^8$ K, we used a geometric progression with the masses in the zones Δm_i decreasing from $1.1 \times 10^{-2} M_\odot$ to $2.2 \times 10^{-3} M_\odot$ for $127 \leq i \leq 150$. In our main H20−180 model, in the course of evolution with an accretion rate of $5 \times 10^{-7} M_\odot$ yr^{-1}, we added 30 zones to this model with the masses decreasing in the same geometric progression with the denominator $q = 0.9324$ (in the notation of this model, the letter "H" points to a high boundary temperature, 180 is the number of mass zones at the explosion time, and 20 is the value of α_c in units of 10^{-4}). As a result, the final model mass reached $M = 1.36781M_\odot$ and the conventional envelope mass m_{ex}, which is related to the external pressure P_{ex} by the relation from Dunina-Barkovskaya *et al.* (2001)

$$P_{\text{ex}} = \frac{GM}{4\pi R^4} m_{\text{ex}}, \qquad (11)$$

was $3.27 \times 10^{-4} M_\odot$. Relation (11) is inaccurate, because m_{ex} is only approximately equal to the actual envelope mass. In general, however, its accuracy increases with decreasing m_{ex}. Parameters of this and other models at the presupernova stage are given in Table 1. As was mentioned above, all models are arbitrarily defined at $T_\text{c} = 5 \times 10^9$ K, a necessary but not sufficient condition for the model explosion.

Figure 2 shows the development of the explosion for the H20−180 and H10−180 models with convective parameters α_c that differ by a factor of 2. In the case with $\alpha_\text{c} = 2 \times 10^{-3}$, delayed detonation or detonation from the edge took place rapidly (in 35 s). However, in the other case (as in the similar H10−174

model with a higher boundary pressure), the pulsations in our calculations lasted up to 500 s and no detonation took place in this time interval. For the H20−181 model, delayed detonation did take place (see Table 2), although m_{ex} decreased approximately by a factor of 3 (see below) compared to the H20−180 model.

For the models with a high presupernova boundary temperature ($T_{\text{b}}^{(\text{PS})} = 2.0 \times 10^8$ K), we were unable to keep this temperature constant during the entire process of pulsational deflagration. In this case, the density in the outer layers decreased to an extent that the radius of the last mass zone significantly (by several factors) exceeded the radius of the next-to-last zone. This made it impossible to properly work with the difference derivatives when solving system (1)−(5). Therefore, instead of setting the left-hand side of Eq. (3) equal to zero in the last zone, we used Eq. (9) for the flux in a gray atmosphere with the optical depth τ estimated from the formula

$$\tau = \frac{\kappa}{4\pi r_N^2} \frac{\Delta m_N + m_{\text{ex}}}{2}. \qquad (12)$$

In our case, condition (9) is, of course, cruder than that in models with a nearly zero boundary pressure and with a fine breakdown of the outer model layers in mass (Imshennik and Nadyozhin 1982). However, it still yields a reasonable final model boundary temperature $T_{\text{b}}^{(\text{end})}$ given in Table 2. This table also lists the other basic quantities that characterize the development of explosion for various initial models. The value of $T_{\text{b}}^{(\text{end})}$ is given at the onset of delayed detonation for the cases with such detonation and at the completion time of our calculations for the cases with a large number of pulsations. The value of t_{expl} from Table 2 shows the time in which the total energy of the model increased to zero through
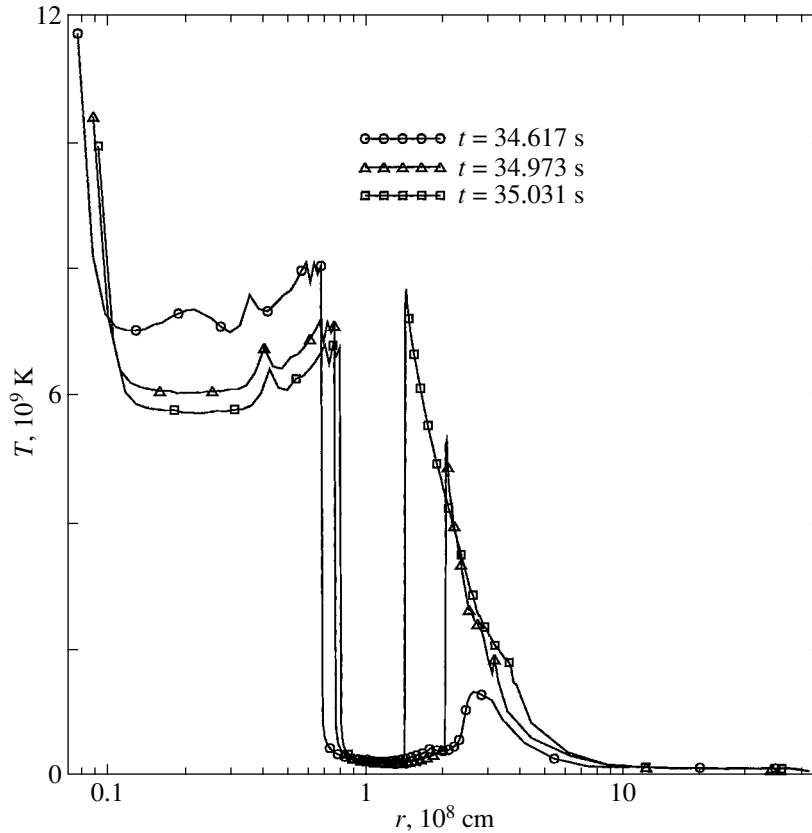
Fig. 3. The development of delayed detonation from the edge for H20−180.

carbon burning, i.e., the model became a gravitationally unbound system. In general, this occurs at the stage of detonation from the edge [except for the models with fast detonation described, e.g., by Dunina-Barkovskaya *et al.* (2001), in which $t_{\rm expl} <$ 1 s], $n_{\rm puls}$ is the number of pulsations (including the first decrease in density) occurred before detonation from the edge or before the completion of our calculations (in H10−180, H10−174, and L10−188). The maximum total energy $E_{\rm tot}^{(\max)}$ for all models is given at the completion time of our calculations. We also give the mass coordinate $m_{\rm defl}$ that was reached by the deflagration front propagating from the center for all models, the mass coordinate $m_{\rm det}$ from which the detonation front began to propagate inward for the models with delayed detonation, and the corresponding mass-zone number $N_{\rm det}$.

For the cases with a relatively high convective parameter, $\alpha_{\rm c} = 2 \times 10^{-3}$, delayed detonation in our calculations took place irrespective of the boundary temperature and boundary pressure. However, in contrast to Dunina-Barkovskaya *et al.* (2001) (where $m_{\rm ex} = 2.34 \times 10^{-3} M_{\odot}$ and $T_{\rm b} = 1.05 \times 10^7$ K), the $\alpha_{\rm c}$ range in which delayed detonation took place significantly narrowed. Of all the models with $\alpha_{\rm c} = 1 \times$

10^{-3}, only the L10−180 model with a low boundary temperature and a high boundary pressure exploded in this study, suggesting an important role of the boundary conditions in effecting this regime.

The development of delayed detonation from the edge for H20−180 is shown in Fig. 3. Although the mass zone 165 in which detonation begins is close to the edge in mass coordinate, a (radially) extended envelope lies behind it. During the development of detonation, i.e., before the collision of its front with an essentially static deflagration front (in $\Delta t \sim 0.4$ s), this envelope remains virtually static, which is in contrast to a similar plot from Dunina-Barkovskaya *et al.* (2001) where this envelope was mainly included (with $r > 4 \times 10^8$ cm) in the boundary condition for pressure. On the other hand, there is a close match between the physical conditions near the detonation front propagating into the presupernova in the calculations being compared.

THE ROLE OF VISCOUS ENERGY DISSIPATION IN THE DEVELOPMENT OF DETONATION FROM THE EDGE

The introduction of artificial viscosity is known (von Neuman and Richtmyer 1950) to be necessary to
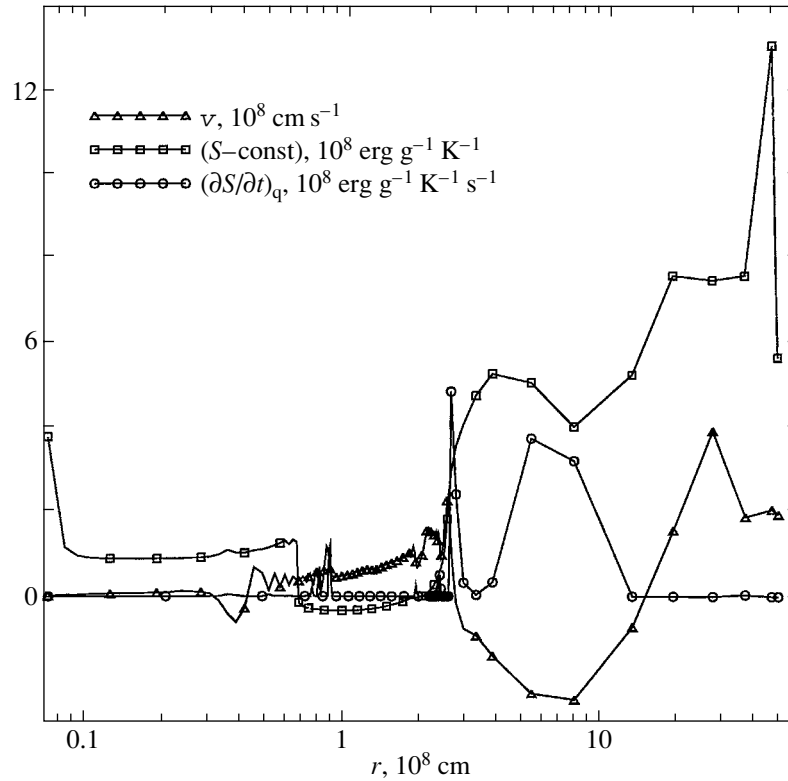
Fig. 4. The profiles of velocity, entropy, and $(\partial S/\partial t)_q$, which determines the contribution of artificial viscosity to the increase in entropy, for H20−180 at $t = 29.20$ s.

properly describe the energy dissipation inside shock fronts within a narrow range of thickness, which is determined in models by the spatial step of the difference grid, i.e., by Δr_i in expression (6). Actually, this range is determined by the physical viscosity. As is easy to show, being proportional to the particle (nuclides, electrons, photons) mean free path in the stellar matter of a CO core, the physical viscosity is extremely low. Nevertheless, the tensor properties of the viscosity effects, which are well known in the hydrodynamics of viscous fluids and gases (Landau and Lifshitz 1954), hold for such artificial viscosity. This viscosity is determined by analogy with volume physical viscosity. It can be shown that in the spherically symmetric (one-dimensional) case, only the diagonal components of the tensor σ'_{ik} of the latter are nonzero (for this reason, it is also called linear scalar viscosity):

$$\Pi = \sigma'_{rr} = \sigma'_{\theta\theta} = \sigma'_{\varphi\varphi} \tag{13}$$

$$= \eta \left(\frac{\partial v}{\partial r} + \frac{2v}{r} \right) = \eta \frac{1}{r^2} \frac{\partial}{\partial r}(r^2 v) = 4\pi\rho\eta \frac{\partial}{\partial m}(r^2 v),$$

where the tensor σ'_{ik} enters the right-hand side of the equation of motion as an addition to the scalar pressure $P\delta_{ik} - \sigma'_{ik}$ and η is the the volume viscosity coefficient, which below is assumed to be constant. Hence, based on tensor differentiation rules

(Kochin 1951), we derive an expression for the only nonzero radial component of the viscous force per unit mass:

$$\frac{1}{\rho}(\text{div}\sigma')_r = \left(\frac{\eta}{\rho} \right) \left(\frac{\partial^2 v}{\partial r^2} + \frac{2}{r} \frac{\partial v}{\partial r} - \frac{2v}{r^2} \right) \tag{14}$$

$$= \left(\frac{\eta}{\rho} \right) \frac{\partial}{\partial r} \left(\frac{\partial v}{\partial r} + \frac{2v}{r} \right).$$

The corresponding specific power of the viscous energy dissipation, which is generally given by $\Psi = [\text{div}(\sigma'\mathbf{v}) - (\mathbf{v} \times \text{div}\sigma')]/\rho$ (Landau and Lifshitz 1954), have the following expression, which is also derived according to tensor differentiation rules using (14):

$$\Psi = \frac{\eta}{\rho} \left[\left(\frac{\partial v}{\partial r} \right)^2 + \frac{4v}{r} \frac{\partial v}{\partial r} + \frac{4v^2}{r^2} \right] \tag{15}$$

$$= \frac{\eta}{\rho} \left(\frac{\partial v}{\partial r} + \frac{2v}{r} \right)^2$$

$$= \frac{\eta}{\rho} \left[4\pi\rho \frac{\partial}{\partial m}(r^2 v) \right]^2 = 4\pi\Pi \frac{\partial}{\partial m}(r^2 v);$$

i.e., it matches the analogous quantity in Eq. (3) if it is considered that $Q \equiv -\Pi$ in the latter equation. In turn, the expression for the viscous force on the right-hand side of Eq. (2) matches expression (14).

Table 3. The entropy S_{test} calculated from the additional equation (10) for H20−180 at $t = 29.20$ s

i	m	$S +$ const, 10^8 erg g^{-1} K^{-1}	$S_{\text{test}} +$ const, 10^8 erg g^{-1} K^{-1}
1	1.1076×10^{-4}	3.7804	3.7816
10	3.5963×10^{-3}	8.8670×10^{-1}	8.8724×10^{-1}
20	3.5824×10^{-2}	1.0211	1.0217
30	1.4440×10^{-1}	1.2740	1.2742
40	2.5516×10^{-1}	-3.1207×10^{-1}	-3.1207×10^{-1}
50	3.6592×10^{-1}	-3.3635×10^{-1}	-3.3634×10^{-1}
60	4.7668×10^{-1}	-3.4208×10^{-1}	-3.4208×10^{-1}
70	5.8743×10^{-1}	-3.3754×10^{-1}	-3.3754×10^{-1}
80	6.9819×10^{-1}	-3.2608×10^{-1}	-3.2608×10^{-1}
90	8.0895×10^{-1}	-3.0441×10^{-1}	-3.0441×10^{-1}
100	9.1971×10^{-1}	-2.6710×10^{-1}	-2.6710×10^{-1}
110	1.0305	-2.1395×10^{-1}	-2.1395×10^{-1}
120	1.1412	-1.3925×10^{-1}	-1.3925×10^{-1}
130	1.2477	-3.9396×10^{-2}	-3.9396×10^{-2}
140	1.3100	4.6799×10^{-2}	4.6799×10^{-2}
150	1.3410	2.3998×10^{-1}	2.3998×10^{-1}
160	1.3564	6.4682×10^{-1}	6.4702×10^{-1}
170	1.3640	4.0611	4.0617
180	1.3678	5.6180	5.6184

However, in introducing artificial viscosity, it proved to be more appropriate to use quadratic rather than linear scalar viscosity (von Neuman and Richtmyer 1950) in the difference scheme. Therefore, the specific expression for Π differs from (13) by the substitution $\Pi \equiv \Pi'$, where

$$\Pi' = \zeta \left(\frac{\partial v}{\partial r} + \frac{2v}{r} \right)^2 = \zeta \left[4\pi\rho \frac{\partial}{\partial m}(r^2 v) \right]^2 . \quad (16)$$

In expression (16), we also substituted ζ for the viscosity coefficient η, because Π and Π' have the same dimensions, $[\Pi] = [\Pi'] = $ erg cm^{-3}. For the shock-front thickness in Lagrangian coordinates to be smeared by $4\pi r^2 k \Delta r_i \rho = k \Delta m_i$ ($k \gtrsim 1$), the viscosity coefficient ζ must be equal in order of magnitude to (in which case, $\Pi' \simeq \rho v^2$)

$$\zeta = \rho k^2 (\Delta r_i)^2. \quad (17)$$

Using relations (16) and (17) and the relation $Q = -\Pi'$, we obtain formula (6) with $A_q = k^2$; i.e., the dimensionless coefficient A_q is actually of the order of unity and it determines the number of spatial zones for a shock-front thickness of $\sim \sqrt{A_q}$.

It remains to note that similar conclusions could be reached with shear (tensor) physical viscosity. However, since it is more complex, there is apparently little point in using the corresponding analog as artificial viscosity in the convective hydrodynamic model.

As was said above, expression (10) contains the term for the specific power of the viscous energy dissipation

$$T \left(\frac{\partial S}{\partial t} \right)_q = -4\pi Q \frac{\partial (r^2 v)}{\partial m}, \quad (18)$$

attributable to artificial viscosity. Recall that, according to (6)–(7), it is always nonnegative. As the entropy increases in the outer model layers, this term becomes comparable to the other terms from Eq. (10) and even exceeds them inside the compression shock fronts by several orders of magnitude, although these shocks are weak in the hydrodynamic sense. Figure 4 shows the velocity, entropy, and $(\partial S/\partial t)_q$ profiles for H20−180 at the time $t = 29.20$ s, close to the onset of detonation from the edge. We see two local entropy maxima: the flatter maximum closer to the center

and the sharper maximum closer to the edge, which plays no role in the development of delayed detonation because of the low density in this (next-to-last) mass zone. In contrast, the narrow sharp maximum of $(\partial S/\partial t)_q$ located at $r \sim 2 \times 10^8$ cm on the inside of the inner entropy maximum led to a thermonuclear explosion and to the development of detonation from the edge at $r \sim 3 \times 10^8$ cm (see Fig. 3).

In comparison with our previous study (Dunina-Barkovskaya *et al.* 2001), where we used an estimate for the increase in entropy inside the steady-state plane fronts of weak shocks (Landau and Lifshitz 1954), here we significantly refined this increase in entropy in arbitrary (unsteady-state, nonweak, and nonplane) compression waves, as follows from the derivation of the entropy production equation (10). Therefore, we should also emphasize that the above derivation of the artificial-viscosity terms (6)−(7) in the basic equations of the convective hydrodynamic model (1)−(5) in terms of physical volume viscosity is also valid in the unsteady-state, nonplane case of nonweak compression waves.

From the viewpoint of numerically solving Eqs. (1)−(5) using the difference scheme that was developed by Blinnikov and Rudzskii (1984), Blinnikov and Bartunov (1993), and Blinnikov and Dunina-Barkovskaya (1993, 1994), it is also important to compare the entropy inferred from the solution of the additional equation (10) with its value that follows from the adopted equations of state. Table 3 makes such a comparison for a slightly sparse Lagrangian grid at the same time $t = 29.20$ s for H20−180, which shows an approximate match between the specific entropies S when delayed detonation sets in, in the most critical time interval of this calculation: the maximum discrepancy between S is $\approx 0.6\%$. Such an independent check on the accuracy of the difference solution of the problem was also made at all instants of time in the other calculations. We emphasize that the entropy plays a special role in the thermonuclear mechanism of SN-Ia explosions under consideration.

CONCLUSIONS

Here, we continued to study the thermonuclear explosion mechanism for presupernovae in the form of an accreting sub-Chandrasekhar-mass carbon−oxygen core (white dwarf) in terms of the convective hydrodynamic model presented previously (Dunina-Barkovskaya and Imshennik 2000; Dunina-Barkovskaya *et al.* 2001). In all probability, the external boundary conditions for temperature and pressure have to be considered in more detail than was done previously. We attempted to numerically simulate the outer layers of an accreting white dwarf by taking into account helium burning (of the main matter of

the accretor), which was reflected in a new boundary condition for temperature. We also developed a special difference technique for adding extra Lagrangian layers that become shallower toward the edge, where possible. The latter improvement of the Lagrangian scheme for solving the difference problem results in a significant reduction of the external boundary pressure, thereby ensuring that the condition of a thin envelope is satisfied at the time of the thermonuclear explosion. In previous calculations, it was violated, as we managed to ascertain in our series of calculations.

Despite the significant increase in the surface temperature of a CO core (approximately by a factor of 10, i.e., to $\sim 5 \times 10^7$ K) and the significant decrease in its surface pressure (also approximately by a factor of 10), delayed detonation was obtained with a convective parameter $\alpha_c \simeq 2 \times 10^{-3}$, irrespective of the possible variations in the above boundary conditions. Nevertheless, the range of convection parameters, $3 \times 10^{-4} \lesssim \alpha_c \lesssim 2 \times 10^{-3}$, significantly narrowed, because at the typical $\alpha_c = 1 \times 10^{-3}$ (Dunina-Barkovskaya *et al.* 2001) this regime was obtained only in the exceptional cases of variations in the external boundary conditions. It became clear that delayed detonation depended on external boundary conditions. In this study, these conditions seem more adequate than the previous, highly simplified conditions. This dependence can, in principle, be determined by extending the physical model of the presupernova evolution and explosion to include the hydrodynamic mass accretion itself. However, this approach at least implies that the hydrodynamic model is not one-dimensional and calls into question the assumed constancy of the accretion rate in an evolving binary system.

Apart from an attempt to study the role of external boundary conditions, we confirmed the mechanism for the onset of delayed detonation itself by justifying the increase in entropy that results from the propagation of the compression waves generated by the initial deflagration−pulsational regime of carbon burning in the outer presupernova layers. In all cases, we numerically solved the additional entropy production equation (10). This equation gives an independent method for calculating the entropy as a function of time and the Lagrangian coordinate, similar to all the other physical quantities that appear in the system of equations (1)−(5). This additional calculation first provides a check on the accuracy of the entire solution of the convective hydrodynamic model problem, because the entropies, primarily for unsteady-state explosion conditions, were shown to be equal. In addition, we showed that the expression for viscous energy dissipation in the case of quadratic artificial scalar viscosity (6) and (7) could be directly derived

from the standard expressions for physical volume viscosity. Viscous energy dissipation produces the characteristic sharp entropy peaks in the outer presupernova layers. These peaks lead to the necessary conditions for the onset of delayed detonation that can be created by an SN-Ia-scale thermonuclear explosion of a sub-Chandrasekhar-mass CO core.

ACKNOWLEDGMENTS

REFERENCES

1. V. P. Arkhipova, in *Eruptive Stars: Collection of Scientific Works,* Ed. by A. G. Masevich (Moscow, 1996), p. 47.
2. G. S. Bisnovatyĭ-Kogan, *Physical Problems of the Theory of Stellar Evolution* (Nauka, Moscow, 1989).
3. S. I. Blinnikov and O. S. Bartunov, Astron. Astrophys. **273**, 106 (1993).
4. S. I. Blinnikov and N. V. Dunina-Barkovskaya, Astron. Zh. **70**, 362 (1993) [Astron. Rep. **37**, 187 (1993)].
5. S. I. Blinnikov and N. V. Dunina-Barkovskaya, Mon. Not. R. Astron. Soc. **266**, 289 (1994).
6. S. I. Blinnikov and M. A. Rudzskii, Pis'ma Astron. Zh. **10**, 363 (1984) [Sov. Astron. Lett. **10**, 152 (1984)].
7. E. Cappellaro, P. A. Mazzali, S. Benetti, *et al.*, Astron. Astrophys. **328**, 203C (1997).
8. S. Cassisi, I. Iben, Jr., and A. Tornambe, Astrophys. J. **496**, 376 (1998).
9. N. V. Dunina-Barkovskaya and V. S. Imshennik, Tr. Fiz. Inst. Akad. Nauk **227**, 32 (2000).
10. N. V. Dunina-Barkovskaya, V. S. Imshennik, and S. I. Blinnikov, Pis'ma Astron. Zh. **27**, 412 (2001) [Astron. Lett. **27**, 353 (2001)].
11. D. A. Frank-Kamenetskiĭ, *Physical Processes in Stars* (Fizmatgiz, Moscow, 1959).
12. V. G. Gorbatskiĭ, *Physics of Space: A Small Encyclopedia* (Sov. Éntsiklopediya, Moscow, 1986), p. 445.
13. V. S. Imshennik and D. K. Nadezhin, Itogi Nauki Tekh., Ser. Astron., 63 (1982).
14. L. N. Ivanova, V. S. Imshennik, and V. M. Chechetkin, Astron. Zh. **54**, 354 (1977) [Sov. Astron. **21**, 197 (1977)].
15. N. E. Kochin, *Vector Calculus and Fundamentals of Tensor Calculus* (Akad. Nauk SSSR, Moscow, 1951).
16. A. Kovetz and D. Prialnik, Astrophys. J. **424**, 319 (1994).
17. L. D. Landau and E. M. Lifshitz, *Mechanics of Continuous Media* (Gostekhizdat, Moscow, 1954).
18. P. J. Schinder, D. N. Schramm, P. J. Wiita, *et al.*, Astrophys. J. **313**, 531 (1987).
19. M. Schwarzschild, *Structure and Evolution of the Stars* (Princeton Univ. Press, Princeton, 1958; Inostrannaya Literatura, Moscow, 1961).
20. E. I. Sorokina, S. I. Blinnikov, and O. S. Bartunov, Pis'ma Astron. Zh. **26**, 90 (2000) [Astron. Lett. **26**, 67 (2000)].
21. J. von Neuman and R. D. Richtmyer, J. Appl. Phys. **21**, 232 (1950).
22. L. R. Yungel'son, in *Proceedings of the International Conference in Honour of Professor A. G. Massevitch's 80th Birthday "Modern Problems in Stellar Evolution," Zvenigorod, 1998,* Ed. by D. S. Wiebe (GEOS, Moscow, 1998), p. 79.

Translated by V. Astakhov

Possibilities for Detecting Extinct Radio Pulsars

V. S. Beskin[1*] and S. A. Yeliseyeva[2]

[1]*Lebedev Institute of Physics, Russian Academy of Sciences, Leninskii pr. 53, Moscow, 119991 Russia*
[2]*Moscow Institute of Physics and Technology, Institutskii per. 9, Dolgoprudnyi, Moscow oblast, 141700 Russia*
Received July 17, 2002

Abstract—We explore the possibilities for detecting pulsars that have ceased to radiate in the radio band. We consider two models: the model with hindered particle escape from the pulsar surface [first suggested by Ruderman and Sutherland (1975)] and the model with free particle escape (Arons 1981; Mestel 1999). In the model with hindered particle escape, the number of particles that leave the pulsar magnetosphere is small and their radiation cannot be detected with currently available instruments. At the same time, for Arons' model, both the number of particles and the radiation intensity are high enough for such "extinct" pulsars to be detectable with the GLAST and INTEGRAL satellites. © *2003 MAIK "Nauka/Interperiodica".*

Key words: *neutron stars, radio pulsars.*

INTRODUCTION

More than 1200 radio pulsars are currently known (Camilo *et al.* 2000). Most of them belong to young neutron stars (NSs) with characteristic ages of ~ 10 Myr. Since the lifetimes of radio pulsars are much shorter than the age of the Universe, up to 10^9 NSs that have already ceased to radiate in the radio band must exist in our Galaxy (Lipunov 1987). The possibility of their detection is commonly associated with the thermal radiation attributable either to intrinsic stores of NS thermal energy (Yakovlev *et al.* 1999) or to accretion from interstellar gas (Colpi *et al.* 1998). In both cases, the electrodynamic processes in the NS magnetosphere are assumed to cease to play a crucial role. However, the cessation of secondary-plasma production in the region of the magnetic poles at rotation periods $P \sim (2-3)$ s by no means implies that the electrodynamic processes become unimportant. Thus, for example, it is well known that secondary plasma cannot be produced in the region of closed magnetic field lines only at periods $P > P_{cr} \sim 10^5 B_{12}^{4/3}$ s (Istomin and Mosyagin 1995), where $B_{12} = B/10^{12}$ G. Therefore, at $P < P_{cr}$, some of the closed magnetic field lines still remain filled with secondary electron–positron plasma. As we see, the critical period is long enough (more than a month) for the electrodynamic processes in extinct radio pulsars to play a significant role for an appreciable length of time. Accordingly, particles can be effectively accelerated in the region of open

magnetic field lines where a strong longitudinal electric field must be generated. This acceleration must give rise to the observable radiation associated with curvature losses.

Clearly, the total intensity of this radiation is related to the number of charged particles that fall into the region of strong longitudinal electric fields. This, in turn, directly depends on the particle work function for the NS surface. Thus, by analyzing the radiation from extinct radio pulsars (or its absence), we can reach a definitive conclusion regarding the particle work function and, hence, obtain independent information on the structure of the particle acceleration region near the magnetic poles of radio pulsars.

Here, we discuss two basic models: the model with hindered particle escape from the pulsar surface (Ruderman and Sutherland 1975) and the model with free particle escape (Arons 1981; Mestel 1999). We show that in the model with hindered particle escape, the number of particles leaving the pulsar magnetosphere is small and their radiation cannot be detected with currently available instruments. At the same time, for the model with free particle escape, the number of particles and, hence, the total energy release are large enough for such extinct pulsars to be detectable with the GLAST and INTEGRAL satellites.

THE MODEL WITH HINDERED PARTICLE ESCAPE FROM THE PULSAR SURFACE

The simplest model used to calculate the radiation intensity is the model with hindered particle escape

---

*E-mail: beskin@lpi.ru

from the pulsar surface, since general-relativity effects introduce no significant corrections, because they do not qualitatively change the structure of the electrodynamic equations in the particle acceleration region (Beskin 1999). Since the particle work function for the NS surface in the Ruderman–Sutherland model is large, particles only fill the equatorial regions with a strongly curved magnetic field in which secondary particles can still be produced. As a result, the longitudinal electric field outside the plasma (in particular, on open magnetic field lines) can be strong enough for effective particle acceleration. In this case, the polar-cap size is determined by the last closed magnetic field line on which secondary plasma can still be produced (Istomin and Mosyagin 1995)

$$R_\perp \approx R \left(P/P_{\mathrm{cr}}\right)^{3/8}, \qquad (1)$$

where R is the NS radius.

Thus, for extinct radio pulsars, the observed radiation must be determined only by the radiation from primary particles through the so-called curvature losses. The mechanism of this radiation is similar to synchrotron radiation, but the radius of curvature of magnetic field lines R_c should be chosen in place of the Larmor radius $r_{\mathrm{L}} = m_e c^2 \gamma/eB$ (Zheleznyakov 1977). However, in contrast to young NSs, the condition for the production of secondary electron–positron pairs in the polar regions of extinct radio pulsars is not satisfied. Therefore, one might expect radiation from extinct radio pulsars only in the high-energy part of the electromagnetic spectrum. We emphasize that this point distinguishes our analysis from the numerous calculations of gamma-ray emission from radio pulsars, for which the entire secondary-particle spectrum should be taken into account [see, e.g., Harding *et al.* (2002) and references therein].

Let us estimate the expected flux from radio-quiet pulsars on Earth as the product of the energy losses by a single particle and the number of particles leaving the pulsar magnetosphere:

$$F \sim \frac{\Delta\mathcal{E}\dot{N}}{4\pi d^2}. \qquad (2)$$

Here, $\dot{N} = dN/dt$ is the number of particles that leave the pulsar magnetosphere, $\Delta\mathcal{E}$ are the energy losses by each of these particles, and d is the distance from the pulsar to the observer. Since the radiation mechanism in this case is curvature radiation, the particle energy losses can be defined as $\Delta\mathcal{E} = (d\mathcal{E}/dt)\Delta t$, where (Zheleznyakov 1977)

$$\frac{d\mathcal{E}}{dt} = \frac{2e^2 c}{3R_c^2}\gamma^4 \qquad (3)$$

is the power of the curvature radiation, $R_c \approx R^2/R_\perp$ is the radius of curvature of magnetic field lines, and the distance from the axis, $R_\perp \approx 10^4$ cm (1), determines the location of the last closed magnetic field line on which secondary plasma can still be produced.

It is well known that a strong longitudinal electric field can exist only near the NS surface. Far from the NS surface, the longitudinal electric field decreases sharply in strength even in the absence of outflowing plasma (see, e.g., Muslimov and Tsygan 1990). Therefore, we have two alternatives: the particle emits all its kinetic energy near the NS or it leaves the region with a small radius of curvature R_c virtually without changing its energy. In the former case, the particle energy losses $\Delta\mathcal{E}$ are determined by the radiation time τ_{rad} and $\Delta\mathcal{E} = m_e c^2 \gamma$. In the latter case, the energy losses are determined by the escape time of the particle from the region of a strong longitudinal electric field, $\tau_{\mathrm{esc}} = R_c/c \approx 10^{-3}$ s. In general, the minimum time $\Delta t = \min(\tau_{\mathrm{esc}}, \tau_{\mathrm{rad}})$ can be taken as Δt. In this case, $\tau_{\mathrm{rad}} = m_e c^2 \gamma/(d\mathcal{E}/dt)$, where the Lorentz factor of the accelerated particles can be estimated as

$$\gamma \sim \frac{eER_\perp}{m_e c^2} \sim \frac{e(4\pi\rho_{\mathrm{GJ}}R_\perp)R_\perp}{m_e c^2} \sim \frac{4\pi e R_\perp{}^2 B_0}{P m_e c^3}. \quad (4)$$

Here, B_0 is the NS surface magnetic field. As a result,

$$\tau_{\mathrm{rad}} \sim \frac{R^4 c^5}{\Omega^3 \omega_B^3 r_e R_\perp^8}, \qquad (5)$$

where $\rho_{\mathrm{GJ}} = en_{\mathrm{GJ}} = -\mathbf{\Omega}\mathbf{B}/(2\pi c) = B/(Pc)$ is the Goldreich–Julian charge density, $r_e = e^2/m_e c^2$ is the classical electron radius, and $\omega_B = eB/m_e c$ is the cyclotron frequency. Therefore, the radiation and escape times are of the same order of magnitude: $\tau_{\mathrm{rad}} \approx 10^{-4} B_{12}$ s, $\tau_{\mathrm{esc}} = R_c/c \approx 10^{-3}$ s. Finally, given the particle Lorentz factor, the characteristic energy of the curvature-radiation photons can be estimated:

$$E_{\mathrm{ph}} \approx 2.9 \times 10^3 B_{12}{}^{-1/2} P^{-3/8} \mathrm{MeV}. \qquad (6)$$

We see that the expected energies lie within the hard gamma-ray range.

Let us now consider the inflow of particles into the region of a strong longitudinal electric field. First, the production of primary particles can be associated with diffuse Galactic gamma-ray radiation, which causes the single-photon conversion of photons into electron–positron pairs. In this case, the number of particles being produced near the magnetic poles can be estimated as 2×10^5 particles s^{-1} (Shukre and Radhakrishnan 1982). Hence, the expected flux from the object must be

$$F \approx 0.3 \times 10^{-25} d_{10}^{-2} \mathrm{MeV\ cm^{-2}\ s^{-1}}, \qquad (7)$$

where $d_{10} = d/10$ pc.

Another source of primary particles could be the diffusion from the region of closed magnetic field lines filled with secondary plasma. The number of particles leaving the pulsar magnetosphere can be estimated using the formula (Istomin and Mosyagin 1995)

$$\dot{N} = \frac{dN}{dt} \sim n_{\mathrm{GJ}} R^3 \frac{\Omega^2}{\omega_B}. \quad (8)$$

As a result, the number of particles that diffuse into the region of a strong longitudinal electric field can be estimated as

$$\dot{N} \sim \frac{4\pi^2 m_{\mathrm{e}} R^3}{P^3 e^2} \sim 4 \times 10^8 \text{ particles s}^{-1}, \quad (9)$$

so the expected flux from the object must be

$$F \sim 10^{-13} d_{10}^{-2} P^{-3} \mathrm{MeV \ cm^{-2} \ s^{-1}}. \quad (10)$$

The flux turns out to be so low that the radiation power is not enough for the NS signal to be detectable even at $P \sim 2-4$ s. This is primarily because the number of primary particles that fall into the region of a longitudinal electric field is small, i.e., because the particles escape from the NS surface is hindered.

THE MODEL WITH FREE PARTICLE ESCAPE FROM THE PULSAR SURFACE. A QUALITATIVE TREATMENT

Let us now consider the model with free particle escape from the NS surface where the charge density of the outflowing particles differs only slightly from the Goldreich charge density. General-relativity effects then become significant near the NS surface (Muslimov and Tsygan 1990; Beskin 1990). In this case, since no particles are produced, the model of Mestel (1999), in which no secondary plasma is generated, rather than the model of Arons (1981), in which a reverse flow of secondary particles must exist, is realized [for more details, see Beskin (1999)]. However, an elucidation is required here. The point is that in Mustel's model, none of the magnetic field lines near the pulsar surface are preferred because of general-relativity effects, so the particles cannot be accelerated (Beskin 1990). In other words, the longitudinal electric field that arises from the mismatch between the outflowing-plasma charge density and the Goldreich charge density decelerates rather than accelerates the outflowing plasma.

Nevertheless, the absence of regular acceleration does not imply that plasma will not fill the polar regions. Only effective particle acceleration is not possible. On the other hand, even at small heights $r > r_0$, where

$$r_0 \approx 1.8 \times 10^6 \, (M/M_\odot) \, P^{1/7} \text{ cm}, \quad (11)$$

at which general-relativity effects become negligible, the difference between the plasma charge density and the Goldreich charge density will result in particle acceleration, at least at the half of the polar cap where the magnetic field lines deviate from the rotation axis (i.e., for which the angle between the magnetic field and the rotation axis increases with distance from the NS). Therefore, we assume below that particle acceleration begins when the radius $r = r_0$ is reached, while at smaller radii, the plasma on open magnetic field lines rotates rigidly with the NS. Finally, recall that in Mestel's model, as in Arons's model, the number of particles leaving the NS magnetosphere closely corresponds to the outflow of the Goldreich density from the polar-cap surface

$$\dot{N} = \pi R_0^2 n_{\mathrm{GJ}} c \approx \frac{10^{30} \Omega^2}{ce} \text{ particles s}^{-1}. \quad (12)$$

Here, $R_0 = (\Omega R/c)R$ is the polar-cap radius.

To determine the electric potential, we write the Poisson equation in a rotating coordinate system (see, e.g., Mestel 1999)

$$\nabla^2 \varphi = 4\pi (\rho_{\mathrm{GJ}} - \rho_{\mathrm{e}}). \quad (13)$$

Here, the Goldreich charge density and the particle charge density can be written as

$$\rho_{\mathrm{GJ}} = -\frac{\mathbf{\Omega B}}{2\pi c} = \frac{\Omega B}{2\pi c} \cos \theta_{\mathrm{b}}, \quad (14)$$

$$\rho_{\mathrm{e}} = -\frac{\Omega B}{2\pi c} \cos \theta_{\mathrm{b}}^{(0)}, \quad (15)$$

where θ_{b} is the current angle between the magnetic field line and the rotation axis and $\theta_{\mathrm{b}}^{(0)}$ is its value at the base of the acceleration region $r = r_0$.

For simplicity, we consider here the axisymmetric case of a coaxial rotator where all magnetic field lines are preferred. After substituting the expressions for the plasma charge density and the Goldrecih charge density, the problem reduces to solving the equation

$$\nabla^2 \varphi = \frac{9}{4} \frac{\Omega B(r_0)}{c} \left(1 - \frac{r_0}{r}\right) \left(\frac{r_0}{r}\right)^3 \sin^2 \theta \quad (16)$$

with the boundary conditions

$$\varphi(r = r_0) = 0; \quad \varphi'(r = r_0) = 0; \quad (17)$$
$$\varphi\left(r = R_{\mathrm{L}} \sin^2 \theta\right) = 0.$$

Here, $R_{\mathrm{L}} = c/\Omega$ is the radius of the light cylinder. As a result, we have as a zero approximation for the solution of this equation

$$\varphi \approx \frac{\Omega B_0}{c} \frac{R^3}{R_{\mathrm{L}}}, \quad (18)$$

so

$$\gamma \approx \frac{e\varphi}{m_{\mathrm{e}} c^2} = \left(\frac{\Omega R}{c}\right)^2 \left(\frac{\omega_B R}{c}\right). \quad (19)$$
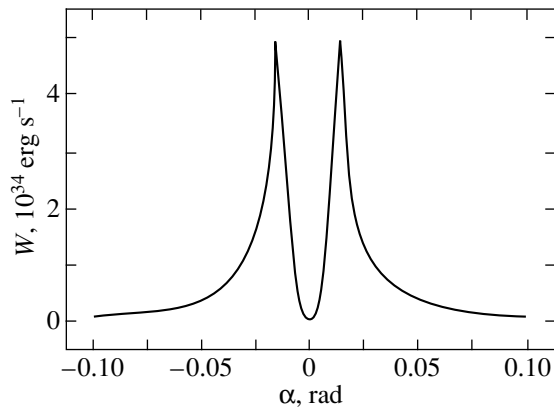
Fig. 1. Radiation intensity W versus angle α for a central beam passage. In what follows, the NS rotation period is assumed to be $P = 1$ s.

Fig. 2. Radiation intensity $I_{\mathcal{E}}(\alpha)$ versus angle α for the energy $E = 30$ MeV.
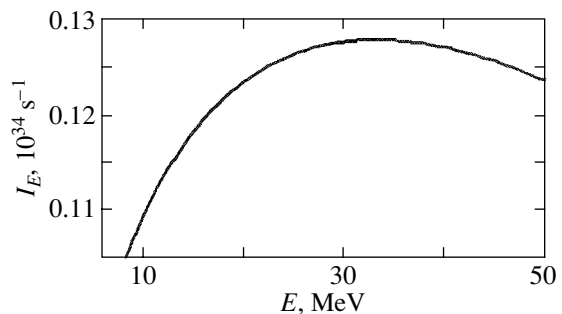
Fig. 3. The energy spectrum of the period-averaged radiation intensity.

Above, we used the law of conservation of magnetic flux, which yields $B(r_0)r_0^3 = B_0 R^3$. Having estimated the times τ_{rad} and τ_{esc}, just as for the model with hindered particle escape from the NS surface, we find that $\tau_{\text{rad}} \approx \tau_{\text{esc}}$ at $P = P_{\text{break}}$, where

$$P_{\text{break}} = \frac{2\pi R}{c}\left(\frac{2r_e}{3R}\right)^{1/7}\left(\frac{\omega_B R}{c}\right)^{3/7} \approx 1.8 \text{ s.} \quad (20)$$

As we see, the break takes place at the NS rotation periods of greatest interest, when the expected radiation power is high (see below).

Next, we obtain $E_{\text{ph}} = \hbar c\gamma^3/R_c \approx 50 P_{-13/2}$ MeV $\approx 0.05 P^{-13/2}$ GeV for the energy of the curvature gamma-ray photons leaving the NS magnetosphere, which also fall within the gamma-ray range. Finally, the radiation power can be estimated as

$$W_1 \approx m_e c^2 \gamma \dot{N} \approx \left(\frac{\Omega R}{c}\right)^4 \left(\frac{\omega_B R}{c}\right)^2 \frac{m_e c^3}{r_e} \quad (21)$$

$$\approx 5 \times 10^{29}\frac{B_{12}^2}{P^4}, \quad \frac{\text{erg}}{\text{s}}, \quad P < P_{\text{break}};$$

$$W_2 \approx \frac{2e^2 c}{R_c^2}\gamma^4 \dot{N} \approx \left(\frac{\Omega R}{c}\right)^{11}\left(\frac{\omega_B R}{c}\right)^5 \frac{2m_e c^3}{3R} \quad (22)$$

$$\approx 3 \times 10^{31}\frac{B_{12}^5}{P^{11}} \quad \frac{\text{erg}}{\text{s}}, \quad P > P_{\text{break}}.$$

The value for $P < P_{\text{break}}$ (21) corresponds to the estimate obtained by Harding *et al.* (2002). Thus, the expected flux from such NSs

$$F \approx \frac{W_1}{4\pi d^2} \approx 3.5 \times 10^{-4}\frac{B_{12}^2}{P^4 d_{10}^2}\frac{\text{MeV}}{\text{cm}^2 s}, P < P_{\text{break}}; \quad (23)$$
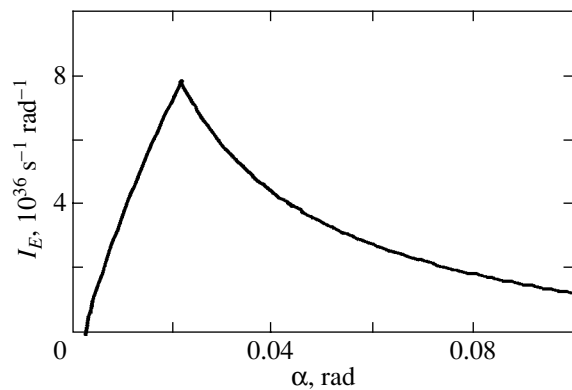
$$F \approx \frac{W_2}{4\pi d^2} \approx 2 \times 10^{-2}\frac{B_{12}^5}{P^{11}d_{10}^2}\frac{\text{MeV}}{\text{cm}^2 s}, P > P_{\text{break}}. \quad (24)$$

Since, as we see, the expected fluxes are large, we conclude that for the distances $d \sim 10-100$ pc characteristic of the nearest NSs, such fluxes can most likely be detected with the GLAST and INTEGRAL satellites. The latter are capable of detecting fluxes of $10^{-2}-10^{-4}$ MeV cm^{-2} s^{-1}.

A MORE ACCURATE SOLUTION FOR THE MODEL WITH FREE PARTICLE ESCAPE

Thus, for free particle escape from the NS surface, hard radiation can actually be detected from extinct radio pulsars. Therefore, it seems appropriate to find a more accurate distribution of the electric potential (and, hence, the particle energy) in the region of open magnetic field lines and, thus, to quantitatively determine the basic parameters of the expected radiation. To numerically solve Eq. (16), we used a simple iteration method for solving elliptic problems by the grid method (Fedorenko 1994). We chose a five-point
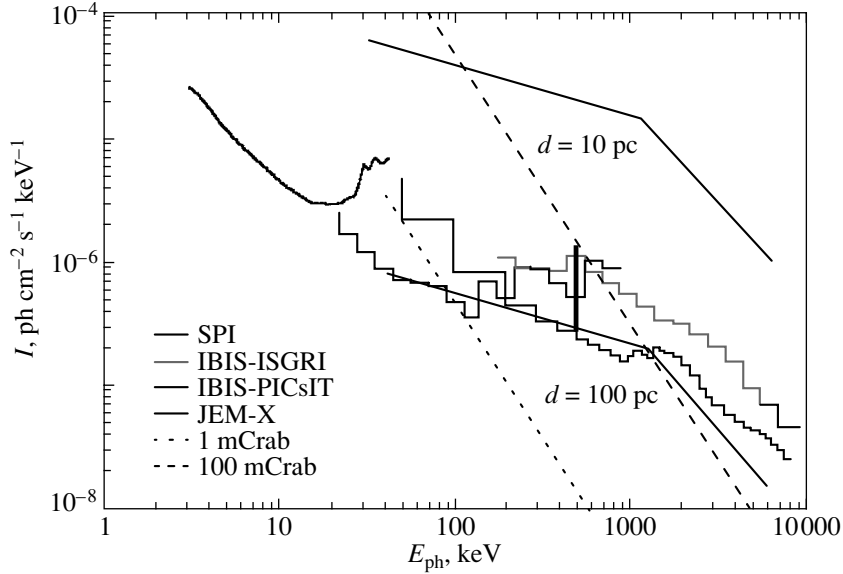
Fig. 4. Comparison of the sensitivities of the INTEGRAL instruments (the exposure time is 10^6 s) and the radiation intensities of extinct radio pulsars for two NS distances.

approximation of the Poisson equation as the (cross) template and the solution (Harding *et al.* 2002)

$$\varphi = \frac{3}{8}\frac{\Omega B_0}{c}\frac{R^3}{R_L}\left(1 - \frac{R_L}{r}\sin^2\theta\right), \qquad (25)$$

which is valid for $r \gg r_0$, as the first approximation. This solution can be easily obtained by analyzing Eq. (16) in which the radial derivatives are disregarded. Relation (25) accurately describes the solution of Eq. (16) even at $r > 1.5r_0$.

Since the radius of curvature of the dipole magnetic field increases with distance from the NS, the bulk of the radiation (which, recall, is associated with curvature losses) originates at small distances compared to the light-cylinder radius R_L. This property holds even if the energy of the emitting particle changes little as it moves along an open magnetic field line. Therefore, the magnetic field in the emission region may be assumed to be dipolar. For the radiation power $W(\alpha)$ into an element of solid angle $\alpha d\alpha d\varphi$, we can then write the expression

$$dW = \dot{N}\dot{\mathcal{E}}\frac{dV}{d\alpha}d\alpha. \qquad (26)$$

Here, $\dot{\mathcal{E}} = 2e^2c\gamma^4/3R_c^2$ is the power of the curvature radiation from a single particle, $R_c = r^2/r_\perp \approx 3r/2\alpha$ is the radius of curvature of the magnetic field lines, $dV = r^2 dr do$ is the volume element, and $\alpha \approx (3/2)\theta$ is the angle with respect to the magnetic dipole axis. Using now the fact that at $\tau_{rad} > \tau_{esc}$, the particle

Lorentz factor can be written as

$$\gamma = \frac{e\varphi}{m_e c^2} = \frac{3}{8}\frac{e}{m_e c^2}\frac{\Omega B_0}{c}\frac{R^3}{R_L}\left(1 - \frac{4}{9}\frac{R_L}{r}\alpha^2\right), \quad (27)$$

we obtain the following radiation intensity distribution in α by the integration over the azimuthal angle and radius r (Fig. 1):

$$W(\alpha) \approx \frac{BR^3\Omega e}{192}\left(\frac{e}{m_e c^2}\frac{\Omega B_0}{c}\frac{R^3}{R_L}\right)^4 \times A. \quad (28)$$

Here,

$$A = \frac{1}{2R^2}\alpha^2 - \frac{16}{27}\frac{R_L}{R^3}\alpha^4 + \frac{8}{27}\frac{R_L^2}{R^4}\alpha^6 \qquad (29)$$

if $0 \leq \alpha \leq 0.022/\sqrt{P}$ and

$$A = \frac{27}{160\alpha^2 R_L^2} \qquad (30)$$

if $0.022/\sqrt{P} \leq \alpha \leq 1$.

Having integrated expression (28) over α, we find the total radiation power

$$W \approx 3.5 \times 10^{29}B_{12}^5 P^{-11} \text{ erg s}^{-1}. \qquad (31)$$

Therefore, the expected flux from radio-quiet pulsars on Earth is

$$F = \frac{W}{4\pi d^2} \approx 2.5 \times 10^{-4}d_{10}^{-2}P^{-11}\frac{\text{MeV}}{\text{cm}^2\text{ s}}. \qquad (32)$$

The simple expression (27) for the particle energy also allows the spectral power of the radiation to be

estimated analytically. Fitting the curvature radiation spectrum for a single particle as

$$I_E \propto E^{1/3}\theta(E_{\max} - E), \qquad (33)$$

where $E_{\max} = (\hbar c/R_c)\gamma^3$, we can obtain (Fig. 2)

$$I_E(\alpha) = [3.6 \times 10^{39} E^{1/3}\alpha^{2/3} P^{-1} \qquad (34)$$
$$- 5.1 \times 10^{40} EP^3]\,\mathrm{s}^{-1}, \ \mathrm{if}\ 0 \le \alpha \le 0.022/\sqrt{P},$$

$$I_E(\alpha) = [0.22 \times 10^{38} E^{1/3}\alpha^{-2/3} P^{-5/3} \qquad (35)$$
$$- 5.1 \times 10^{40} EP^3]\,\mathrm{s}^{-1}, \ \mathrm{if}\ 0.022/\sqrt{P} \le \alpha \le 1.$$

Here, the photon energy E is given in ergs. However, since the expected radiation intensity is low, we are primarily interested in the spectral density of the radiation averaged over the NS rotation period. For a central passage through the beam, we obtain (Fig. 3)

$$I_E = [5.1 \times 10^{34} E^{1/3} P^{-7/3} - 1.2 \times 10^{37} EP^2]\,\mathrm{s}^{-1}. \qquad (36)$$

Figure 4 compares the threshold sensitivities of the INTEGRAL instruments (in particular, for the SPI detector) and the photon count rates for the model with free particle escape from the pulsar surface for distances from the NS to the observer of 10 and 100 pc. As we see, for nearby pulsars at distances 10−100 pc, INTEGRAL can, in principle, detect the gamma-ray fluxes from extinct radio pulsars.

CONCLUSIONS

Thus, we have shown that extinct radio pulsars can be observed for some time as intense gamma-ray sources. For nearby neutron stars, they can be detected with currently available detectors.

On the other hand, since the dependence on the NS rotation period P in the expressions for the radiation power is strong, radio-quiet pulsars with sufficiently long rotation periods (i.e., those which have long ceased to exist as radio pulsars or those for which the rotation period was relatively long even at the radio emission stage) can no longer be detected. Therefore, we can formulate two conditions for the possibility of detecting gamma-ray emission from extinct radio pulsars: a relatively small distance to such stars ($d \sim 10−100$ pc) and a short rotation period ($P \sim 2−4$ s). In this case, the detection of gamma-ray

emission with the parameters described above would be direct evidence for free particle escape from the NS surface.

REFERENCES

1. J. Arons, Astrophys. J. **248**, 1099 (1981).
2. V. S. Beskin, Pis'ma Astron. Zh. **16**, 665 (1990) [Sov. Astron. Lett. **16**, 286 (1990)].
3. V. S. Beskin, Usp. Fiz. Nauk **169**, 1169 (1999).
4. V. S. Beskin, A. V. Gurevich, and Ya. N. Istomin, *Physics of the Pulsar Magnetosphere* (Cambridge Univ. Press, Cambridge, 1993).
5. F. Camilo, A. G. Lyne, R. N. Manchester, *et al.*, in *Proceedings of the 177th Colloquium of the IAU "Pulsar Astronomy-2000 and Beyond," Bonn, 1999,* Ed. by M. Kramer, R. Wex, and R. Wielebinski (Astronomical Society of the Pacific, San Francisco, 2000), Astron. Soc. Pac. Conf. Ser. **202**, 3 (2000).
6. M. Colpi, R. Turolla, S. Zane, and A. Trevis, Astrophys. J. **501**, 252 (1998).
7. R. P. Fedorenko, *An Introduction to Computational Physics* (Mosk. Fiz.-Tekh. Inst., Moscow, 1994).
8. A. K. Harding, A. G. Muslimov, and B. Zhang, Astrophys. J. (in press), astro-ph/0205077 (2002).
9. Ya. N. Istomin and D. V. Mosyagin, Astron. Zh. **72**, 826 (1995) [Astron. Rep. **39**, 735 (1995)].
10. V. M. Lipunov, *Astrophysics of Neutron Stars* (Nauka, Moscow, 1987).
11. L. Mestel, *Stellar Magnetism* (Clarendon, Oxford, 1999).
12. A. G. Muslimov and A. I. Tsygan, Astron. Zh. **67**, 263 (1990) [Sov. Astron. **34**, 133 (1990)].
13. M. A. Ruderman and P. G. Sutherland, Astrophys. J. **196**, 51 (1975).
14. C. S. Shukre and V. Radhakrishnan, Astrophys. J. **258**, 121 (1982).
15. D. G. Yakovlev, K. P. Levenfish, and Yu. A. Shibanov, Usp. Fiz. Nauk **169**, 825 (1999).
16. V. V. Zheleznyakov, *Electromagnetic Waves in Cosmic Plasma (Generation and Propagation)* (Nauka, Moscow, 1977).

Translated by V. Astakhov

Triplet Structure of the H₂O Spectra in S255

M. I. Pashchenko[1*], E. E. Lekht[2], and A. M. Tolmachev[3]

[1]Sternberg Astronomical Institute, Universitetskii pr. 13, Moscow, 119992 Russia

[2]Instituto Nacional de Astrofísica, Óptica y Electrónica, Luis Enrique Erro No. 1,
Apdo Postal 51 y 216, 72840 Tonantzintla, Puebla, México

[3]Radio Astronomy Station, Lebedev Institute of Physics,
Russian Academy of Sciences, Pushchino, Moscow oblast, 142292 Russia

Received May 20, 2002

Abstract—We analyzed the monitoring data for the maser S255 obtained in the H_2O line at $\lambda = 1.35$ cm with the 22-m radio telescope at the Pushchino Radio Astronomy Observatory in 1981−2002. The maser was most active during 1998−2002. Since 2001, the H_2O spectra have been extended and complex; their triplet structure has been disrupted. The extent of the spectra was 24 km s^{-1} (from −6 to 18 km s^{-1}). We calculated orbital parameters for some of the components. We estimated the mass of the central star to be $(6-7)M_\odot$ and the outer Keplerian-disk radius to be ∼160 AU. © 2003 MAIK "Nauka/Interperiodica".

Key words: *radio sources; masers; interstellar medium; gaseous nebulae.*

INTRODUCTION

Among the H_2O masers associated with star-forming regions, sources with triplet spectra are of great interest. Such spectra can be formed in a rotating disk observed edge-on.

One such a source is the H_2O maser S255. The triplet structure of S255 was first studied by Cesaroni (1990). He constructed a model of the maser in the form of a Keplerian disk. The main argument for this model was the flux anticorrelation between the side triplet components found by Cesaroni. However, a 20-year-long monitoring (Pashchenko *et al.* 2001) shows that during some periods the H_2O spectra in S255 were complex and consisted of many components. Despite the significant difference in the structures of the spectra, their radial-velocity ranges, obtained by Pashchenko *et al.* (2001) and Cesaroni (1990), coincided and were from −2 to 14 km s^{-1}.

The H_2O maser is located in the S255 IR complex (Lo and Burke 1973), a compact region of active star formation. The distance to S255 IR was estimated to be 2.4 kpc (Jaffe *et al.* 1987) and the mass of the star was estimated to be $M_* \approx 18M_\odot$ (Cesaroni 1990). The source is located in a molecular cloud whose radial velocity measured in the CS line is 8.3 km s^{-1} (Morris *et al.* 1974).

*E-mail: `pachenko@sai.msu.ru`

Here, based on its monitoring with the RT-22 radio telescope (Pushchino), we study the evolution of the H_2O maser emission in S255 .

OBSERVATIONS AND DATA PRESENTATION

The H_2O maser emission toward S255 IR ($\alpha_{1950} = 06^h09^m58.2^s$, $\delta_{1950} = 18°00'17''$) was observed with the 22-m radio telescope RT-22 (Pushchino) from July 2000 until April 2002. We also used published data (Pashchenko *et al.* 2001). The noise temperature of the system with a cooled transistor amplifier at the input was within the range 120−150 K. The signal was analyzed by a 128-channel filter-bank spectrum analyzer with a frequency resolution of 7.5 kHz.

Figure 1 presents previously unpublished H_2O spectra of S255 (March 2001−April 2002). Figure 2 shows the variability of the total flux for the most active phase of the maser emission (1998−2002). The vertical arrow indicates the center of the interval June 1998−June 2000; h and i denote the successive activity cycles (Pashchenko *et al.* 2001). From 1981 until 2000, there were eight activity cycles, each about two years long. June 2000 may be considered as the beginning of another activity cycle. Since it clearly breaks up into two shorter intervals, we denote them by i_1 and i_2 for convenience. Below, for simplicity, we use these designations.

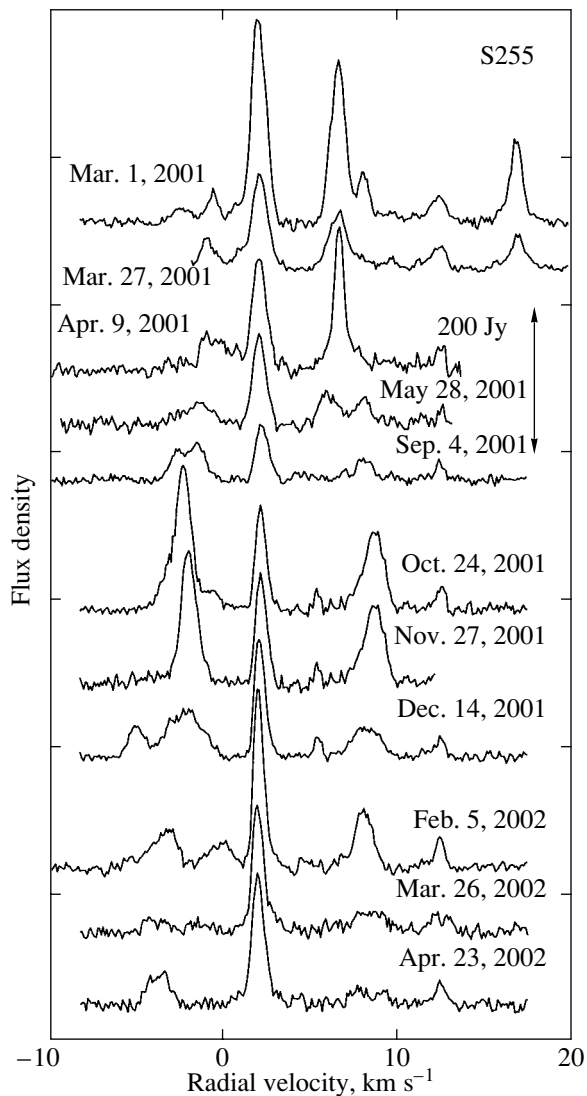Figure 3 shows the average spectra obtained for segments i_1 and i_2 and for the entire interval

Fig. 1. The spectra of H_2O maser emission from S255 obtained in 2001—2002. The vertical arrow indicates the major scale division.

Fig. 2. Variability of the total H_2O maser flux from S255. The arrow indicates the position of the maximum determined from a fitted Gaussian.

Fig. 3. Average spectra of the H_2O maser S255 for the July 2000—May 2001 and September 2001—April 2002 intervals, and for the entire interval (2000—2002).

(July 2000—April 2002). For convenience, we assigned ordinal numbers to some emission features.

Here, we also used the eight average spectra (for the eight activity cycles) obtained from the data of our entire monitoring of S255 from 1981 until 2000 (Pashchenko *et al.* 2001). We determined the radial velocities of individual features or groups of features from the average spectra of each of the nine activity cycles of S255. These velocities were related in time to the positions of the corresponding total-flux maxima. For h and i, we took the centers of the time intervals. The results are shown in Fig. 4, where we also used data from Cesaroni (1990). The large circles indicate the most intense components. The dashed straight line corresponds to the radial velocity of the molecular cloud.
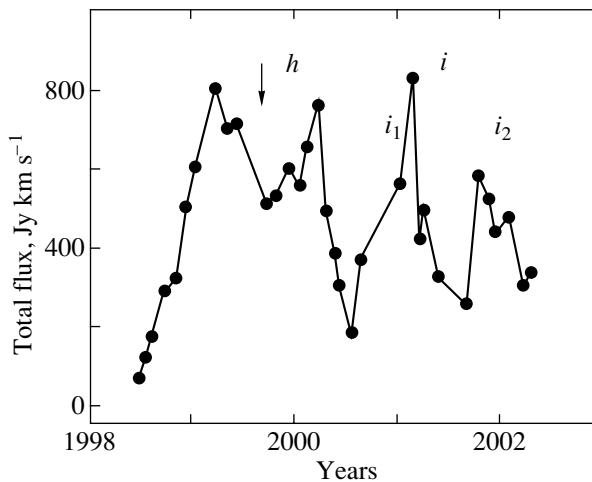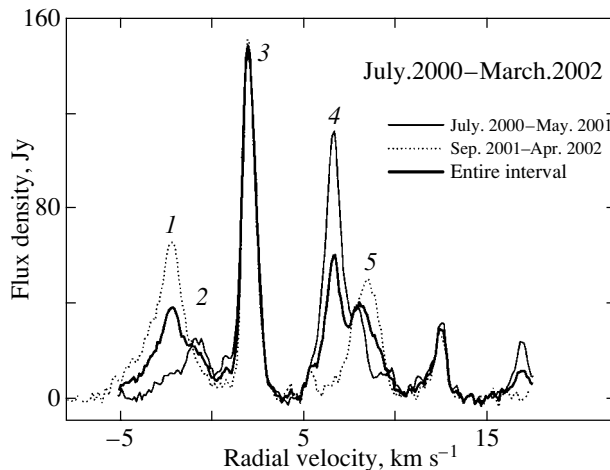
Figure 5 schematically shows the arrangement of the maser regions for the blue triplet component in S255 for the Keplerian-disk model.

DISCUSSION

Variability of the Total Flux

An important parameter for studying the evolution of maser emission and, in particular, the spectral structure, is the total (integrated) flux. Its variability in S255 has a cyclic pattern (Pashchenko *et al.* 2001). The most complex pattern of variability was observed from 1998 until 2002. The last two maser activity cycles, h and i, have dips at their centers. A particularly significant dip was observed
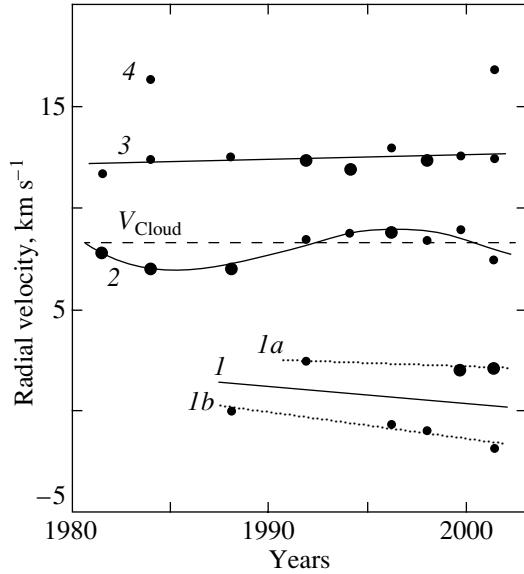
Fig. 4. Variations in the radial velocities of groups of features (or single features) in the H$_2$O maser S255 determined from average spectra.

Fig. 5. Arrangement of the H$_2$O maser regions in S255 for the blue component.

in cycle i. Cycles h and i occurred at a high level of maser activity, which is determined by the state of the central star.

It is quite natural that in this case, the favorable conditions for maser emission took place for a larger number of maser condensations, which gave rise to additional emission features. At the same time, the spectra ceased to be triplet ones. Thus, the spectral structure of the H$_2$O maser sources identified with Keplerian disks may be assumed to depend on the activity phase of the central star.

Variability of the H$_2$O Maser in 2000−2002

In accordance with the cyclic variability of the total flux, Fig. 3 shows average spectra for the intervals designated as i_1 and i_2 (the thin and dotted lines, respectively). There are both a difference and a coincidence between them. The main difference may be considered to be the fact that the intensity ratio of emission features within two groups (from −6 to 0 and from 5 to 10 km s^{-1}) located more or less symmetrically relative to the 2-km s^{-1} component varies. As we see from Figs. 1 and 3, the 2-km s^{-1} component is the most intense and stable.

Note the most important features of the maser during this period:

(1) the breakup of the variability cycle into two segments, i_1 and i_2;

(2) the high activity of the maser;
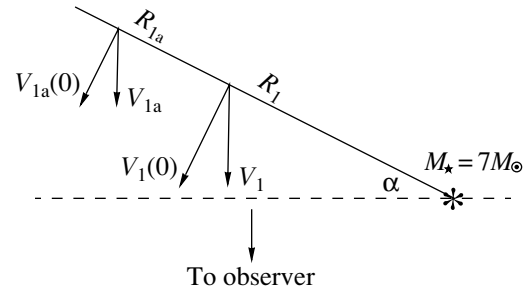
(3) the fast and significant variations of the spectra;

(4) a large extent of the spectra, from −6 to 18 km s^{-1};

(5) the absence of triplet structure;

(6) the stability of the emission from the blue (2 km s^{-1}) and red (12.5 km s^{-1}) components.

In period i_1, features *2* and *4* (see Fig. 3) that are closer to the main feature *3* of the maser activity cycle i than features *1* and *5* were most intense. Subsequently, in period i_2, the farther features *1* and *5* became more intense. Comparison of the spectra indicates that the intensities anticorrelate only for features *1* and *4*. This anticorrelation does not explain the overall pattern of evolution of the spectra. We can assume that the stellar wind from the central star successively excites masing regions. The emission of feature 1 is delayed from that of feature *4* by about one year. For a stellar-wind velocity of 100 km s^{-1}, the difference in the radial distances between features 1 and 4 relative to the star is ∼20 AU, which seems to be quite a reasonable value.

Structure of the Spectra

As we see from Fig. 4, the features in the average spectra can be separated into four groups. In turn, the first group splits into two subgroups. The features of the fourth group were observed only in two activity cycles. Nevertheless, their separation into one group is important in understanding the structure of the H$_2$O spectra. The emission of groups *2* and *3* was observed persistently. Thus, there was mainly a statistical recurrence of the triplet structure of the H$_2$O spectra in S255.

In most cases, the group of features with $V_{LSR} \approx$ 8 km s^{-1} was central, implying that the radial velocities of this group and the molecular cloud (8.3 km s^{-1}) are virtually the same. In the Keplerian-disk model for the maser S255, the velocity of the central component is the radial velocity of S255. Thus, we can assume that the maser S255 (the Keplerian disk) has no peculiar velocity relative to the molecular cloud.

The deviation of the points from a straight line for the central component (Fig. 4) may result from the complex spectral structure at these velocities. Thus, for example, there are two emission features in cycle i at a velocity of ~ 7.5 km s^{-1}. Variations of their flux ratio caused variations in the line shape and a displacement of the line peak in the spectrum. Nevertheless, the velocity variability of this group is well fitted by a sine wave with a period of the order of 20 years. Because of their small amplitude, these velocity variations cannot be associated with orbital motion. In addition, it should be noted that the sinusoidal velocity variations are associated with the average spectrum rather than with a specific emission feature.

Variations in the radial velocities of the features belonging to the central component can take place, for example, when the stellar wind acts on clumps of matter (maser condensations). We cannot rule out the existence of an activity superperiod of the maser and, hence, the central star. However, judging by the pattern of variability of the total flux (see also Pashchenko et $al.$ 2001), it is so far hard to tell with certainty whether such a superperiod exists. If it exists, it is most likely longer than 20 years.

The red component 3 has always been observed, while the blue component 1 has been observed since 1987. The blue component splits up into two ($1a$ and $1b$). Their fluxes anticorrelate. Cycle i, during which both components were present in the spectra, is an exception.

A Model of the Maser

Thus, Fig. 4 led us to conclude that there was a triplet structure in S255. The central component is at a velocity of ~ 8 km s^{-1}, which is confirmed by the fact that the radial velocities of the central component and the molecular cloud observed in the CS line are equal. The triplet structure of the spectra for single components showed up only at some epochs, mainly when the maser activity was low. The intensities of the side components anticorrelated at these epochs. This anticorrelation can be explained by the competition between spatial emission modes in a partially saturated disk maser with anisotropic pumping.

The detected radial-velocity drift of the blue-component features allows us to calculate some parameters of the Keplerian disk. Although these calculations are approximate, they make it possible to refine the parameters of the Keplerian-disk model proposed by Cesaroni (1990).

The radial velocity of a condensation relative to the central star (to be more precise, relative to the center of mass) varies as

$$V(\alpha) = V(0) \cos \alpha, \qquad (1)$$

where α is the angle between the radius vector of the condensation and the plane of the sky and $V(0)$ is the orbital velocity of the condensation. Differentiating formula (1) and making minor transformations yields

$$\frac{dV}{dt} = -V(\alpha) \tan \alpha \, \frac{2\pi}{T}, \qquad (2)$$

where T is the orbital period of the condensation.

Let us perform calculations for the straight line 1 that represents the mean drift of the blue triplet component (Fig. 4). According to Cesaroni (1990), the group must be in the side amplification corridor of the Keplerian disk. Therefore the angle α does not differ greatly from 0°. In accordance with similar calculations for S140 (Lekht and Sorochenko 2001), we can assume that $|\alpha| < 30°$. It follows from Fig. 4 that the radial velocity of component 1 relative to the central component 2 at epoch 2001 is 8 km s^{-1} and the rate of its change is 0.13 km s^{-1} yr^{-1}. For $\alpha \approx 30°$, an orbital period of the condensation $T_1 \approx 230$ yrs corresponds to this rate of change in V_{LSR}. According to Eq. (1), $V_1(0) = 9.2$ km s^{-1}.

As was shown by Lekht et $al.$ (1993), the derived period can be its upper limit. Thus, we can estimate an upper limit on the central-star mass, $M_* = \{T_1[V_1(0)]^3\}/(2\pi G) < 7 M_\odot$, and an upper limit on the distance from the star to the condensation, $R_1 = T_1 V_1(0)/2\pi < 70$ AU, from the condition of Keplerian rotation.

Let us now perform similar calculations for component $1a$. Its radial velocity relative to the central component is 6 km s^{-1} and the rate of its change is 0.04 km s^{-1} yr^{-1}. The observed anticorrelation between the intensities of components $1a$ and $1b$ can take place only in the absence of their relative motion, i.e., toward each other (Cesaroni 1990). Since they have different radial velocities but are in the blue amplification corridors, they must be located on the same radius vector from the star (see Fig. 5). Thus, we can assume that $\alpha \approx 30°$ for component $1a$ as well. Using the corresponding formulas, as in the case of component 1, we obtain $T_{1a} \approx 570$ yr, $V_{1a}(0) = 7.2$ km s^{-1}, $M_* < 7 M_\odot$, and $R_{1a} < 130$ AU.

To estimate the outer radius of the Keplerian disk in S255, we make use of the fact that the red component 2 has a radial velocity of about 4.8 km s^{-1} relative to the central component and, hence, it is farther from the star than the blue features. Its radial-velocity drift was modest, 0.02 km s^{-1} yr^{-1}. This value is a factor of 3 smaller than the scatter of data points caused by variations in the flux ratio of the emission features belonging to this red group. Certainly, the accuracy of the calculations is lower in this case. Calculations similar to the previous ones yielded

the following results: $T_3 = 900$ yr, $M_* \approx 5.7 M_\odot$, and $R_3 \approx 160$ AU.

The close match between the stellar masses can be an argument for the fact that the observed drift reflects the orbital motion in the Keplerian disk. Based on the three calculations, we can assume that the stellar mass lies within the range $(6-7)M_\odot$. The derived parameters differ from the corresponding parameters in Cesaroni's model. In our model, the stellar mass is a factor of 2.5 lower, while the outer radius of the disk and the orbital periods are a factor of ≈ 4 smaller.

Thus, our analysis of the results of the 20-year-long monitoring in the 1.35-cm line indicates that the triplet structure of the H_2O spectra in S255 identified with a Keplerian disk was not observed persistently but only in some periods. In other periods, however, the spectra were complex and consisted of many emission features. Nevertheless, the separation of spectral features into three main groups was preserved. In the Keplerian-disk model for S255, these are side and central components. The emission of group 4 appeared only twice: weak emission with a flux of no more than 2 Jy in 1983−1985 and strong emission (110 Jy at maximum) in 2001−2002. The region responsible for this emission is most likely located in the inner Keplerian disk, in the red amplification corridor.

CONCLUSIONS

(1) The long-term monitoring revealed H_2O maser emission in S255 in a wide velocity range, from -7 to 18 km s^{-1}.

(2) There was a stable recurrence of a triplet spectral structure. The triplet structure was observed for three groups of features with similar radial velocities within each group.

(3) The maser was most active from 1998 through 2002. There were significant variations in the total flux on a time scale that was several times shorter than the mean period of the cyclic variability, i.e., two years. During this period, the triplet structure of the H_2O spectrum was disrupted.

(4) The fluxes of the emission features located in the blue amplification corridors of the Keplerian disk anticorrelated.

(5) We estimated the mass of the central star in S255 to be $(6-7)M_\odot$ and the outer radius of the Keplerian disk to be ≈ 160 AU.

REFERENCES

1. R. Cezaroni, Astron. Astrophys. **223**, 513 (1990).
2. D. T. Jaffe, J. A. Davidson, M. Dragovan, and R. H. Heldebrand, Astrophys. J. **284**, 637 (1984).
3. E. E. Lekht, S. F. Likhachev, R. L. Sorochenko, and V. S. Strel'nitskiĭ, Astron. Zh. **70**, 731 (1993) [Astron. Rep. **37**, 367 (1993)].
4. E. E. Lekht and R. L. Sorochenko, Astron. Zh. **78**, 137 (2001) [Astron. Rep. **45**, 113 (2001)].
5. K. Y. Loy and B. F. Burke, Astron. Astrophys. **26**, 487 (1973).
6. M. Morris, P. Palmer, B. E. Turner, and B. Zuckerman, Astrophys. J. **191**, 111 (1974).
7. M. I. Pashchenko, E. E. Lekht, and I. I. Berulis, Astron. Zh. **78**, 696 (2001) [Astron. Rep. **45**, 600 (2001)].

Translated by G. Rudnitskii

Spectroscopic and Photometric Studies of the Magnetic Cataclysmic Variable EU UMa (=RE1149+28)

T. A. Somova[1*], N. N. Somov[1], J. M. Bonnet-Bidaud[2], and M. Mouchet[3,4]

[1]*Special Astrophysical Observatory, Russian Academy of Sciences, Nizhnii Arkhyz, Stavropolskii krai, 369167 Russia*

[2]*Service d'Astrophysique, Centre d'Etudes Nucleaires de Saclay, CEA/DSM/DAPNIA/SAP, 91191 Gif-sur-Yvette Cedex, France*

[3]*LUTH Observatoire de Paris-Medon, F-92190 Medon, France*

[4]*Universitè Denise Diderot, Place Jussieu, F-75005 Paris Cedex, France*

Received August 5, 2002

Abstract—We present the optical observations of the AM Herculis system EU UMa (=RE1149+28) carried out in February 1993 with a TV scanner and a photometer (NEPh) at the secondary focus of the 6-m Special Astrophysical Observatory telescope. Spectroscopy with a time resolution of 300 s and a spectral resolution of 2 Å in the wavelength range $\approx 3950-4950$ Å is used to analyze the variability of emission-line profiles, equivalent widths, central intensities R_c, and radial velocities with orbital phase. We determined the orbital period of the system from line radial-velocity measurements, 90.0 ± 0.2 min. The emission-line profiles are highly variable. The Hβ and He II 4686 Å lines exhibit P Cyg profiles at selected phases. The spectral-line parameters were found to vary significantly on time scales from 5 to 15 min. The possible causes of the detected spectroscopic variability are discussed. © 2003 MAIK "Nauka/Interperiodica".

Key words: *stars—variable and peculiar, polars, accretion.*

INTRODUCTION

The AM Herculis (AM Her) stars are close binaries that represent the subclass of cataclysmic variables. They are also classified as X-ray binaries. In these objects, a synchronously rotating (with orbital period) magnetized white dwarf with a magnetic-field strength $B \approx 10-230$ MG accretes matter from a low-mass companion—a red dwarf. The matter transferred from the secondary component to the primary forms no accretion disk around the latter. This process is inhibited by the strong magnetic field of the primary component, which controls the motion of the gas and channels it to the magnetic poles of the white dwarf. Accreting plasma moves along magnetic field lines into an accretion column(s), a narrow region(s) near the pole(s) of the white dwarf. In the polar regions of the white dwarf, energy is released via accretion over a wide spectral range: from hard X-rays to the far infrared. A characteristic property of these systems is the high intrinsic linear and circular polarization of their optical radiation (Tapia 1977). Therefore, these objects are also called polars. An overview of the basic information on AM Her systems

(or polars) was given by Cropper (1990), Voikhanskaya (1990), and Chanmugam (1992).

After the ROSAT All-Sky Survey, the number of known magnetic cataclysmic variables tripled; presently, there are about 60 such systems. EU UMa (=RE1149+28) was also discovered during this survey. The R and B photometry obtained by Mittaz *et al.* (1992) yielded the following magnitude estimates for the star averaged over the observing time: $17^m\!.0 \pm 0.1$ and $16^m\!.7 \pm 0.1$. They also determined the probable orbital periods of the polar, 102.78 ± 0.65 or 90.09 ± 0.50 min.

In our studies, the objective was to investigate the rapid spectroscopic variability in this polar on time scales from several to several tens of minutes. To this end, we took spectra of this faint source on the 6-m telescope using a TV photon counter with a high time resolution. In order to know in which brightness state we studied the system, we planned to estimate its magnitudes. Based on our spectroscopic data, we intended to determine the orbital period of the polar and to analyze the behavior of the spectral parameters for emission lines with orbital phase. This paper is the result of our series of studies of this magnetic cataclysmic variable published in the proceedings of

---
[*]E-mail: `tsom@sao.ru`

Table 1. A log of spectroscopic observations

Date	Start (UT)	End (UT)	Exposure time, s	V
February 14, 1993	00:51:27	02:40:01	6514	$16^{m}\!.6$

several conferences (Bonnet-Bidaud *et al.* 1994; So-mov *et al.* 1995; and Somova *et al.* 2000).

OBSERVATIONS AND RESULTS

Our observations were performed on February 14 and 15, 1993, at the secondary focus of the 6-m telescope (N1) (Ioannisiani *et al.* 1982) with an SP-124 spectrograph (Gusev *et al.* 1976) equipped with a TV scanner (Somova *et al.* 1982; Drabek *et al.* 1986; and Afanasiev *et al.* 1991) and a NEPh photometer (Vikul'ev *et al.* 1991). We used a B2 diffraction grating (1200 lines mm^{-1}) with a dispersion of 50 Å mm^{-1} and a spectral resolution of ≈ 2 Å, which allowed spectra to be taken in the wavelength range 3950–4950 Å. Information was recorded with the TV scanner in a frame-by-frame mode; data on each arrived photon was recorded using the technique of dynamic spectroscopy (Somov 1988). The spectra were wavelength-calibrated with a He–Ar–Ne lamp.

We reduced the spectroscopic data with the codes written on the SIPRAN (a special interpreter for programming and reducing astronomical observations) algorithmic language (Somov 1986) using the programs and techniques described by Kopylov *et al.* (1986). A log of our spectroscopic observations is given in Table 1.

We made the photometric measurements with the NEPh photometer that was also mounted at the secondary N1 focus of the 6-m telescope. The classical (Johnson) four-color $UBVR$ photometry was performed to estimate the polar magnitudes. The accuracy of our measurements was about $0^{m}\!.1$. The photometer aperture was $12''$ in diameter. The photometric standard was star SA56B (Neizvestny 1995). On the first date of our observations (JD 2449033.5869), the $UBVR$ measurements of EU UMa yielded the following results: $V = 16^{m}\!.56 \pm 0.13$, $U-B = -0.39 \pm 0.22$, $B-V = 0.03 \pm 0.19$, and $V-R = 0.15 \pm 0.25$. The V magnitude of the source at the end of our observations (JD 2449034.5439) was $17^{m}\!.2 \pm 0.1$.

Figure 1 shows an average continuum-normalized spectrum of the object. The Hβ, Hγ, Hδ, and He II 4686 Å emission lines are clearly seen in the spectrum; in addition, we see the C III–N III 4640 Å blend and He I (4921 and 4471 Å) lines. Table 2 presents the period-averaged equivalent widths (EW), central line intensities R_c (the ratio of intensity at the line center to continuum intensity), and FWHMs. For comparison, this table also gives the emission-line equivalent widths for this polar measured by Mittaz *et al.* (1992). We see from the table that the Hγ and Hβ equivalent widths are, respectively, 20% lower and 25% higher than those from Mittaz *et al.* (1992). For He II 4686 Å, the measurements yield comparable values.

Fig. 1. The total continuum-normalized spectrum of EU UMa (=RE1149+28). The observations were carried out on February 14, 1993.

Emission-Line Profiles

To study the rapid variability of spectral lines on time scales from several to several tens of minutes, we analyze the spectra taken with an exposure time of 300 s. All of these data are homogeneous in recording and reduction techniques. We used them to analyze the profile variability of the emission lines under study.

Figure 2 shows variations in the profiles of the Hβ, Hγ, and He II 4686 Å emission lines with orbital phase. The start of our observations, UT $= 00:51:27$, corresponds to zero phase when the orbital period of 90.0 min is used.

These profiles are highly variable and asymmetric in most cases. The Hβ and He II 4686 Å lines exhibit P Cyg profiles at various phases, in particular, at $\phi = 0.51$. In the phase range 0.56–0.61, the lines virtually disappear.
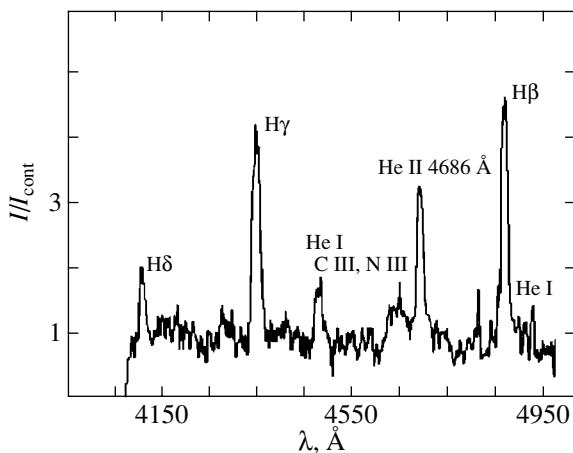
Table 2. The mean spectrophotometric parameters of emission lines

Line	EW, Å	R_c	FWHM, Å	EW, Å Mittaz *et al.* (1992)
Hγ	22.5−116; 48	2.3−8.4; 5.1	5.5−21; 10	67
He I 4471 Å	2−25; 12	0.6−4.8; 2.1	2−22; 12	27
He II 4686 Å	11.5−75; 47	1.8−8; 4.7	2.5−17; 9	42
Hβ	10−262; 80	2.5−20.5; 7.6	3−17; 9	61

Table 3. Parameters of the radial-velocity curves

Line	Method	γ, km s^{-1}	K, km s^{-1}	ϕ_0	σ, km s^{-1}
Hβ	Centroid	199(19)	370(25)	0.61(0.01)	75
Hβ	Peak	112(23)	393(29)	0.65(0.01)	89
Hγ	Centroid	174(28)	491(35)	0.57(0.01)	107
Hγ	Peak	296(64)	608(80)	0.55(0.02)	248
He I 4471 Å	Peak	55(60)	431(73)	0.74(0.03)	234
He II 4686 Å	Centroid	−1(29)	310(37)	0.65(0.02)	111
He II 4686 Å	Peak	19(34)	303(41)	0.74(0.02)	133

Table 4. The orbital period of the system

Line	Period (sine-wave fitting)	Period (Deeming's method)	Mean period
	min		
Hβ	89.55	90.50	90.025
Hγ	90.46	88.90	89.68
He I 4471 Å	90.45	90.37	90.42
	90.15 ± 0.3	89.92 ± 0.51	90.04 ± 0.2

Variations in Line Equivalent Widths and Relative Intensities with an Orbital Phase

Spectroscopy with a time resolution of 5 min allows the variations in all spectral parameters of emission lines to be traced during the orbital period. The technique for measuring the spectrophotometric parameters of emission lines in the spectra taken with the TV scanner was described by Kopylov *et al.* (1986). The measurement errors are ≈5% for the equivalent widths of lines with EW ≈20 Å, ≈5% for the central line depths R_c, and ≈4% for the line FWHMs. For weaker lines, the errors can reach 10%.

Variations in the equivalent widths and central intensities R_c of the Hβ, Hγ, and He II 4686 Å emission lines are shown in Fig. 3. We see from the figure how greatly the equivalent widths and relative intensities (R_c) of these emission lines vary with orbital phase. The equivalent-width and relative-intensity curves for the Balmer lines exhibit two sharp peaks at phases 0.15 and 0.85. The calculation of orbital phases was described above. The behavior of the line equivalent widths correlates with that of R_c. Weaker peaks are seen in the Hβ and He II 4686 Å lines in these curves near phase 0.4. We also see from these curves that the minima of all curves lie within the phase range 0.55−0.6. The FWHM curves for the emission lines exhibit peaks near phase 0.5.

The Radial Velocities of Emission Lines and Determining the Orbital Period

The true locations of the emission-line regions in polars are still the subject of debate. Many authors have shown that a narrow peak and a broad base represent different formation regions. We analyzed
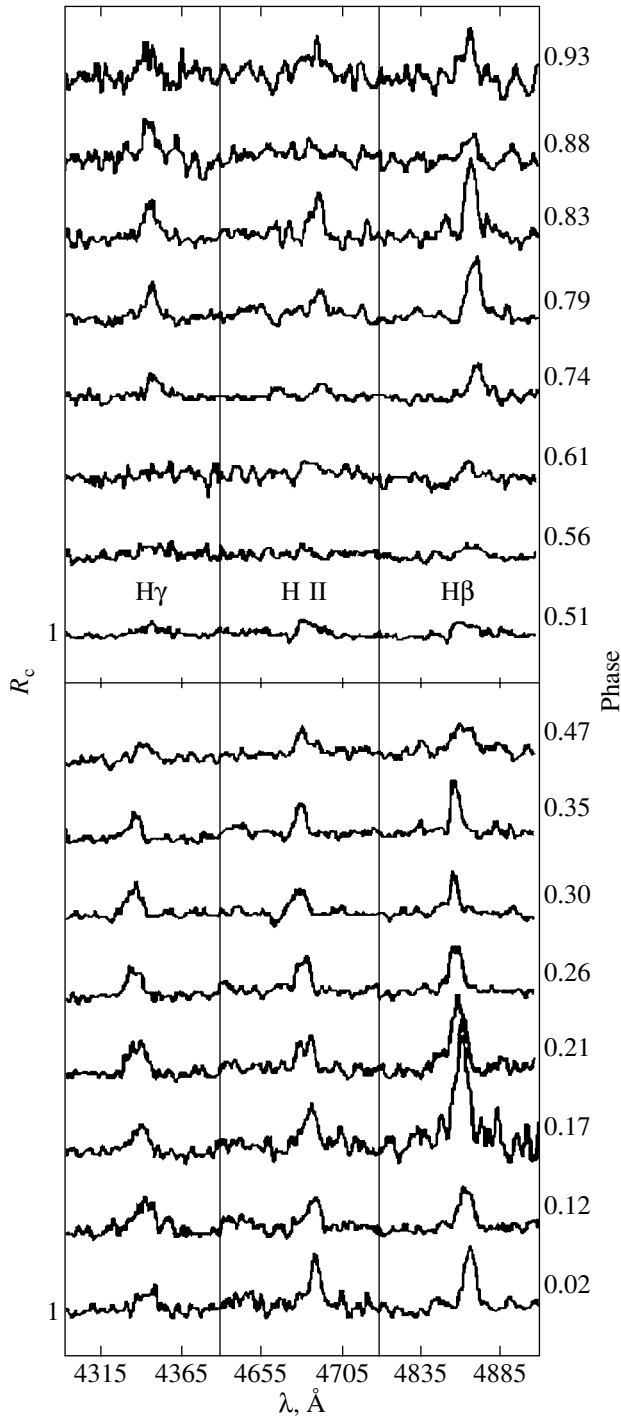
set for each of the measured lines by the least-squares method:

$$V = \gamma + K \sin[2\pi(t - t_0)/P],$$

where V is the radial velocity, γ is the γ velocity, t is the current time, the epoch $t = 0$ and $\phi = 0$ corresponds to the start of our observations, K is the semi-amplitude of the radial-velocity curve in km s^{-1}, σ is the rms deviation of all measurements from a sine wave, and P is the period. The period was varied over the range from 60 to 130 min with a 30-s step. We calculated the errors for all parameters. The minimum rms deviation from a sine wave was the criterion that the orbital period was chosen correctly. The results of our calculations for some lines are presented in Table 3. The measurement errors are given in parentheses. The second column of this table gives the method of radial-velocity measurements: centroid is the from the line centroid and peak is the from the line peak. We see from Table 3 that the differences between the radial velocities measured from the line centroids and from the emission-line peaks are small. We also see that the radial-velocity curves constructed from the velocities measured by using the helium-line peaks have the same phase shift and are displaced by $0.1P$ from the radial-velocity curves constructed from the velocities measured by using the Balmer-line peaks. Figure 4 shows the radial-velocity curve for the broad feature of the Hβ line.

We also used Deeming's method (seeking a power spectrum for the series of measurements) to determine the orbital period of EU UMa (Deeming 1975). The two methods yielded consistent results (see Table 4).

DISCUSSION

Our spectroscopic and photometric studies of EU UMa (RE1149+28) indicate that the system is a faint (17^m) object whose spectrum varies greatly with the orbital phase. This spectroscopic variability with time is illustrated by Figs. 2 and 3. These figures show line-profile variations (Fig. 2) and variations in the spectrophotometric parameters of emission lines in the spectrum with a time resolution of 300 s (Fig. 3). The spectral-line parameters vary significantly on time scales from 5 to 15 min. The rapid variations of emission features in the spectra could be associated with photometric characteristics of the system and with unsteady accretion in the polars.

The mean FWHMs are 550–700 km s^{-1} for the Balmer emission lines and about 600 km s^{-1} for the He II 4686 Å line. These values are comparable with the line FWHMs for other polars. The emission-line FWHMs are largest near phase 0.5. In the phase
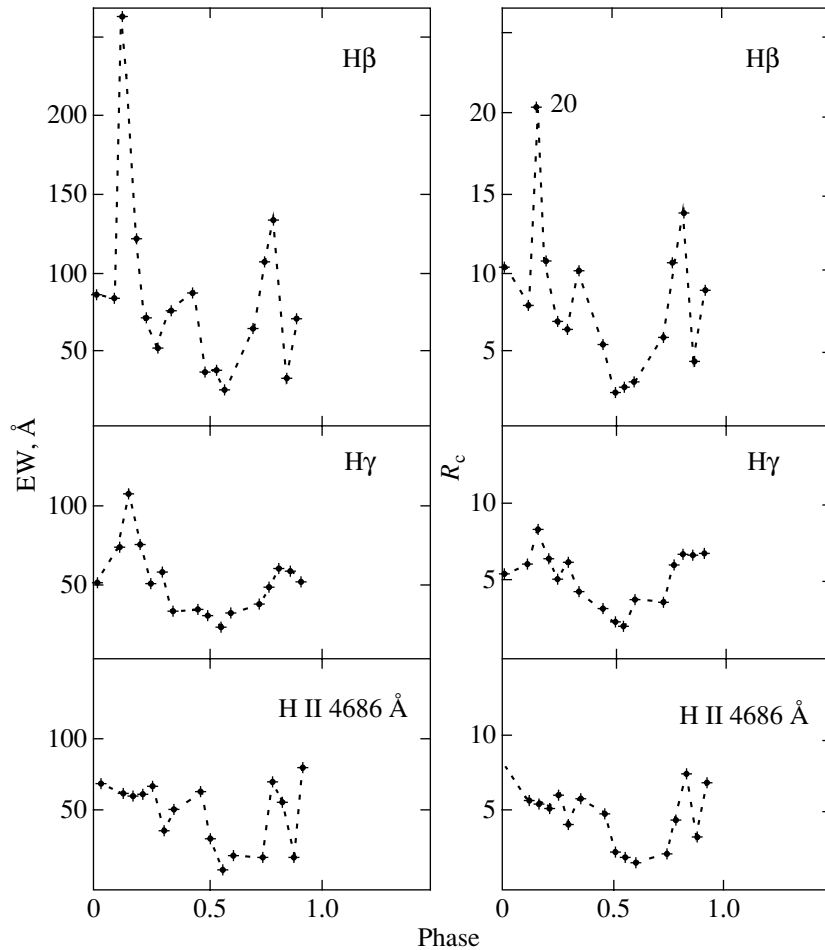

Fig. 2. The profiles of the Hβ, Hγ, and He II 4686 Å emission lines as a function of orbital phase.

the radial velocities of several emission lines. The radial velocities were measured for broad line features (from the centroids) and for narrow features (from the line peaks). The error in the radial velocities is ± 20 km s^{-1}. For weak lines, this error can double.

We constructed the following curve from the data

Fig. 3. Spectral parameters of emission lines (equivalent widths EW and relative intensities R_c) versus orbital phase.

range 0.56−0.61, the emission lines virtually disappear. An eclipse of the accretion pole or of the accretion stream by the white dwarf itself could be responsible for the disappearance of the lines. At selected phases, the Hβ and He II 4686 Å lines exhibit P Cyg profiles. These profiles may result from a superposition of atmospheric absorption lines of the white dwarf on the emission-line spectrum or from a circumstellar nonuniformity moving in the system shell.

Analysis of the radial-velocity curves for all of the lines except He II 4686 Å indicates that the orbital period of RE1149+28 is, on average, 90.15 ± 0.3 min (see Table 4). The mean period estimated by two different methods (sine-wave fitting and Deeming's method) is 90.04 ± 0.2 min (see Table 4). Thus, of the two possible periods found from the results of Mittaz *et al.* (1992), the correct period is 90 min (Bonnet-Bidaud *et al.* 1994; Somov *et al.* 1995). This is the first determination of the orbital period for EU UMa (=RE1149+28) from spectroscopic data. The soft X-ray (EUVE) observations of this system carried out by Howell *et al.* (1995) also revealed a similar period.

Interestingly, the radial velocities of the He II 4686 Å emission-line peaks yielded a radial-velocity curve with the period of 74.9 ± 2.8 min that correlates with the separation between the peaks in the curves of variations in the Balmer-line equivalent
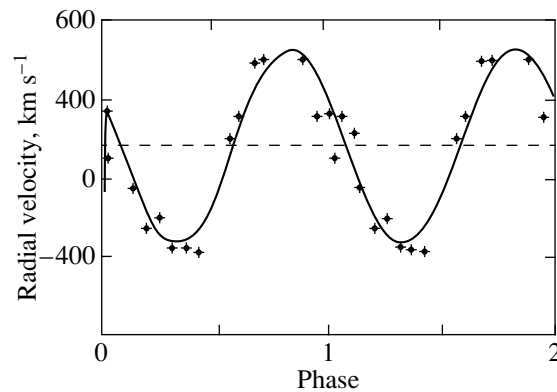

Fig. 4. The radial-velocity curve for the broad feature of the Hβ line. The curve parameters are given in Table 3.

widths and central intensities with orbital phase. The mean period estimated by the two methods is 73.5 ± 1.9 min. This period probably indicates that at least two regions contribute to the narrow feature. These could be the heated hemisphere of the red dwarf and part of the horizontal stream.

CONCLUSIONS

We analyzed the spectroscopic and photometric observations of EU UMa (=RE1149+28) carried out in February 1993 with a TV spectrophotometer (scanner) and a photometer (NEPh) at the secondary Nasmyth-1 focus of the 6-m telescope.

We obtained the following results.

(1) The orbital period of the system was estimated from spectroscopic data to be 90.0 ± 0.2 min.

(2) Our analysis of the variability of spectral parameters for Balmer lines revealed their significant variations with orbital phase. The line equivalent widths and central intensities were found to peak at phases 0.15 and 0.85. The time separation between these peaks was 72.5 min. The Balmer-line equivalent widths were at a minimum in the phase range $\approx 0.5-0.6$.

(3) The curve of variations in the equivalent widths of the He II 4686 Å line with an orbital phase exhibits no sharp peaks, as for the Balmer lines. The equivalent widths in the curve are at a minimum in the phase range $\approx 0.5-0.7$.

(4) The velocities measured from narrow features of the He II 4686 Å line yielded a mean period of 73.5 ± 1.9 min. This period correlates in duration with the separation between the peaks in the curves of variations in the hydrogen-line equivalent widths and central intensities with orbital phase. This period probably indicates that at least two regions contribute to the narrow feature. These could be the heated hemisphere of the red dwarf and part of the horizontal stream.

(5) The emission-line FWHMs peak at phase 0.5. In the phase range 0.56–0.61, the emission lines virtually disappear. An eclipse of the accretion pole or of the accretion stream by the white dwarf itself could be responsible for the disappearance of the lines.

(6) We found significant rapid variations in R_c and EW on time scales from 5 to 15 min. The rapid variations of emission features in the spectra could be associated with photometric characteristics of the system and with unsteady accretion in the polars.

(7) At selected phases, the Hβ and He II 4686 Å emission lines exhibited P Cyg profiles. These profiles suggest a possible superposition of the absorption-line spectrum from the white-dwarf atmosphere on the emission-line spectrum or the existence of a circumstellar nonuniformity moving in the system shell.

REFERENCES

1. V. L. Afanasiev, V. A. Lipovetskii, V. P. Mikhaĭlov, *et al.*, Astrofiz. Issled. (Izv. SAO) **31**, 128 (1991).
2. J. M. Bonnet-Bidaud, M. Mouchet, N. N. Somov, and T. A. Somova, Odessa Astron. Publ. **7**, 111 (1994).
3. G. Chanmugam, Annu. Rev. Astron. Astrophys. **30**, 143 (1992).
4. M. S. Cropper, Space Sci. Rev. **54**, 195 (1990).
5. T. J. Deeming, Astrophys. Space Sci. **36**, 137 (1975).
6. S. V. Drabek, I. M. Kopylov, N. N. Somov, and T. A. Somova, Astrofiz. Issled. (Izv. SAO) **22**, 64 (1986).
7. O. N. Gusev, N. G. Zandin, and M. V. Lobachev, Opt.-Mekh. Prom−st., No. 12, 63 (1976).
8. S. B. Howell, M. M. Sirk, R. F. Malina, *et al.*, Astrophys. J. **439**, 991 (1995).
9. B. K. Ioannisiani, I. M. Kopiilov, V. S. Riilov, and L. I. Snejko, *Instrumentation for Astronomy with Large Optical Telescopes,* Ed. by C. M. Humphries (Reidel, Dordrecht, 1982), p. 3.
10. I. M. Kopylov, N. N. Somov, and T. A. Somova, Astrofiz. Issled. (Izv. SAO) **22**, 77 (1986).
11. J. Liebert and H. S. Stockman, *Cataclysmic Variables and Low Mass X-ray Binaries,* Ed. by D. Q. Lamb and J. Patterson (Reidel, Dordrecht, 1985), p. 151.
12. J. P. D. Mittaz, S. R. Rosen, K. O. Mason, and S. B. Howell, Mon. Not. R. Astron. Soc. **258**, 277 (1992).
13. S. I. Neizvestny, *Photometric Systems and Standard Stars* (Moletai Astronomical Observatory, 1995), p. 37.
14. N. N. Somov, Astrofiz. Issled. (Izv. SAO) **22**, 73 (1986).
15. N. N. Somov, Author's Abstract of Candidate's Dissertation (Nizhni Arkhyz, 1988).
16. N. N. Somov, T. A. Somova, J. M. Bonnet-Bidaud, and M. Mouchet, Astron. Soc. Pac. Conf. Ser. **85**, 296 (1995).
17. T. A. Somova, N. N. Somov, S. V. Markelov, *et al.*, *Instrumentation for Astronomy with Large Optical Telescopes,* Ed. by C. M. Humphries (Reidel, Dordrecht, 1982), p. 283.
18. T. A. Somova, N. N. Somov, J. M. Bonnet-Bidaud, and M. Mouchet, *Proceedings of the International Meeting on Magnetic Fields of Chemically Peculiar and Related Stars, Moscow, 2000,* Ed. by Yu. V. Glagolevskij and I. I. Romanuk, p. 232.
19. S. Tapia, Astrophys. J. Lett. **212**, L125 (1977).
20. N. A. Vikul'ev, V. V. Zin'kovskii, B. I. Levitan, *et al.*, Astrofiz. Issled. (Izv. SAO) **33**, 158 (1991).
21. N. F. Voikhanskaya, Astrofiz. Issled. (Izv. SAO) **30**, 3 (1990).

Translated by V. Astakhov

Determining the Minimum Sum of the Component Masses for a Binary with a Known Parallax from Observations of a Short Arc of Its Apparent Motion

A. A. Kiselev and O. V. Kiyaeva[*]

Pulkovo Astronomical Observatory, Russian Academy of Sciences,
Pulkovskoe sh. 65, St. Petersburg, 196140 Russia
Received October 19, 2001; in final form, August 6, 2002

Abstract—An inequality that allows the minimum sum of the component masses for a binary, M_0, to be determined was derived from simple geometric considerations. This quantity satisfies the observed orbital motion according to Newton's law with a known parallax. The M_0 value can be calculated if the apparent-motion parameters for the components, including the curvature of the observed short orbital arc, were determined from observations. We estimated M_0 for 14 Pulkovo program stars for which the apparent orbital arc covered with observations was no less than 10°. We compare M_0 with the masses estimated from the mass–luminosity relation. A significant mass excess was found for the star ADS 10329. © *2003 MAIK "Nauka/Interperiodica"*.

Key words: *visual binaries.*

The method of apparent-motion parameters (AMPs), as applied to determining the orbits of visual binaries (Kiselev and Kiyaeva 1980), can also be used as an efficient tool for studying the kinematics and dynamics of the components of wide stellar pairs with orbital periods of ~ 1000 yr or more (Kiselev and Romanenko 1996). A necessary condition for such studies is a reliable knowledge of the following four first-order apparent-motion parameters: distance ρ, position angle θ, relative velocity μ, and its direction ψ, supplemented with the relative radial velocities of the components and with the trigonometric parallax of the star under study.

Here, we consider another unexpected application of the AMP method, which makes it possible to estimate the sum of the component masses for a visual binary with a known parallax solely from positional observations, without determining its orbit and without requiring the radial velocities of the components.

The mass estimate can be easily derived from the key formula of the PAM method

$$r^3 = k^2 \frac{\rho \rho_c \tau}{\mu^2} |sin(\psi - \theta)|. \qquad (1)$$

Here, r is the spatial separation between component A and component B and k^2 is the dynamical

constant of astrocentric motion determined from Kepler's third law

$$k^2 = 4\pi^2 (M_A + M_B). \qquad (2)$$

The dimensions of k^2 are $(\mathrm{AU})^3 \, (\mathrm{yr})^{-2}$ if the binary component masses are given in solar masses. The parameters ρ, θ, μ, and ψ mentioned above describe the relative positions and motions of the components at a fixed epoch T_0 and ρ_c is the radius of curvature of the observed short arc of the apparent orbit near T_0. The dimensions of ρ and ρ_c are arcseconds; the dimensions of μ are arcseconds per year. The quantity r is then expressed in AU. It remains to compare the magnitude of vector r calculated from dynamical considerations with its projection onto the plane of the sky r_t determined purely geometrically if the trigonometric parallax π_t is known. Clearly,

$$r \geq r_t = \frac{\rho}{\pi_t}, \qquad (3)$$

Transforming estimate (3) using (1) and (2) yields

$$M_A + M_B \geq \frac{\rho^2 \mu^2}{4\pi^2 \rho_c \pi_t^3 |\sin(\psi - \theta)|} = M_0. \qquad (4)$$

Formula (4) makes it possible to determine the minimum of M_0, the sum of the binary component masses that satisfies the observed relative motion of the components on a short arc. Using this estimate does not require knowledge of any spectroscopic or photometric parameters of the stars under study. Of

[*]E-mail: `kiyaeva@gao.spb.ru`

Table 1. Parameters of the apparent relative motion for the components of visual binaries

ADS	ΔT	T_0, year	ρ''	θ	μ	ψ	ρ_c
48 (1)	1961−1994	1978.8	$5''.940 \pm .002$	$172°.911 \pm .008$	$0''.0462 \pm .0003$	$248°.9 \pm .3$	$2''.78 \pm .14$
48 (2)	1870−1994	1936	$5.253 \pm .008$	$151.818 \pm .044$	$0.0557 \pm .0002$	$219.0 \pm .4$	$4.10 \pm .07$
2427	1920−1999	1956	$4.567 \pm .031$	$22.85 \pm .34$	$0.0324 \pm .0012$	312 ± 4	$4.6 \pm .2$
2757	1830−1995	1908	$8.406 \pm .024$	$48.86 \pm .07$	$0.0140 \pm .0006$	187 ± 3	$3.3 \pm .6$
3353	1830−1997	1909	$3.732 \pm .012$	$20.54 \pm .07$	$0.0103 \pm .0002$	328 ± 2	$3.0 \pm .5$
7551	1830−1997	1914	$2.232 \pm .011$	$307.66 \pm .28$	$0.0101 \pm .0002$	246 ± 2	$1.34 \pm .18$
8250	1833−1996	1905	$10.032 \pm .025$	$259.56 \pm .12$	$0.0205 \pm .0004$	146 ± 2	$9.4 \pm .8$
8980	1908−1991	1946	$2.713 \pm .095$	$287.09 \pm .33$	$0.0236 \pm .0015$	37 ± 9	$1.23 \pm .13$
9031	1962−1979	1972	$3.288 \pm .005$	$152.69 \pm .06$	$0.0502 \pm .0006$	$214.6 \pm .9$	$1.4 \pm .1$
9167	1831−1997	1914	$2.242 \pm .013$	$81.99 \pm .24$	$0.0173 \pm .0002$	168 ± 2	$4.8 \pm .2$
10329	1830−1995	1915	$12.028 \pm .042$	$49.41 \pm .14$	$0.0140 \pm .0005$	332 ± 4	$2.9 \pm .1$
12169	1832−1986	1903	$9.331 \pm .024$	$217.47 \pm .04$	$0.0243 \pm .0006$	74 ± 1	76 ± 9.00
15600	1832−1995	1916	$7.026 \pm .010$	$281.15 \pm .06$	$0.0165 \pm .0003$	247 ± 1	$4.0 \pm .2$
16291	1832−1997	1904	$3.774 \pm .014$	$65.22 \pm .10$	$0.0104 \pm .0002$	25 ± 1	$9.4 \pm .9$
19464 + 3201	1936−2000	1968	$3.984 \pm .010$	$131.96 \pm .10$	$0.0400 \pm .0006$	$142.0 \pm .7$	$12.4 \pm .4$

Table 2. Comparison of the minimum sum of the component masses M with the expected value of M_{Sp-L} calculated from the spectral type and luminosity

ADS	Sp_A	Sp_B	V_A	V_B	π_{Hip}	$M_{Sp-L}, M_\odot$	$M, M_\odot$
48 (1)	dK6	dM0	8.93	8.97	$0''.0851 \pm .0027$	1.0	$1.1 \pm .1$
48 (2)	dK6	dM0	8.93	8.97	$0.0851 \pm .0027$	1.0	$0.9 \pm .1$
2427	M2	M2	10.5	10.8	$0.0743 \pm .0006$	0.7	$0.3 \pm .1$
2757	K1V	K2V	7.67	8.37	$0.0408 \pm .0022$	1.6*	$2.3 \pm .6$
3353	F2V	F2V	6.56	6.68	$0.0143 \pm .0016$	3.3	5.4 ± 2.0
7551	K0	−	8.42	8.85	$0.0168 \pm .0029$	2.0	$2.3 \pm .9$
8250	G0V	K2	6.29	8.22	$0.0429 \pm .0010$	1.8	$1.6 \pm .3$
8980	M0	−	9.77	10.75	$0.0457 \pm .0027$	1.1	$0.9 \pm .2$
9031	dK6	dK6	7.04	8.2	$0.0732 \pm .0013$	1.4	$1.4 \pm .1$
9167	K2V	K2V	8.92	9.27	$0.0264 \pm .0018$	1.6*	$0.4 \pm .1$
10329	K5	M0	8.61	10.34	$0.0400 \pm .0010$	1.3	$4.0 \pm .5$
12169	G3V	G3V	5.85	6.0	$0.0402 \pm .0008$	2.4	$0.4 \pm .1$
15600	A3m	F7V	4.26	6.34	$0.0320 \pm .0007$	3.3*	$4.6 \pm .4$
16291	F5s	F4s	6.19	6.31	$0.0160 \pm .0009$	1.4	$1.6 \pm .4$
19464 + 3201	M1	−	9.74	10.7	$0.0749 \pm .0029$	0.7	$0.7 \pm .1$

* ADS 2757, 9167, and 15600 are triple stars. Given the third component, $M_{Sp-L} = 1.7 M_\odot$ for ADS 2757 (Tokovinin *et al.* 1994), $M_{Sp-L} = 2.35 M_\odot$ for ADS 9167 (Kiyaeva *et al.* 1998), and $M_{Sp-L} = 4.0 M_\odot$ for ADS 15600 (McAlister 1980).

course, knowledge of the trigonometric parallaxes with a sufficient accuracy plays a crucial role here, because the relative error in the mass estimate is at least a factor of 3 larger than the relative error of the parallax:

$$\frac{\Delta M_{A+B}}{M_{A+B}} \geq 3\frac{\Delta \pi_t}{\pi_t}. \qquad (5)$$

Thus, disregarding the AMP errors, whose effect on the mass error is much weaker, we conclude that for stars at distances up to 25 pc ($\pi_t = 0''.040$), M_0 is estimated with an accuracy of 30% if π_t was determined with an error of $\pm 0''.004$ (van Altena *et al.* 1995) and 8% if π_t was determined with an error of $\pm 0''.001$, as in the Hipparcos catalog (ESA 1997). For the Hipparcos stars at a distance of 100 pc, the error in the estimate increases to 30%.

Another important factor that affects the accuracy of the M_0 estimate is ρ_c. This parameter is difficult to determine from observations of a short arc, especially if the star under study is a wide pair with a long orbital period (500 yr or more). Therefore, our method is applicable only in those cases where the radius of curvature can be reliably determined.

In our study, we estimated M_0 for 14 visual binaries with available Hipparcos parallaxes and with dense series of positional observations at Pulkovo in 1960−2000 and at other observatories, starting from Struve, which were included in the WDS catalog of 1996 (Worley and Douglass 1997). Since astrophysical data were available for all the stars under study, we were able to estimate the sum of the masses from the mass−luminosity relation, M_{Sp-L}.

Our goal was to obtain reliable M_0 estimates from Eq. (4) and to compare them with M_{Sp-L}. The following inequality must hold: $M_{Sp-L} \geq M_0$. Otherwise, if (even with errors) M_0 is much larger than M_{Sp-L}, we conclude that there is a mass excess in the system under study. This mass excess can be attributed either to hidden mass in the system (e.g., to a dark companion) or to peculiarities of the physical nature of the stars, which lead to the breakdown of the mass−luminosity relation. In both cases, such stars are of great interest in stellar astronomy and can stimulate further research.

Our observational data are presented in Table 1, which lists the AMPs derived from series of positional observations ΔT in duration at epoch T_0. Two sets of AMPs are given for the star ADS 48: for epoch 1978.8 based on the Pulkovo observations alone and for epoch 1938.0 based on all the observations from the WDS catalog. We only used the 17-year-long Pulkovo observations (Kiselev *et al.* 1988) for ADS 9031 and all the available observations for the remaining stars.

Calculations of ρ_c for stars with slow orbital motions of their components involve difficulties requiring longer series of observations. The values of ρ_c in Table 1 were mostly calculated by using the exact formula with the second derivatives of ρ and θ

$$\rho_c = \frac{\mu^3}{\dot{\theta}(\mu^2 + \dot{\rho}^2) + \rho(\dot{\rho}\ddot{\theta} - \ddot{\rho}\dot{\theta})}. \qquad (6)$$

In all cases, these calculations were checked by approximate calculations, using a formula that reproduced the definition of curvature in differential geometry:

$$K = \frac{1}{\rho_c} = \frac{d\psi}{d\sigma}. \qquad (7)$$

Here, $d\sigma$ is the element of the apparent orbital arc that corresponds to the change in the tangent direction, $d\psi$. Thus, we managed to minimize the probable error of ρ_c determined from observations. Our results are presented in Table 2. The estimated sum of the masses M_0 is given with errors that include only the errors in the trigonometric parallaxes and in the radii of curvature. The sum of the masses estimated from the mass−luminosity relation, M_{Sp-L}, were reconciled with data from Kulikovskii (1985). We took astrophysical data for the individual components from the WDS catalog and the parallaxes from the Hipparcos catalog.

Comparison of M_{Sp-L} and M_0 shows that, in most cases, $M_0 < M_{Sp-L}$, which confirms the good agreement between the results independently obtained from astrophysics and geometry. However, in two cases, ADS 3353 and ADS 10329, the M_0 estimates clearly exceed M_{Sp-L} by 1 or 2 solar masses. The mass excess derived for ADS 3353 is equal to the error in M_0. As regards ADS 10329, we may be dealing with hidden mass in the system. Further studies of this star are desirable.

The multiple stars ADS 2757 and ADS 15600, for which $M_0 > M_{Sp-L}$, but within the error limits, are also noteworthy. Studies of these stars indicate that component B of ADS 2757 is a spectroscopic binary (Tokovinin *et al.* 1994) and component A of ADS 15600 is a speckle binary (McAlister 1980).

CONCLUSIONS

We proposed a method to determine a lower limit for the sum of the component masses for a binary with a known parallax if the parameters of the relative motion of its components, including the curvature of the observed short arc, were determined from observations. The method makes it possible to detect binaries with an excess mass compared to that expected from the mass−luminosity relation even if the orbital period

of the star is longer that 500 yr and if its orbit has not been determined at all.

We applied our method to 14 visual binaries of the Pulkovo program. One system with a mass excess of $\sim 2M_\odot$ was found. At present, the applicability of our method has been significantly enhanced in connection with the availability of highly accurate Hipparcos parallaxes.

REFERENCES

1. European Space Agency (ESA), SP-1200 (1997).
2. A. A. Kiselev and O. V. Kiyaeva, Astron. Zh. **57**, 1227 (1980) [Sov. Astron. **24**, 708 (1980)].
3. A. A. Kiselev and L. G. Romanenko, Astron. Zh. **73**, 875 (1996) [Astron. Rep. **40**, 795 (1996)].
4. A. A. Kiselev, O. A. Kalinichenko, G. A. Plyugin, *et al.*, *Catalog of Relative Positions and Motions of 200 Visual Binary Stars* (Nauka, Leningrad, 1988).
5. O. V. Kiyaeva, A. A. Tokovinin, and O. A. Kalinichenko, Pis'ma Astron. Zh. **24**, 868 (1998) [Astron. Lett. **24**, 753 (1998)].
6. P. G. Kulikovskii, *Stellar Astronomy* (Nauka, Moscow, 1985).
7. H. A. McAlister, Astrophys. J. **236**, 522 (1980).
8. A. A. Tokovinin, A. Duquennoy, J.-L. Halbwachs, and M. Mayor, Astron. Astrophys. **282**, 831 (1994).
9. W. F. van Altena, J. T. Lee, and E. D. Hoffleitz, *The General Catalogue of Trigonometric Stellar Parallaxes* (Yale University Observatory, New Haven, 1995, 4th ed.).
10. C. E. Worley and G. G. Douglass, Astron. Astrophys., Suppl. Ser. **125**, 523 (1997).

Translated by N. Samus'

Dynamics of Rotating Triple Systems

M. J. Valtonen[1], A. A. Mülläri[1], V. V. Orlov[2*], and A. V. Rubinov[2]

[1]*Department of Physics and Department of Information Technologies, Turku University, Turku, Finland*
[2]*Astronomical Institute, St. Petersburg State University,*
Universitetskii pr. 28, Petrodvorets, 198504 Russia
Received July 9, 2002

Abstract—We investigate the dynamical evolution of $100\,000$ rotating triple systems with equal-mass components. The system rotation is specified by the parameter $w = -c^2 E$, where c and E are the angular momentum and total energy of the triple system, respectively. We consider $w = 0.1, 1, 2, 4, 6$ and study $20\,000$ triple systems with randomly specified coordinates and velocities of the bodies for each w. We consider two methods for specifying initial conditions: with and without a hierarchical structure at the beginning of the evolution. The evolution of each system is traced until the escape of one of the bodies or until the critical time equal to 1000 mean system crossing times. For each set of initial conditions, we computed parameters of the final motions: orbital parameters for the final binary and the escaping body. We analyze variations in the statistical characteristics of the distributions of these parameters with w. The mean disruption time of triple systems and the fraction of the systems that have not been disrupted in 1000 mean crossing times increase with w. The final binaries become, on average, wider at larger angular momenta. The distribution of their eccentricities does not depend on w and generally agrees with the theoretical law $f(e) = 2e$. The velocities of the escaping bodies, on average, decrease with increasing angular momentum of the triple system. The fraction of the angles between the escaping-body velocity vector and the triple-system angular momentum close to $90°$ increases with w. Escapes in the directions opposite to rotation and prograde motions dominate at small and large angular momenta, respectively. For slowly rotating systems, the angular momentum during their disruption is, on average, evenly divided between the escaping body and the final binary, whereas in rapidly rotating systems, about 80% of the angular momentum is carried away by the escaping component. We compare our numerical simulations with the statistical theory of triple-system disruption. © *2003 MAIK "Nauka/Interperiodica"*.

Key words: *celestial mechanics, triple systems, dynamical evolution, simulations.*

INTRODUCTION

Triple systems are widely represented among stars and galaxies. Therefore, the dynamical evolution of such systems has long attracted the attention of researchers [see, e.g., Anosova and Orlov (1985), Valtonen (1988), and Valtonen and Mikkola (1991) for a review].

The dynamical disruption of triple systems can be analyzed both numerically and in terms of the statistical theory of disruption (Monaghan 1976a, 1976b; Nash and Monaghan 1978). This approximate theory is based on the assumption that the phase trajectory of a triple system is quasi-ergodic within the region of strong body interaction (a close triple encounter). The probability of escape with certain parameters of the final state (orbital elements of the final binary and the escaping body) is then proportional to the corresponding volume of phase space in a coordinate system associated with the center of mass of the triple system for the chosen integrals of motion. Another simplifying assumption of this theory is the absence of interaction between the escaping body and the remaining binary.

In several cases, comparison of the theoretical distributions of disruption parameters and numerical simulations shows good agreement, suggesting that the quasi-ergodic hypothesis is suitable for describing the results of close triple encounters that lead to the disruption of triple systems. It is of interest to determine the validity range for the statistical theory of disruption by comparing its predictions with numerical simulations.

The dynamical evolution of rotating triple systems has been numerically simulated for more than 30 years (see, e.g., Anosova 1969; Standish 1972; Saslaw *et al.* 1974; Valtonen 1974; Anosova *et al.* 1984; Mikkola and Valtonen 1986; Anosova and Orlov 1986). These authors showed that an increase
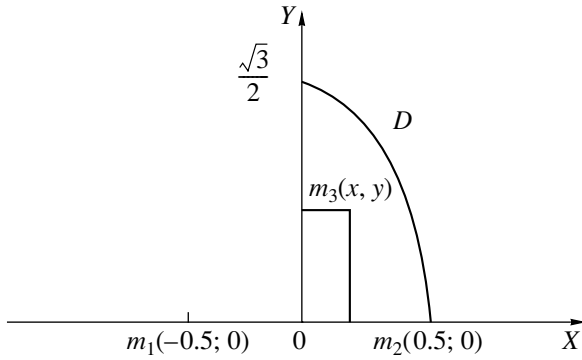
*E-mail: vor@astro.spbu.ru

Fig. 1. The domain of all possible configurations of triple systems.

in angular momentum, on average, causes the dynamical evolution to slow down and the fraction of stable hierarchical triple systems to increase.

Comparison of the statistical theory of disruption with numerical simulations (Monaghan 1976b; Nash and Monaghan 1978) shows the qualitative agreement of the theoretical distributions of eccentricity and binding energy for the final binary and the magnitude of the velocity for the escaping body with their distributions derived from the statistical theory of disruption. As the angular momentum of a triple system increases, the escape direction tends to be orthogonal to the angular momentum vector of the triple system (the angle θ between these vectors is close to $90°$), which is in qualitative agreement with the numerical simulations of Valtonen (1974).

Here, we consider the dynamical evolution of rotating triple systems in three-dimensional space. We constructed the distributions for several parameters that characterize the final states of the disrupted systems and compare our results with the statistical theory of disruption.

THE MODEL

We consider the evolution of triple systems with equal-mass components. The rotation is specified by the parameter

$$w = -c^2 E, \qquad (1)$$

where c and E are the magnitude of the angular momentum vector and the total energy of the triple system, respectively. This parameter was also used by Mikkola and Valtonen (1986).

We use the following system of units: the gravitational constant $G = 1$, the body masses $m_1 = m_2 = m_3 = 1$, and $E = -1$.

We consider two different methods of specifying the initial conditions.

The first method is similar to that used by Mikkola and Valtonen (1986). The dynamical evolution begins with the encounter of a single body with a close binary along an elliptical orbit with a low binding energy compared to the binding energy of the inner binary; i.e., at the beginning of the evolution, the triple system has an hierarchical structure.

The second method for specifying the initial conditions does not assume any mandatory hierarchical structure. The initial configuration is chosen randomly from the domain D (Fig. 1): the coordinates of the third body are chosen uniformly randomly from the segment bounded by the coordinate axes and by the arc of a circumference of unit radius centered at point $(-0.5, 0)$; the positions of the first and the second bodies are fixed at points $(-0.5, 0)$ and $(+0.5, 0)$, respectively. The domain D includes all possible configurations of triple systems (see, e.g., Agekyan and Anosova 1967). The initial velocities are chosen isotropically, with the virial coefficient k being distributed uniformly randomly over the interval $(0, 1)$.

In both methods of specifying the initial conditions, the value of $w(1)$ is fixed and the initial conditions for which w differs from the assumed value by no more than 0.01 are chosen. We considered $w = 0.1, 1, 2, 4, 6$. For each w and each choice of initial conditions, we traced the evolution of 10 000 triple systems. A total of 100 000 sets of initial conditions were considered. Our computations lasted until one of the bodies escaped from the triple system along a hyperbolic orbit or until the critical time 1000τ was reached, where

$$\tau = \frac{GM^{5/2}}{|2E|^{3/2}} \qquad (2)$$

is the mean crossing time of the triple system. Here, M is the total mass of the triple system and G is the gravitational constant. The quantity τ is the characteristic time in which the component moving at the characteristic velocity crosses the system (see, e.g., Valtonen 1988).

Below, the parameters with the dimensions of length are expressed in units of the mean system size

$$d = \frac{G(m_1 m_2 + m_1 m_3 + m_2 m_3)}{|E|}, \qquad (3)$$

and the parameters with the dimensions of velocity are given in units of d/τ.

THE RESULTS OF NUMERICAL SIMULATIONS

We determined the following parameters for the disrupted triple systems: the lifetime T of the triple

Mean disruption parameters

w	0.1	1	2	4	6
n_H	9814	9543	8700	4591	883
n_D	9839	9705	9447	7269	4692
$\overline{T}_H$	49.4 ± 1.0	80.0 ± 1.4	120.5 ± 2.0	190.9 ± 3.8	274.2 ± 10.4
$\overline{T}_D$	44.0 ± 0.9	82.7 ± 1.3	112.5 ± 1.7	160.2 ± 2.6	61.9 ± 2.6
$\bar{a}_H$	0.1164 ± 4	0.1349 ± 3	0.1429 ± 2	0.1556 ± 2	0.1636 ± 1
$\bar{a}_D$	0.0976 ± 5	0.1270 ± 3	0.1349 ± 3	0.1404 ± 4	0.1201 ± 6
$\bar{e}_H$	0.710 ± 2	0.689 ± 2	0.705 ± 2	0.722 ± 3	0.634 ± 6
$\bar{e}_D$	0.695 ± 2	0.695 ± 2	0.699 ± 2	0.712 ± 2	0.707 ± 3
$\overline{V}_H$	2.22 ± 2	1.50 ± 1	1.22 ± 1	0.76 ± 1	0.39 ± 1
$\overline{V}_D$	4.04 ± 5	2.02 ± 2	1.69 ± 2	1.51 ± 2	2.34 ± 3
$\overline{\theta}_H$	90.2 ± 3	90.0 ± 1	90.1 ± 1	89.9 ± 1	90.0 ± 1
$\overline{\theta}_D$	90.0 ± 3	89.9 ± 1	90.0 ± 1	90.1 ± 1	90.0 ± 1
$\overline{\lambda}_H$	114.8 ± 4	90.4 ± 4	83.2 ± 4	62.0 ± 4	36.3 ± 5
$\overline{\lambda}_D$	110.6 ± 4	84.3 ± 4	75.0 ± 4	60.1 ± 4	75.9 ± 6
$\bar{\beta}_H$	1.13 ± 2	0.310 ± 1	0.219 ± 1	0.165 ± 1	0.170 ± 1
$\bar{\beta}_D$	0.731 ± 4	0.274 ± 1	0.200 ± 1	0.144 ± 1	0.108 ± 1

system, the semimajor axis a of the final binary, the eccentricity e of the final binary, the asymptotic velocity V of the escaping body, the angle θ between the orbital angular momentum vector of the triple system and the velocity vector of the escaping body, the angle λ between the angular momentum vectors of the final binary and the binary formed by the escaping body and the center of mass of the final binary, and the ratio β of the angular momentum of the final binary to the angular momentum of the outer binary formed by the escaping body and the barycenter of the final binary.

The table lists the mean values of these parameters for the two methods of choosing the initial conditions and the w values considered here. The subscript "H" in the first column corresponds to hierarchical systems (the first method of choosing the initial conditions); the subscript "D" refers to the second method (the initial configuration in the domain D). The first two rows give the number of systems disrupted in a time $T < 1000\tau$. Based on these systems, we computed the mean disruption parameters and constructed their distributions.

As we see from the table, the fraction of the systems that were not disrupted in time 1000τ increases with the angular momentum of the triple system. Note that this increase is much larger for hierarchical systems. For $w = 6$, the fraction of the hierarchical systems disrupted in time $T < 1000\tau$ is less

than 10%, whereas this fraction is slightly less than 50% for the second method of specifying the initial conditions. This difference probably results from the emergence of a significant number of nonhierarchical systems disrupted in a short time, whereas among hierarchical systems such initial conditions are much fewer in number. This is probably the reason why the mean lifetime greatly decreases at $w = 6$ for the second method of choosing the initial conditions.

The final binaries become, on average, wider and the velocities of the escaping bodies, accordingly, decrease with increasing angular momentum. In the second method of specifying the initial conditions, the final binaries are, on average, closer and the velocities of the escaping bodies are higher than those for hierarchical systems. This may be because the interaction between the components and the energy redistribution between the escaping body and the final binary in systems with nonhierarchical initial configurations are more intense than those in hierarchical systems.

The mean eccentricities of the final binaries are almost independent of w and of the method for choosing the initial conditions. The mean $\bar{e} \approx 0.7$. Only $\bar{e} = 0.634 \pm 0.006$ for hierarchical triple systems constitutes an exception. Here, the final binaries are, on average, less eccentric.

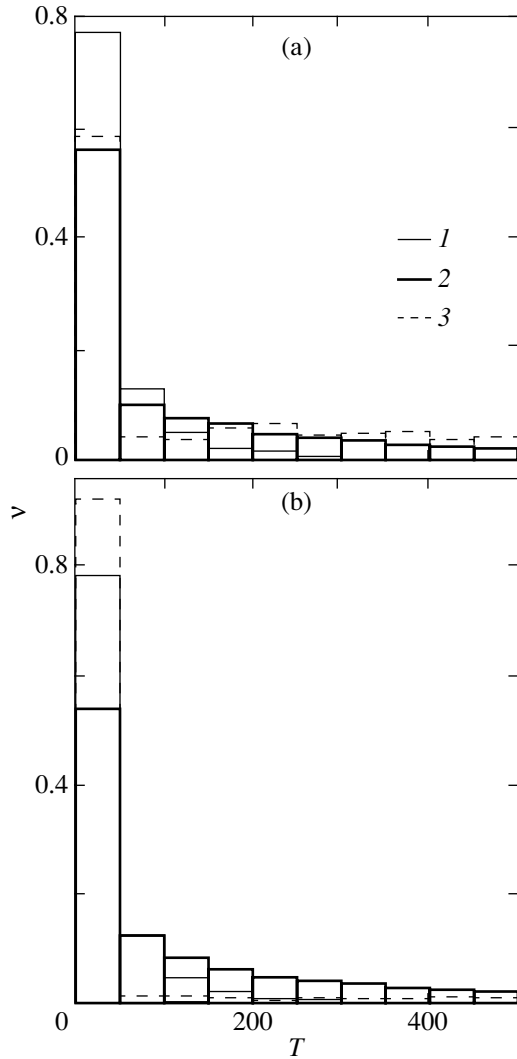The mean angles θ are close to 90°, irrespective of the method of choosing the initial conditions.

Fig. 2. The distributions of triple-system disruption times for the first (a) and second (b) method of specifying the initial conditions: *1* is $w = 0.1$; *2* is $w = 2$; and *3* is $w = 6$.
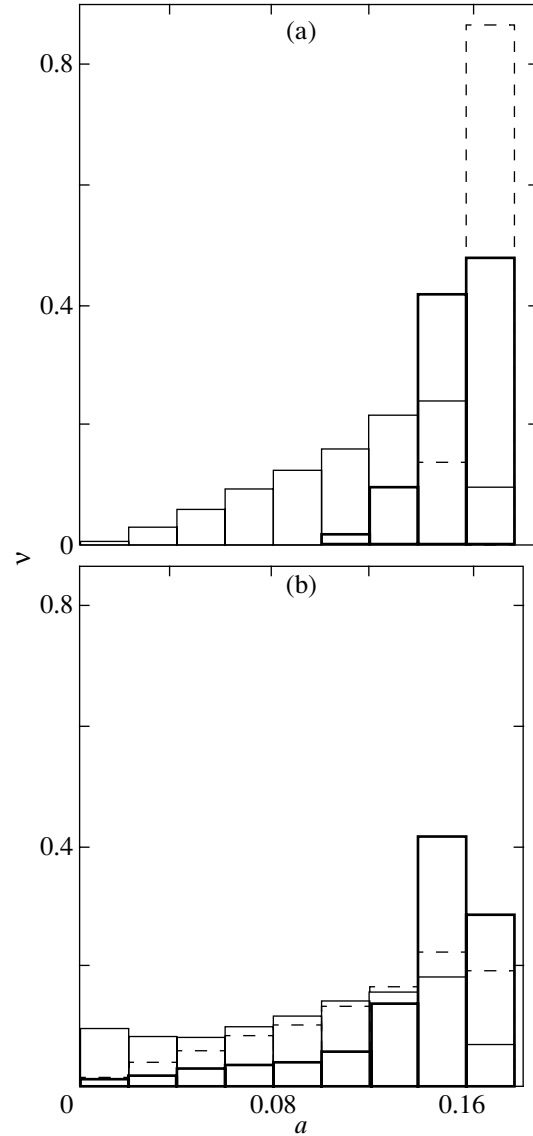

Fig. 3. The distributions of semimajor axes of the final binaries. The notation is the same as that in Fig. 2.

In slowly rotating systems ($w = 0.1$), body escapes in the direction opposite to the rotation of the final binary ($\bar{\lambda} > 90°$) generally dominate, whereas in rapidly rotating systems ($w > 1$), more escapes take place in the direction of the rotation of the final binary ($\bar{\lambda} < 90°$). The values of $\bar{\lambda}_H$ and $\bar{\lambda}_D$ generally agree, although for initially hierarchical systems, $\bar{\lambda}_H$ is slightly larger than $\bar{\lambda}_D$, except for the case $w = 6$, where $\bar{\lambda}_H$ is much smaller than $\bar{\lambda}_D$.

The angular momentum is redistributed almost equally between the final binary and the binary formed by the escaping body and the barycenter of the final binary for both methods of choosing the initial conditions. For hierarchical systems, this ratio is, on average, slightly larger than that for nonhierarchical systems. The mean $\bar{\beta}_H$ and $\bar{\beta}_D$ decrease with

increasing angular momentum of the system. This is probably because the escaping body carries away excess angular momentum.

Let us consider the distribution functions for the parameters of the final states of triple systems. These distributions are shown in Figs. 2–8. Figures 2a, 3a, 4a, 5a, 6a, 7a, and 8a and 2b, 3b, 4b, 5b, 6b, 7b, and 8b correspond to the first (hierarchical systems) and second (systems without mandatory initial hierarchy) methods of specifying the initial conditions. The parameter bins and the fractions ν of triple systems in these bins are plotted along the x and y axes, respectively.

In general, the parameter distributions for the first and second methods of choosing the initial conditions
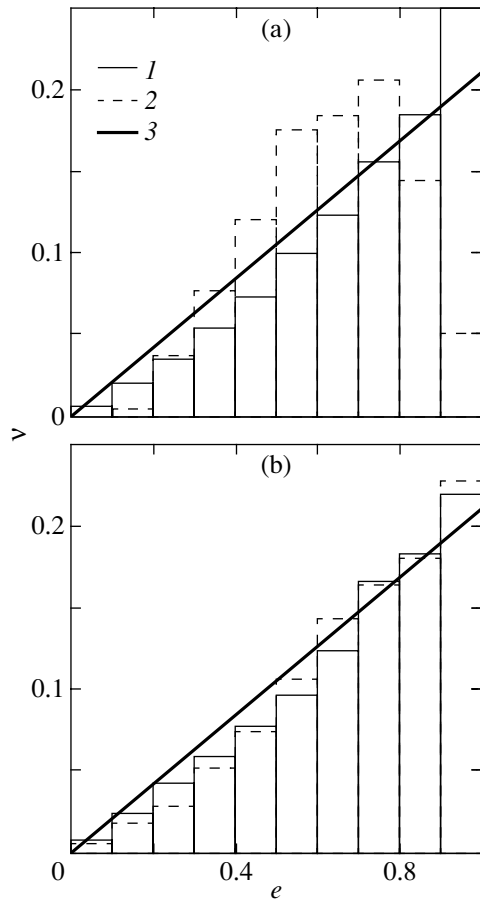
Fig. 4. The distributions of eccentricities of the final binaries for the two methods of specifying the initial conditions (a) and (b) at $w = 0.1$ (*1*) and $w = 6$ (*2*); *3* is the theoretical distribution $f(e) = 2e$.
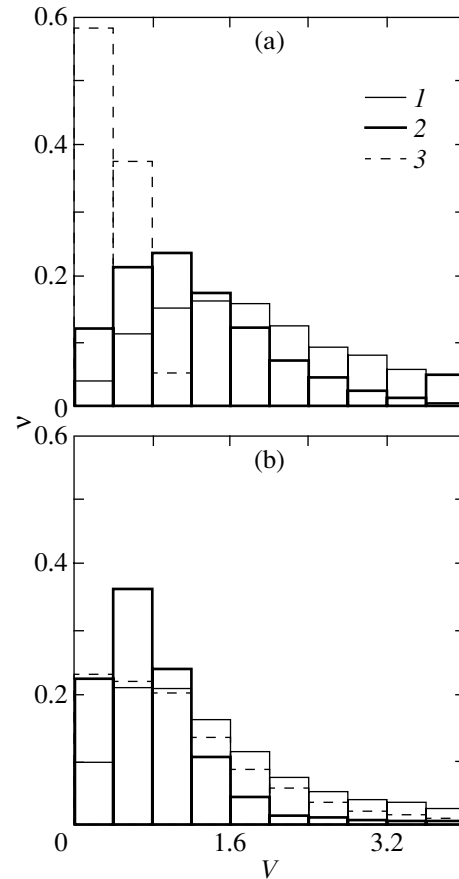

Fig. 5. The velocity distributions for the escaping body for two methods of specifying the initial conditions (a) and (b) at $w = 0.1$ (*1*), $w = 2$ (*2*), and $w = 6$ (*3*).

agree. The general trends of variations in the distributions with w correspond to the trends of variations in the mean parameters (see the table).

Most of the systems are disrupted in time $T < 50\tau$; the fraction of the systems with long lifetimes generally increases with w (the "tail" of the distribution becomes more powerful). Only the distribution $f(T_D)$ for the second method of specifying the initial conditions at $w = 6$ constitutes an exception. Note that $w = 6$ is close to the critical value of $w_{cr} = 6.25$, which corresponds to the instability threshold of a triple system with respect to hierarchy violation (see, e.g., Szebehely and Zare 1977). At $w > w_{cr}$, the triple systems appear to be separated into two categories: (1) stable triple systems and (2) unstable triple systems where one of the bodies escapes in a short time without hierarchy violation. As the stability threshold w_{cr} is approached, the triple systems break up into three classes: (1) nearly stable triple systems with long lifetimes $T > 1000\tau$, (2) unstable systems

with fast escape of one of the bodies, and (3) the intermediate class of unstable systems.

For hierarchical triple systems (see Fig. 2a and the table), the fraction of the systems with fast escape of one of the bodies is small, about 5% of the entire sample of initial conditions. More than 90% of the systems were not disrupted in time 1000τ. For the second method of specifying the initial conditions (see Fig. 2b and the table), the fraction of the systems being rapidly disrupted is about 40% of the total number of systems and more than 80% of the systems that were disrupted in time $T < 1000\tau$. This is also the reason why the mean lifetime $\bar{T}_D$ decreases as one passes from $w = 4$ to $w = 6$. The result obtained probably suggests that in nonhierarchical systems with large angular momentum, one of the bodies often rapidly escapes, whereas in hierarchical systems, such situations are much rarer. The results for hierarchical and nonhierarchical systems (the mean lifetimes and their distribution functions) become closer with decreasing angular momentum.

The preference of the $w = 6$ case for nonhierarchical systems also shows up in the distributions of a, V,
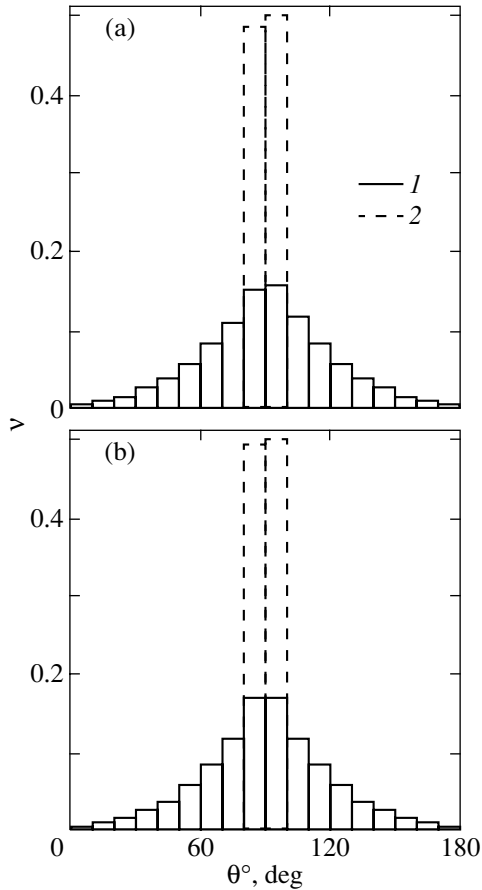
Fig. 6. The distributions of the angle between the orbital angular momentum vector of the triple system and the velocity vector of the escaping body for the two methods of specifying the initial conditions (a) and (b) at $w = 0.1$ (*1*) and $w = 6$ (*2*).
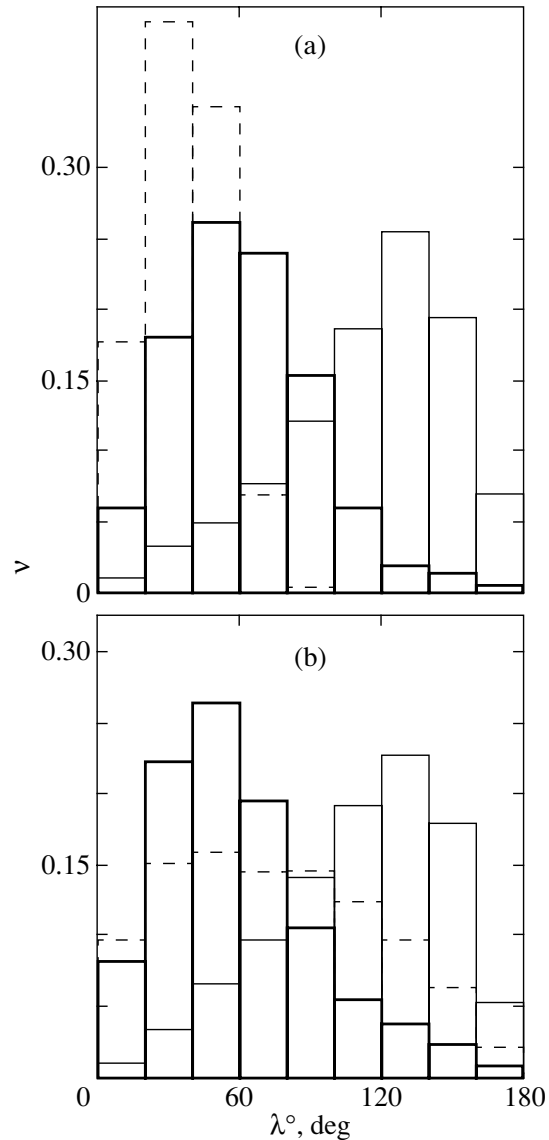

Fig. 7. The distributions of the angle between the orbital planes of the final binary and the escaping body. The notation is the same as that in Fig. 5.

and λ (see Figs. 3, 5, and 7 and the table). At $w = 6$, the final binaries formed during the disruption of non-hierarchical systems become, on average, closer and the escaping bodies carry away more kinetic energy than in the $w = 4$ case (see Figs. 3b and 5b), whereas for hierarchical systems the tendency for the final binaries to widen and for the escape velocity to decrease with increasing w is preserved (see Figs. 3a and 5a). For nonhierarchical systems with $w = 6$, the tendency for the angles λ to decrease (i.e., for prograde motions of the escaping body and the remaining pair to dominate) gives way to their increase. This may be because for systems being rapidly disrupted, the numbers of prograde and retrograde escapes are approximately equal (see Fig. 9).

The distributions of eccentricities for the final binaries are virtually independent of w (Fig. 4). They agree with the theoretical distribution for the probability density

$$f(e)de = 2ede, \qquad (4)$$

which corresponds to the dissociative equilibrium of binaries in a stellar field (see Ambartsumyan 1937; Heggie 1975). The straight lines in Fig. 4 correspond to this distribution. The distribution of eccentricities for the final binaries formed during the disruption of hierarchical systems with large angular momentum at $w = 6$ (Fig. 4a) constitutes an exception. In this case, no highly eccentric binaries with $e > 0.9$ are formed and the distribution peak is located at $e \approx 0.6$.

The distributions of the angle θ are symmetric about $\theta = 90°$ (Fig. 6). The concentration of the distribution toward $\theta = 90°$ increases with w: body escapes generally occur near the stationary Laplace
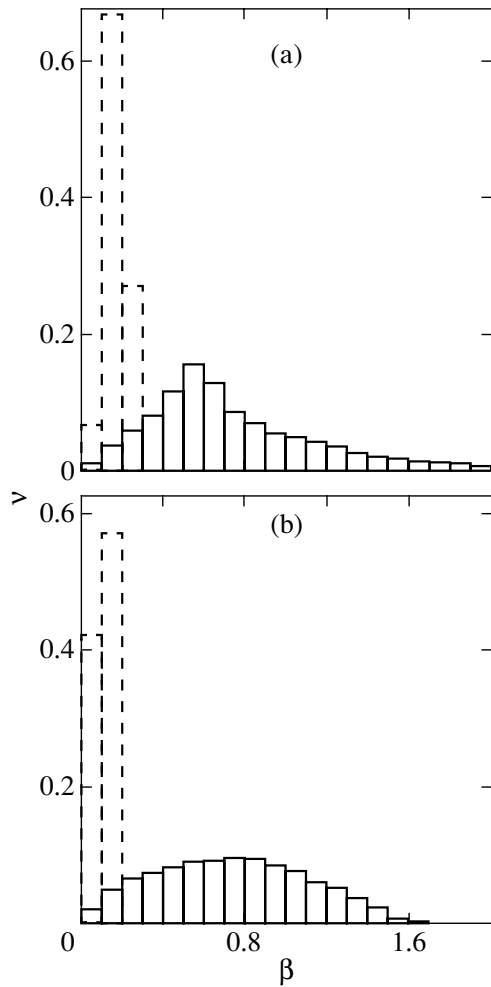
Fig. 8. The distributions of the ratio of angular momenta for the final binary and the binary formed by the escaping body and the barycenter of the final binary. The notation is the same as that in Fig. 6.
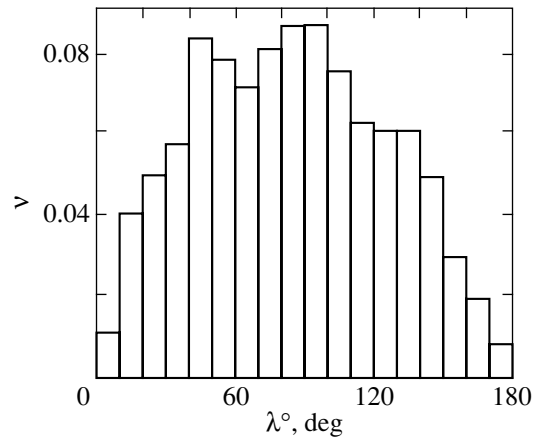

Fig. 9. The distributions of the angle λ between the angular momentum vectors of the final binary and the escaping body at $w = 6$ for systems with lifetimes $T < 5$ for the second method of choosing the initial conditions.
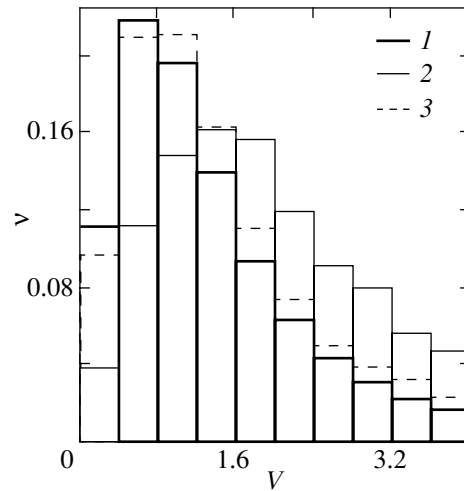

Fig. 10. The velocity distributions for the escaping body: theoretical distribution (*1*), at $w = 0.1$ for the first (*2*) and second (*3*) methods of specifying the initial conditions.

plane. Fast rotation hinders escapes in other directions.

The distributions of λ (Fig. 7) show that in slowly rotating triple systems ($w = 0.1$), escapes in the directions opposite to the rotation of the triple system ($\lambda > 90°$) dominate, because the rotations of the inner and outer binaries are mutually compensated. In rapidly rotating systems ($w \geq 1$), escapes more commonly occur in the direction of rotation of the triple system; rotation supplies additional energy to the escaping body.

The angular momentum is redistributed between the outer and inner binaries differently for slowly and rapidly rotating systems (see Fig. 8 and the table). Whereas in slowly rotating systems ($w = 0.1$) the angular momentum is, on average, evenly distributed, in rapidly rotating systems ($w \geq 2$) the lion's share (on average, from 80% to 90%) is carried away by the escaping body and only from 10% to 20% of the angular momentum remains in the final binary.

ANALYTIC APPROXIMATIONS OF THE DISTRIBUTIONS

The Eccentricities of Final Binaries

In the statistical theory of disruption of triple systems (Monaghan 1976a, 1976b; Nash and Monaghan 1978), the eccentricity distributions for the final binaries were obtained as a function of the triple-system angular momentum. The distribution function of eccentricities for three-dimensional motions with small angular momentum is given by formula (4). Comparison with numerical simulations (see Fig. 4

and the table) shows that this law agrees with the simulations. The fraction of the final binaries with highly eccentric orbits decreases with increasing angular momentum (Nash and Monaghan 1978). This result also qualitatively agrees with the numerical simulations of hierarchical triple systems at $w = 6$ (Fig. 4a). At the same time, for nonhierarchical systems, the function $f(e) = 2e$ satisfactorily describes the simulation results for all of the w values considered.

The Velocities of Escaping Bodies

In the statistical theory of disruption, the velocity distributions for the escaping bodies are unimodal; as the angular momentum increases, the peak shifts toward higher velocities (Nash and Monaghan 1978). In the numerical models, the distribution is also unimodal (Fig. 5), however, the peak shifts toward lower velocities as the angular momentum increases. This discrepancy probably stems from the fact that at small angular momentums, the triple encounters that result in escapes are closer than those in the cases of fast rotation [see, e.g., Anosova and Orlov (1985) for a review]. For a small angular momentum, the theoretical distribution $f(V)$ peaks at $V = 2/3$ (in our system of units). This value does not differ greatly from the corresponding values for the model distributions at $w = 0.1$ (see Fig. 5).

The theoretical distribution itself is (Monaghan 1976a)

$$f(V) = \frac{3}{2} \frac{V}{(1 + 3/4V^2)^2}. \qquad (5)$$

Figure 10 shows a plot of this distribution (heavy solid line) and, for comparison, histograms of the model distributions at $w = 0.1$ for the first (solid line) and second (dashed line) methods of specifying the initial conditions. The theoretical distribution agrees with the numerical simulations of nonhierarchical systems (dashed line) but shifts to the left of the model distribution for hierarchical systems. The mean for the theoretical distribution (5) is equal to $\bar{V} = \pi/\sqrt{3} \approx 1.81$. This value is closer to $V_H = 2.22$, whereas, as was pointed out above, the form of the theoretical distribution is closer to the model function for nonhierarchical systems.

The Escape Angle

Nash and Monahgan (1978) obtained theoretical distributions of the angle θ between the velocity vector of the escaping body and the angular momentum vector of the triple system. These distributions are symmetric about $\theta = 90°$, as are the model distributions (see Fig. 6). The peaks of the theoretical

distributions become sharper with increasing angular momentum, which is also in agreement with the numerical simulations.

CONCLUSIONS

We numerically simulated the dynamical evolution of 100 000 rotating triple systems. The following two methods of specifying the initial conditions were considered:

(1) Hierarchical systems in which the encounter of a single body with a binary system takes place at the beginning of the evolution; and

(2) Triple systems with randomly chosen configurations in the domain D (Fig. 1) with an isotropic velocity distribution of the bodies.

Our analysis of the final states for disrupted triple systems showed that the results for the two methods of specifying the initial conditions generally agree.

The following evolutionary trends are observed as the angular momentum of a triple system increases:

(1) The fraction of the systems that were not disrupted in time 1000τ increases.

(2) The mean lifetime of the systems being disrupted increases.

(3) The final binaries generally become wider.

(4) The velocities of the escaping bodies during disruption, on average, decrease.

(5) Body escapes occur, on average, closer to the Laplace plane and in the direction of rotation of the triple system.

(6) The fraction of the angular momentum carried away by the escaping body increases and the ratio of the final-binary and triple-system angular momenta decreases.

We compared the numerical simulations with the statistical theory of disruption for triple systems.

The form of the eccentricity distribution for the final binaries is almost independent of the angular momentum and agrees with the theoretical distribution $f(e) = 2e$, which is valid for small angular momenta (Monaghan 1976a). Only hierarchical systems with $w = 6$, where no highly eccentric binaries with $e > 0.9$ are formed, constitute an exception.

The general forms of the theoretical and model distributions of escape velocities are in agreement. These distributions have one peak. However, the tendencies for the forms of the distributions to change with increasing w are different. The theoretical distributions shift toward higher velocities, whereas in model systems, the escape velocities, on average, decrease. This discrepancy may be due to the different degree of closeness of triple encounters for slowly and rapidly rotating triple systems. Closer triple encounters in

slowly rotating systems increase the probability of escapes with high velocities. The statistical theory of disruption, which assumes all encounters to be equally close, appears to ignore this effect.

The distributions of angles θ qualitatively agree and have a similar dependence on angular momentum: the larger the triple-system angular momentum, the stronger the concentration of the escape angles to $90°$.

ACKNOWLEDGMENTS

REFERENCES

1. T. A. Agekyan and Zh. P. Anosova, Astron. Zh. **44**, 1261 (1967) [Sov. Astron. **11**, 1006 (1967)].
2. V. A. Ambartsumyan, Astron. Zh. **14**, 207 (1937).
3. Zh. P. Anosova, Tr. Astron. Obs. Leningr. Gos. Univ. **26**, 88 (1969).
4. Zh. P. Anosova, D. I. Bertov, and V. V. Orlov, Astrofizika **20**, 327 (1984).
5. Zh. P. Anosova and V. V. Orlov, Tr. Astron. Obs. Leningr. Gos. Univ. **40**, 66 (1985).
6. Zh. P. Anosova and V. V. Orlov, Astron. Zh. **63**, 643 (1986) [Sov. Astron. **30**, 380 (1986)].
7. D. C. Heggie, Mon. Not. R. Astron. Soc. **173**, 729 (1975).
8. S. Mikkola and M. Valtonen, Mon. Not. R. Astron. Soc. **223**, 269 (1986).
9. J. J. Monaghan, Mon. Not. R. Astron. Soc. **176**, 63 (1976a).
10. J. J. Monaghan, Mon. Not. R. Astron. Soc. **177**, 583 (1976b).
11. P. E. Nash and J. J. Monaghan, Mon. Not. R. Astron. Soc. **184**, 119 (1978).
12. W. C. Saslaw, M. J. Valtonen, and S. J. Aarseth, Astrophys. J. **190**, 253 (1974).
13. E. M. Standish, Astron. Astrophys. **21**, 185 (1972).
14. V. Szebehely and K. Zare, Astron. Astrophys. **58**, 145 (1974).
15. M. Valtonen, *The Stability of the Solar System and of Small Stellar Systems,* Ed. by Y. Kozai (D. Reidel, Dordrecht, 1977), p. 211.
16. M. Valtonen, Vistas Astron. **32**, 23 (1988).
17. M. Valtonen and S. Mikkola, Annu. Rev. Astron. Astrophys. **29**, 9 (1991).

Translated by A. Dambis

Natural Superrotation of a Rarefied Planetary Atmosphere

P. A. Bespalov[1]* and   O. N. Savina[2]

[1]Institute of Applied Physics, Russian Academy of Sciences, ul. Ul'yanova 46, Nizhni Novgorod, 603600 Russia
[2]Nizhni Novgorod State Technical University, ul. Minina 24, Nizhni Novgorod, 603600 Russia

Received March 20, 2002; in final form, July 10, 2002

Abstract—We consider the kinetics of a rarefied rotating planetary atmosphere. The spatial distributions of the atmospheric-gas density and mean angular velocity were determined by analyzing the exact solution of the two-dimensional kinetic equation. We show that the angular velocity of the gas at some distance from the planet could be higher than that in the initial layer starting from which the atmosphere is rarefied. Our model calculations elucidate the superrotation mechanism under consideration. © 2003 MAIK "Nauka/Interperiodica".

Key words: *planets, Venus, Mars, Earth, atmospheres, kinetics, rotation, superrotation.*

INTRODUCTION

Experimental studies of atmospheric flows carried out for several planets have established the possibility of superrotation of their atmospheres. Thus, for example, analysis of satellite drag in the Earth's atmosphere revealed atmospheric superrotation at large heights. This superrotation is characterized by the ratio of the angular velocities of the atmosphere and the Earth. Following Allen (1973), we give experimental values of the superrotation at various heights above the Earth's surface:

Height, km	200	250	300	350	400
Superrotation	1.1	1.2	1.3	1.4	1.1

The atmosphere of Venus exhibits pronounced superrotation: the rotation period of its upper cloud cover is about four days (Izakov 2001), while the rotation period of the planet is about 247 Earth days (Izakov 2001).

Several possible superrotation mechanisms have been discussed in the literature. Hide (1984) associated superrotation with the nonuniform rotation of the planet due to its internal processes. The results obtained were used to explain processes in the atmospheres of Earth and Venus. Nonuniform atmospheric heating by the Sun as a superrotation source for the atmosphere of Venus was investigated by Dikii (1969), Dobrovolskis and Ingersoll (1980), Monin *et al.* (1987), and Izakov (2001). Kundt (1983) considered the spinup action of the Ampère force. Thus, several mechanisms responsible for atmospheric superrotation were proposed, but none of

them were universal. Indeed, Venus possesses no appreciable magnetic field at all, which makes it difficult to invoke the Ampère force to explain superrotation. Nonuniform solar heating of the giant planets seems not so important because they are far from the Sun and their rotation is rapid. In general, the universal superrotation mechanism has not yet been established.

Here, we consider the kinetics of a rarefied atmosphere replenished with particles injected from a spherical surface inside which collisions are significant. As we show below, peculiarities of the motion of a rarefied gas in the gravitational field of a slowly rotating planet can give rise to superrotation. It follows from the laws of motion that sufficiently fast particles can rise high and even recede to infinity. Because of the axial rotation of the planet, the particles whose velocity have the same direction as the rotational velocity of the planet will have a higher (in magnitude) initial velocity. Primarily these particles can recede appreciably from the planet to become its "satellites" due to weak collisions. Therefore, we have reason to expect that the mean angular velocity of the particles in the upper planetary atmosphere can exceed the angular velocity at its inner boundary. Let us now turn to a quantitative analysis of this problem based on the exact solution of the kinetic equation.

BASIC EQUATIONS

Consider the motion of a single particle for the Keplerian problem. In spherical coordinates, the components of the particle velocity **v** are defined by the kinematic relations

$$v_r = \frac{dr}{dt}, \quad v_\theta = r\frac{d\theta}{dt}, \quad v_\varphi = r\sin\theta\frac{d\varphi}{dt},$$

*E-mail: `peter@appl.sci-nnov.ru`

where φ is the azimuthal angle and the angle θ is measured from the rotation axis.

The Lagrangian L for this problem does not depend explicitly on time, $\partial L/\partial t = 0$. Therefore, it is the energy integral

$$\varepsilon = \frac{m}{2}\left(\dot{r}^2 + r^2\dot{\theta}^2 + r^2\sin^2\theta\dot{\varphi}^2\right) - g\frac{mr_0^2}{r}, \quad (1)$$

where m is the particle mass, r_0 is the planetary radius, r is the distance from the planetary center to the particle, and g is the free-fall acceleration on the planetary surface. Since $\partial L/\partial\varphi = 0$, the variable φ is cyclic. Consequently, there is another integral of motion that can be written as

$$M = mr^2\sin^2\theta\dot{\varphi}. \quad (2)$$

Thus, according to Eqs. (1) and (2), the energy ε and angular momentum M are conserved during the motion of a single particle. The particle is known to move in an elliptical orbit for $\varepsilon < 0$ and in a hyperbolic orbit for $\varepsilon > 0$ (see, e.g., Arnold 1979).

SOLVING THE COLLISIONLESS KINETIC EQUATION FOR THE TWO-DIMENSIONAL MODEL PROBLEM

Let us write the collisionless Boltzmann kinetic equation for the distribution function $f(t, \mathbf{r}, \mathbf{v})$ in spherical coordinates (Kogan 1967):

$$\frac{\partial f}{\partial t} + v_r\frac{\partial f}{\partial r} + \frac{v_\varphi}{r\sin\theta}\frac{\partial f}{\partial\varphi} + \frac{v_\theta}{r}\frac{\partial f}{\partial\theta} \quad (3)$$

$$+ \left(\frac{v_\varphi^2 + v_\theta^2}{r} - g\frac{r_0^2}{r^2}\right)\frac{\partial f}{\partial v_r}$$

$$- \left(\frac{v_\varphi v_\theta\cos\theta}{r\sin\theta} + \frac{v_\varphi v_r}{r}\right)\frac{\partial f}{\partial v_\varphi}$$

$$+ \left(\frac{v_\varphi^2\cos\theta}{r\sin\theta} - \frac{v_\theta v_r}{r}\right)\frac{\partial f}{\partial v_\theta} = 0.$$

We seek the solution of this equation by choosing an appropriate boundary condition. Assume that particles with a Maxwellian (in a comoving frame of reference) velocity distribution are injected from the planetary surface in the equatorial plane. To simplify our analysis, we restrict it to the two-dimensional problem by assuming that $\theta = \pi/2$ and $v_\theta = 0$. In an inertial frame of reference, this distribution is

$$f_+ = C\exp\left\{-\left(\frac{m}{2kT}\right)\right. \quad (4)$$

$$\left. \times\left[(v_\varphi - \omega_+ r_0)^2 + v_r^2\right]\right\}E(v_r),$$

where C is the normalization constant; T is the temperature that characterizes the thermal spread in azimuthal and radial velocities; k is the Boltzmann constant; ω_+ is the characteristic angular velocity for the particles escaping from the surface, which we choose below in such a way that the mean angular velocity near the surface is ω_0; and the factor with a unit function $E(v_r)$ ($E(\xi) = 1$, $\xi > 0$; $E(\xi) = 0$, $\xi < 0$) takes into account the fact that particles with upward-directed velocities are injected. In our case, the function $E(v_r)$ for particles with positive energies is also the energy integral.

According to Eqs. (1) and (2), for the particles moving in the equatorial plane,

$$\varepsilon = \frac{m}{2}(v_r^2 + v_\varphi^2) - g\frac{mr_0^2}{r}, \quad (5)$$

$$M = mrv_\varphi.$$

Relations (5) define the range of distances r in which the particle moves. The boundaries of this range correspond to the condition $v_r = 0$ and depend on ε and M. This circumstance should be taken into account when seeking a solution.

The sought-for distribution function must describe both escaping and returning particles. The energy of the downward-moving particles is negative ($\varepsilon < 0$); there are no particles with $\varepsilon > 0$ in the flow falling to the planet, because they go to infinity. According to the Liouville theorem for Hamiltonian systems, the distribution function $f(\mathbf{r}, \mathbf{v})$ that is the solution of Eq. (3) is an integral of motion. Therefore, a function of other integrals of motion is also the solution of Eq. (3). Thus, the expression for the sought-for distribution function can be written as

$$f = C\exp\left\{-\left(\frac{m}{2kT}\right)\left(\omega_+^2 r_0^2 + 2gr_0\right)\right\} \quad (6)$$

$$\times E\left(\frac{m}{2}(v_r^2 + v_\varphi^2) - g\frac{mr_0^2}{r} - \frac{mr^2v_\varphi^2}{2r_0^2} + mgr_0\right)$$

$$\times\left[E\left(-\frac{m}{2}(v_r^2 + v_\varphi^2) + g\frac{mr_0^2}{r}\right)\right.$$

$$\left. + E\left(\frac{m}{2}(v_r^2 + v_\varphi^2) - g\frac{mr_0^2}{r}\right)E(v_r)\right]$$

$$\times\exp\left\{-\left(\frac{m}{2kT}\right)\left(v_r^2 + v_\varphi^2 - 2\omega_+ rv_\varphi - 2g\frac{r_0^2}{r}\right)\right\}.$$

In expression (6), the factor $E(\varepsilon - (M^2/2mr_0^2) + mgr_0)$ makes it possible to selectively take into account the particles whose orbits reach the planetary surface. This corresponds to the choice of initial conditions when there are no particles (no satellites) in orbits that do not touch the planet. It can be verified that the distribution function (6) satisfies the boundary and initial conditions and the kinetic equation (3).

Given the distribution function, the density and angular velocity can be easily determined:

$$n(r, \omega_+) = \int\limits_{-\infty}^{+\infty} \int\limits_{-\infty}^{+\infty} f \, dv_\varphi \, dv_r, \qquad (7)$$

$$\omega(r, \omega_+) = \frac{1}{rn(r, \omega_+)} \int\limits_{-\infty}^{+\infty} \int\limits_{-\infty}^{+\infty} f v_\varphi \, dv_\varphi \, dv_r$$

$$= \frac{kT}{mr^2 n(r, \omega_+)} \frac{\partial n(r, \omega_+)}{\partial \omega_+} + \omega_+ \left(\frac{r_0}{r}\right)^2.$$

Let us first calculate the integral over v_φ in the first formula (7). To this end, we consider the integral $\Psi(r, v_r)$ with appropriate integration limits,

$$\Psi(r, v_r) \qquad (8)$$

$$= \int\limits_{v_{\varphi\min}(r,v_r)}^{v_{\varphi\max}(r,v_r)} \exp\left\{-\left(\frac{m}{2kT}\right)(v_\varphi - \omega_+ r)^2\right\} dv_\varphi.$$

In this integral, the integration limits $v_{\varphi\min}(r, v_r)$ and $v_{\varphi\max}(r, v_r)$ are defined by the unit functions in relation (6). Let us discuss the physical meaning of the range of integration in integral (8). Under the chosen boundary and zero initial conditions, particles are present only in the region hatched by inclined straight lines in the v_φ, v_r plane (see Fig. 1). Particles moving in elliptical orbits are located in the region with double hatching, while particles moving in hyperbolic orbits that go to infinity are located in the region with single inclined hatching. According to Eqs. (5) and (6), the line

$$\frac{\varepsilon}{mgr_0} = -1 + \frac{M^2}{2m^2 gr_0^3}$$

bounds the region of the particles whose orbits pass through the $r = r_0$ sphere. Particles moving in finite orbits that do not cross the planetary surface are located in the regions with horizontal hatching. In the absence of collisions, if there were no such particles according to the initial conditions, then they will not appear. The particles whose orbits start and end at infinity without crossing the sphere of radius r_0 are located in the regions with vertical hatching; these particles are disregarded in our calculations. Thus, we must take into account only the particles that are located in the region with inclined hatching. In the variables v_φ and v_r, this region (Fig. 1) is bounded by the circumference

$$v_r^2 + v_\varphi^2 = 2gr_0\left(\frac{r_0}{r}\right)$$
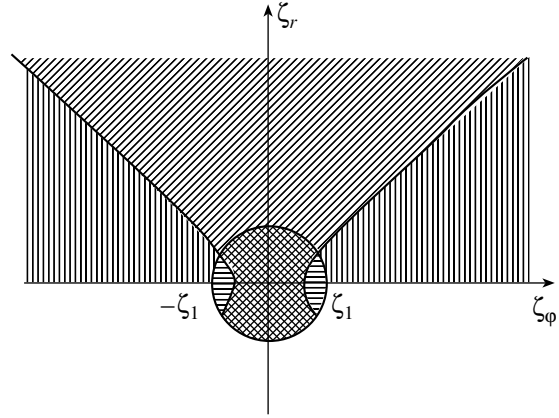

Fig. 1. The regions of velocity space ($\zeta_\varphi = v_\varphi/(2gr_0)^{1/2}$ and $\zeta_r = v_r/(2gr_0)^{1/2}$) that correspond to particles escaping from and returning to the planet (double inclined hatching); to particles escaping from and not returning to the planet (single inclined hatching); to satellites (horizontal hatching); and to particles arriving from and going back to infinity (vertical hatching). The radius of the circle is $\zeta_1 = (r_0/r - \zeta_r^2)^{1/2}$.

that corresponds to a zero total energy ε and by the hyperbola

$$v_r^2 - \left[\left(\frac{r}{r_0}\right)^2 - 1\right] v_\varphi^2 = -2gr_0\left(\frac{r_0}{r}\right)\left(\frac{r}{r_0} - 1\right)$$

that corresponds to the contact of the orbits with the $r = r_0$ sphere.

Let us write out integral (8). Bearing in mind the integration over the region with inclined hatching in Fig. 1, we can write the function $\Psi(r, v_r)$ as

$$\Psi(r, v_r) = E(v_r - v_{r1})E(v_{r2} - v_r)\Psi_1(r, v_r) \qquad (9)$$
$$+ E(v_r - v_{r2})\Psi_2(r, v_r).$$

Here,

$$v_{r1} = -r_0\left(\frac{2g}{r}\right)^{1/2},$$

$$v_{r2} = -\frac{r_0}{r}\left[2gr_0\left(\frac{r}{r_0} - 1\right)\right]^{1/2},$$

$$\Psi_{1,2}(r, v_r, \omega_+) = \left(\frac{\pi kT}{m}\right)^{1/2}$$

$$\times \left\{ \mathrm{erf}\left[\left(\frac{m}{2kT}\right)^{1/2}(v_{1,2} + \omega_+ r)\right] \right.$$

$$\left. + \mathrm{erf}\left[\left(\frac{m}{2kT}\right)^{1/2}(v_{1,2} - \omega_+ r)\right] \right\},$$

where

$$\mathrm{erf}(x) = \frac{2}{\sqrt{\pi}} \int_0^x \exp(-\xi^2) d\xi$$

is the error integral (*Handbook...* 1964),

$$v_1 = \left[2gr_0\left(\frac{r_0}{r}\right) - v_r^2\right]^{1/2},$$

$$v_2 = \left[v_r^2 + 2gr_0\left(\frac{r_0}{r}\right)\left(\frac{r}{r_0} - 1\right)\right]^{1/2}$$

$$\times \left[\left(\frac{r}{r_0}\right)^2 - 1\right]^{-1/2}.$$

Using formula (9), the radial density distribution (7) can be written as

$$n(r,\omega_+) = C\exp\left\{\frac{m}{2kT}\left[\omega_+^2(r^2 - r_0^2)\right.\right. \qquad (10)$$

$$\left.\left. - 2gr_0\left(1 - \frac{r_0}{r}\right)\right]\right\}\left\{\int_{v_{r1}}^{v_{r2}}\exp\left(-\frac{mv_r^2}{2kT}\right)\Psi_1 dv_r\right.$$

$$\left. + \int_{v_{r2}}^{\infty}\exp\left(-\frac{mv_r^2}{2kT}\right)\Psi_2 dv_r\right\}.$$

To analyze expression (10), it is convenient to change to dimensionless variables. It is clear from general considerations that the solution of the problem of rarefied-gas kinetics depends on several dimensionless parameters. These primarily include the scale height H reduced to the planetary radius

$$h = H/r_0.$$

It is convenient to represent the angular velocity of the planet ω_0, the mean angular velocity of the upward moving particles ω_+ at $r = r_0$, and the mean local angular velocity ω as

$$\Omega_0 = \frac{\omega_0}{\omega_b}, \quad \Omega_+ = \frac{\omega_+}{\omega_b}, \quad \Omega = \frac{\omega}{\omega_b}.$$

Here, ω_b is the ballistic angular velocity at $r = r_0$, which can be determined from the relation $m\omega_b^2 r_0 = mg$: $\omega_b = (g/r_0)^{1/2}$.

The reduced distance to the planetary center R and the dimensionless radial and azimuthal particle velocities, ζ_r and ζ_φ, can be written as

$$R = \frac{r}{r_0}, \quad \zeta_r = \frac{v_r}{(2gr_0)^{1/2}}, \quad \zeta_\varphi = \frac{v_\varphi}{(2gr_0)^{1/2}}.$$

Let us now analyze the expression for the radial density distribution (10) by writing it as a function of the dimensionless variables:

$$n(R,\Omega_+) = Cgr_0(\pi h)^{1/2} \qquad (11)$$

$$\times \exp\left\{\frac{1 - R}{hR} + \frac{\Omega_+^2(R^2 - 1)}{2h}\right\}$$

$$\times \left[\int_{-R^{-1/2}}^{-R^{-1}(R-1)^{1/2}}\exp(-\zeta_r^2/h)\Phi_1 d\zeta_r\right.$$

$$\left. + \int_{-R^{-1}(R-1)^{1/2}}^{\infty}\exp(-\zeta_r^2/h)\Phi_2 d\zeta_r\right],$$

where we introduced the functions

$$\Phi_{1,2}(R,\zeta_r,\Omega_+) = \left\{\mathrm{erf}\left[\frac{1}{h^{1/2}}\left(\zeta_{1,2} + \frac{\Omega_+ R}{\sqrt{2}}\right)\right]\right.$$

$$\left. + \mathrm{erf}\left[\frac{1}{h^{1/2}}\left(\zeta_{1,2} - \frac{\Omega_+ R}{\sqrt{2}}\right)\right]\right\}.$$

Here,

$$\zeta_1 = \left(\frac{1}{R} - \zeta_r^2\right)^{1/2},$$

$$\zeta_2 = \left[\zeta_r^2 + \frac{1}{R}(R - 1)\right]^{1/2}(R^2 - 1)^{-1/2}.$$

In turn, according to the second formula (7), the angular velocity

$$\Omega = \frac{h}{R^2}\left(\frac{1}{n}\frac{\partial n}{\partial\Omega_+}\right) + \frac{\Omega_+}{R^2} = \Omega_+ - \frac{1}{R}\left(\frac{8h}{\pi}\right)^{1/2}\exp\left(-\frac{\Omega_+^2 R^2}{2h}\right) \qquad (12)$$

$$\times \frac{\left[\int_{-R^{-1/2}}^{-R^{-1}(R-1)^{1/2}}\exp(-\zeta_r^2/h)\Psi_1 d\zeta_r + \int_{-R^{-1}(R-1)^{1/2}}^{\infty}\exp(-\zeta_r^2/h)\Psi_2 d\zeta_r\right]}{\left[\int_{-R^{-1/2}}^{-R^{-1}(R-1)^{1/2}}\exp(-\zeta_r^2/h)\Phi_1 d\zeta_r + \int_{-R^{-1}(R-1)^{1/2}}^{\infty}\exp(-\zeta_r^2/h)\Phi_2 d\zeta_r\right]},$$

where

$$\Psi_{1,2} = \exp\left(-\frac{\zeta_{1,2}^2}{h}\right)\sinh\left(\frac{\sqrt{2}\zeta_{1,2}\Omega_+ R}{h}\right).$$

Solutions (11) and (12) depend on two arbitrary constants, Ω_+ and C, which can be determined from the following considerations. Recall that ω_+ is the mean angular velocity of the particles injected from the level below which the gas cannot be assumed to be rarefied. Under this assumption, we can argue that

the mean angular velocity $\omega(r_0)$ of the atmospheric gas at the chosen boundary calculated using formula (7) must be equal to the angular velocity of the planet, $\omega(R = 1) = \omega_0$. In dimensionless variables, this condition is $\Omega(R = 1) = \Omega_0$ and, according to (12), it is an equation to determine Ω_+. In general form, this equation can be solved numerically. However, if $\Omega_+ \ll 1$, which corresponds to a low angular velocity of the atmosphere compared to the ballistic particle velocity near the planetary surface, then this constant can be determined analytically to give

$$\Omega_+ = \Omega$$

$$\times \left\{ 1 - \frac{2}{\pi h} \frac{\left[\int_{-R^{-1/2}}^{-R^{-1}(R-1)^{1/2}} \zeta_1 \exp\left(-\frac{\zeta_r^2}{h} - \frac{\zeta_1^2}{2} \right) d\zeta_r + \int_{-R^{-1}(R-1)^{1/2}}^{\infty} \exp\left(-\frac{\zeta_r^2}{h} - \frac{\zeta_2^2}{2} \right) d\zeta_r \right]}{\left[\int_{-R^{-1/2}}^{-R^{-1}(R-1)^{1/2}} \exp\left(-\frac{\zeta_r^2}{h} \right) \mathrm{erf}\left(\frac{\zeta_1}{h^{1/2}} \right) d\zeta_r + \int_{-R^{-1}(R-1)^{1/2}}^{\infty} \exp\left(-\frac{\zeta_r^2}{h} \right) \mathrm{erf}\left(\frac{\zeta_2}{h^{1/2}} \right) d\zeta_r \right]} \right\}^{-1} .$$

If Ω_+ is known from the condition $n(R = 1) = n_0$, then the second constant C can be easily calculated by using relation (11). Having determined these constants, we unambiguously find the solution to our problem.

SOLVING THE KINETIC EQUATION WITH WEAK COLLISIONS

In an actual rarefied atmosphere, there are at least weak collisions that realize Brownian motion in velocity space. For the light helium- and hydrogen-type molecules concerned, which are well represented in the upper rarefied atmosphere, Brownian motion is related to the natural deviation of the gravitational field from exact axial symmetry. This deviation causes the angular-momentum invariance to break down.

Assume that the effective scattering centers are fixed in the laboratory frame of reference. The energy ε

Fig. 2. The space of integrals of motion: the denser the hatching, the larger the distribution function.

is then conserved during collisions. The small random variations in angular momentum M can be taken into account by substituting the collision term in the Fokker–Planck form (Javier *et al.* 1999) into the right-hand side of Eq. (3):

$$\mathrm{St}f = v_r \frac{\partial}{\partial M}\left(\frac{D(\varphi, r, M, \varepsilon)}{v_r} \frac{\partial f}{\partial M} \right), \qquad (13)$$

where D is a positive diffusion coefficient and v_r ensures that the total number of particles is conserved. To be more precise, this factor is related to the recalculation of variables in accordance with the formulas

$$dM d\varepsilon = m^2 r |v_r| dv_\varphi dv_r.$$

The significance of weak collisions is easiest to explain on the plane shown in Fig. 2. Transit particles (the region with inclined hatching) are located in the collision zone for a finite time. At a low diffusion coefficient, these give only a small correction to the distribution function. The situation in the zone of particles with finite captured satellite-type orbits (the region with horizontal hatching) is different. These particles experience collisions for a long time. Over a long period, the distribution function levels off in angular momentum M up to $\partial f/\partial M = 0$ through collisions (13). At the $\varepsilon = 0$ boundary, the distribution function is continuous. Therefore, the steady-state distribution function (6) can be extended into the zone of satellites:

$$f^\pm = C \exp\left\{ -\left(\frac{m}{2kT} \right) \left(\omega_+^2 r_0^2 + 2gr_0 \right) \right\} \quad (14)$$

$$\times \exp\left\{ \frac{\pm \omega_+ m r_0 (2gr_0)^{1/2}[(\varepsilon/mgr_0) + 1]^{1/2} - \varepsilon}{kT} \right\},$$

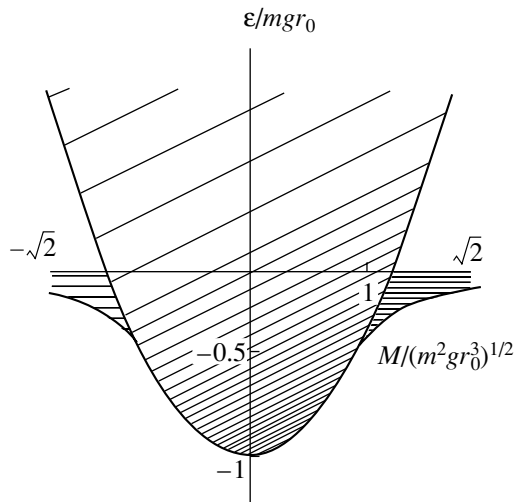where the "+" and "−" signs correspond, respectively, to particles with the same sense of rotation as

Fig. 3. The radial density distribution in the atmospheres of Venus (V), Earth (E), and Mars (M).
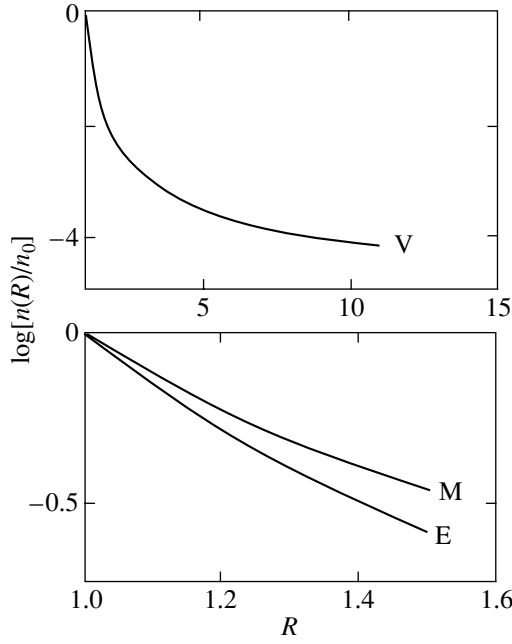

Fig. 4. The radial angular-velocity distribution in the atmospheres of Venus (V), Earth (E), and Mars (M).

the planet and to particles rotating in the opposite sense.

Given the contribution of the trapped particles, the expressions for the density and angular velocity change. We have the following expressions in place of formulas (11) and (12):

$$n_{St}(R, \Omega_+) = n(R, \Omega_+) \qquad (15)$$

$$+ \int_{-\zeta_3}^{\zeta_3} \left(\int_{-\zeta_1}^{-\zeta_2} F^- d\zeta_\varphi \right) d\zeta_r + \int_{-\zeta_3}^{\zeta_3} \left(\int_{\zeta_2}^{\zeta_1} F^+ d\zeta_\varphi \right) d\zeta_r.$$

Here,

$$F^{\pm} = C2gr_0 \exp \left\{ -\frac{(2 + \Omega_+^2)}{2h} \pm \sqrt{2} \frac{\Omega_+}{h} \right.$$

$$\times \left(\zeta_r^2 + \zeta_\varphi^2 + 1 - \frac{1}{R} \right)^{1/2} - \frac{1}{h} \left(\zeta_r^2 + \zeta_\varphi^2 - \frac{1}{R} \right) \right\},$$

$$\zeta_1 = \left(\frac{1}{R} - \zeta_r^2 \right)^{1/2},$$

$$\zeta_2 = \left[\zeta_r^2 + \frac{1}{R}(R - 1) \right]^{1/2} (R^2 - 1)^{-1/2},$$

$$\zeta_3 = \frac{(R - 1)^{1/2}}{R}.$$

In turn, according to the second formula (7), the angular velocity

$$\Omega_{St}(R, \Omega_+) = \frac{n(R, \Omega_+)}{n_{St}(R, \Omega_+)} \Omega(R, \Omega_+) \qquad (16)$$
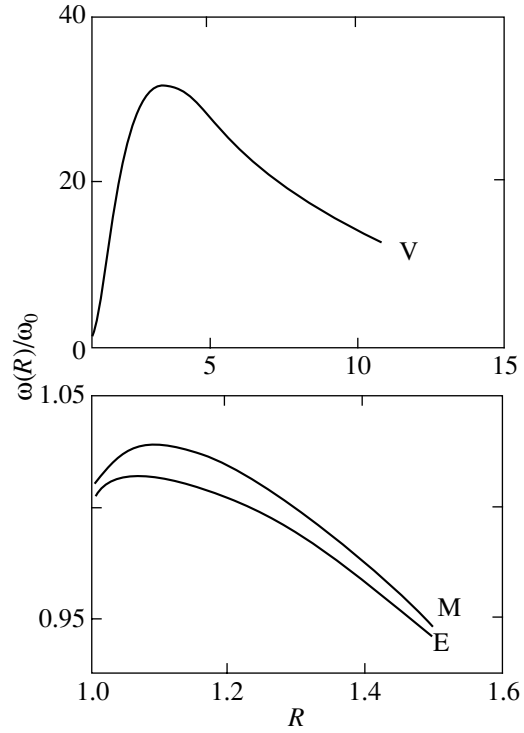
$$+ \frac{\sqrt{2}}{R n_{St}(R, \Omega_+)} \left\{ - \int_{-\zeta_3}^{\zeta_3} \left(\int_{-\zeta_1}^{-\zeta_2} F^- \zeta_\varphi d\zeta_\varphi \right) d\zeta_z \right.$$

$$\left. + \int_{-\zeta_3}^{\zeta_3} \left(\int_{\zeta_2}^{\zeta_1} F^+ \zeta_\varphi d\zeta_\varphi \right) d\zeta_z \right\}.$$

Examples of our calculations performed using formulas (15) and (16) are shown in Figs. 3 and 4.

DISCUSSION OF SUPERROTATION FOR A RAREFIED ATMOSPHERE

Extensive experimental data on flows in planetary atmospheres have been accumulated to date (Allen 1973; Zasova *et al.* 2000). According to current theoretical views, there are several superrotation mechanisms: nonuniform atmospheric heating by the Sun (Dikii 1969; Dobrovolskis and Ingersoll 1980; Monin *et al.* 1987; and Izakov 2001), nonuniform rotation of the planet due to its internal processes (Hide 1984), and the action of the Ampère force on the current system (Kundt 1983).

Here, we restricted our analysis to the superrotation of a rarefied atmosphere whose properties are described by kinetic equations. For our case in a

Table

Planet	h_0	Ω_0	R_*	h
Venus	4.95×10^{-4}	2.47×10^{-4}	1.93×10^2	0.099
Earth	1.25×10^{-3}	0.059	6.63	0.25
Mars	3.24×10^{-3}	0.068	6.03	0.324

zero-order approximation, we assumed that a comparatively dense atmosphere rigidly rotates with the angular velocity of the planet because of viscosity. Our calculations yield the angular velocity of the gas in the exosphere, which can serve as an upper boundary condition for the lower hydrodynamic flow of the atmosphere.

Let us summarize the information on physical conditions in the atmospheres of slowly rotating planets whose angular velocities are much lower than the ballistic angular velocity on the surface that is required for our estimates. We present the reduced scale heights h_0 near the planetary surfaces, the angular velocities of the planets Ω_0, and the geostationary orbital radii R_* in tabular form using data from Allen (1973).

All of the planets under consideration rotate slowly, because $\Omega_0 \ll 1$ for them. The last column in the table deserves a special discussion. It gives the scale heights of the atmospheres where they are rarefied and where our results are valid. In estimating these quantities, we took into account the fact that at large heights, where the gas is highly rarefied, the temperature differs from the surface temperature and light (helium and hydrogen) particles dominate. Therefore, h are many times larger than h_0 near the planetary surface. It would be more appropriate to take an elevated level as the lower boundary of a rarefied atmosphere, but this does not change our qualitative conclusions.

For the tabulated data, we determined the radial density and angular-velocity distributions using formulas (15) and (16). Superrotation of the type under consideration is most pronounced for Venus, where $\omega_{max}/\omega_0 \approx 30$. For the Earth, where $\omega_{max}/\omega_0 \approx 1.02$, superrotation is indistinct. Superrotation shows up more clearly in the atmosphere of Mars, where $\omega_{max}/\omega_0 \approx 1.03$. Note that our conclusions regarding the exospheric superrotation of Venus should be treated with care. The point is that the theory of thermal tides (Monin *et al.* 1987) plays an important role in understanding the effect under consideration in a dense atmosphere. Allowance for the mutual influence of flows in dense and rarefied atmospheres requires further studies.

Thus, arbitrarily weak collisions with light (hydrogen and helium) particles along with effective "collisions" with gravitational-field nonuniformities in a steady state cause the distribution function to level off in the zone of satellites. This leveling leads to different levels for particles with the same sense of rotation as the planet and those rotating in the opposite sense. Satellites are fast particles for slowly rotating planets. The above superrotation can be explained by the fact that the ballistic angular velocity on the surface is higher than the angular velocity of the planet. This effect vanishes outside the geostationary orbit that satisfies the condition

$$R_* = \left(\frac{g}{\omega_0^2 r_0} \right)^{1/3} = \frac{1}{\Omega_0^{2/3}}.$$

Therefore, for this superrotation mechanism to take place, the planetary rotation must also be sufficiently slow in the sense that $1 \ll R_*$.

The three-dimensional problem of the kinetics of a rarefied atmosphere corresponds to an actual situation. It is clear from symmetry that in three-dimensional calculations, no angular velocity will appear in the θ direction and that the angular velocity in the φ direction will depend not only on radius but also on latitude. This is because particles arrive at the point with the chosen radius and latitude from the surface in flat orbits that lie in all the planes passing through the radius vector. Therefore, there is an effective planetary radius of its own at each latitude. Our calculations yield estimates of the actual processes in the equatorial plane.

Atmospheric superrotation can also affect the electrodynamics of the ionosphere. The point is that at heights where the density of charged particles is much lower than the density of neutral particles, charged particles can be treated as a passive scalar entrained by collisions with neutral particles (Gershman 1974). This effect produces a conductive plasma sheet that does not rotate rigidly with the planet. This type of motion keeps the planetary electric generator, which produces a kind of a current system in the ionosphere and atmosphere, running (Bespalov and Chugunov 1996).

CONCLUSIONS

We have shown that one of the superrotation mechanisms for rarefied planetary atmospheres is the separation of particles: some of them fly away from the planet, while others become its satellites. Based on the proposed mechanism, we estimated the superrotation for the exospheres of Venus, Earth, and Mars.

Our main results are as follows.

(1) We found an exact solution of the boundary-value problem for the two-dimensional collisionless Boltzmann equation that includes particles with elliptical and hyperbolic orbits.

(2) We obtained and analyzed the solution of the kinetic equation with weak elastic collisions.

(3) We determined the spatial distributions of the atmospheric-gas density and mean angular velocity and established the possibility of exospheric superrotation.

In conclusion, it should be emphasized that the separation of particles with weak collisions is a universal, although, probably, not the only superrotation mechanism for an upper rarefied slowly rotating atmosphere.

ACKNOWLEDGMENTS

REFERENCES

1. C. W. Allen, *Astrophysical Quantities* (Athlone Press, London, 1973; Mir, Moscow, 1977).
2. V. I. Arnold, *Mathematical Methods of Classical Mechanics* (Nauka, Moscow, 1979; Springer-Verlag, New York, 1989).
3. P. A. Bespalov and Yu. V. Chugunov, J. Atmos. Terr. Phys. **58**, 601 (1996).
4. L. A. Dikii, *Theory of Oscillations of the Earth's Atmosphere* (Gidrometeoizdat, Leningrad, 1969).
5. A. R. Dobrovolskis and A. P. Ingersoll, Icarus **41**, 1 (1980).
6. B. N. Gershman, *Dynamics of Ionospheric Plasma* (Nauka, Moscow, 1974).
7. *Handbook of Mathematical Functions,* Ed. by M. Abramowitz and I. A. Stegun (National Bureau of Standards, Washington, 1964; Nauka, Moscow, 1979).
8. R. Hide, Philos. Trans. R. Soc. London, Ser. A **313**, 107 (1984).
9. M. N. Izakov, Astron. Vestn. **35**, 275 (2001).
10. B. J. Javier, M. J. Ruiz-Montero, R. R. Garciacutea, *et al.*, Phys. Rev. E **60**, 7174 (1999).
11. M. N. Kogan, *Dynamics of Rarefied Gas* (Nauka, Moscow, 1967).
12. W. Kundt, Planet. Space Sci. **31**, 1339 (1983).
13. A. S. Monin, A. S. Shafrai, and O. V. Chalikov, Dokl. Akad. Nauk SSSR **295**, 828 (1987).
14. L. V. Zasova, V. M. Linkin, and I. V. Khatuntsev, Kosm. Issled. **38**, 54 (2000).

Translated by V. Astakhov

A Model for the Tail Region of the Heliospheric Interface

V. V. Izmodenov[1*] and D. B. Alexashov[2**]

[1]*Moscow State University, Vorob'evy gory, Moscow, 119992 Russia*
[2]*Institute for Problems in Mechanics, Russian Academy of Sciences,*
pr. Vernadskogo 101, Moscow, 119526 Russia
Received July 8, 2002

Abstract—The physical processes in the tail of the region where the solar wind interacts with a partially ionized local interstellar medium are investigated in terms of a self-consistent kinetic–gas-dynamical model. Resonant charge exchange between hydrogen atoms and plasma protons is shown to cause the contact discontinuity to disappear far from the Sun. The solar wind plasma cools down and, as a result, the parameters of the plasma and hydrogen atoms approach the corresponding parameters of the unperturbed interstellar medium at large heliocentric distances. © *2003 MAIK "Nauka/Interperiodica"*.

Key words: *solar wind, heliosphere, interstellar medium.*

INTRODUCTION

The Sun and the Solar System are known to move in a partly ionized local interstellar medium (LISM) (Lallement 1996). Direct Ulysses measurements of interstellar helium atoms (Witte *et al.* 1996) yielded the translational velocity of the Sun relative to the LISM, ≈ 25 km s^{-1}, and the LISM temperature, ≈ 6000 K. Only these two LISM parameters (velocity and temperature) can be satisfactorily determined in the solar neighborhood. Other interstellar parameters, such as the degree of ionization, the densities of the neutral and charged components, and the magnitude and direction of the interstellar magnetic field, can be determined only indirectly, by theoretically interpreting various space experiments. Indirect measurements include the backscattered solar Lyman α radiation experiments onboard the SOHO, Voyager, and Pioneer spacecraft; pickup-ion measurements onboard the Ulysses and ACE spacecraft; Voyager solar wind measurements at large heliocentric distances; observations of Lyman α absorption toward nearby stars; and flux measurements of energetic neutral atoms (ENA). An adequate theoretical model for the solar wind interaction with the LISM is required to properly interpret these measurements. The concept of solar wind interaction with LISM plasma was suggested in the pioneering paper by Baranov *et al.* (1970). It has been developed for the last 30 years by several research groups [see, e.g., Izmodenov (2000, 2002) for a review].

The structure of the solar wind–LISM interaction region is shown in Fig. 1. The contact discontinuity, which is also called the heliopause (HP), separates the solar wind from the interstellar plasma. The heliopause may be treated as an obstacle both to the supersonic (with a Mach number of about 10) solar wind and to the supersonic (with a Mach number of about 2) interstellar wind. Supersonic flow around an obstacle is known to be accompanied by shock formation. The supersonic solar wind passes through the termination shock (TS) to become subsonic. After the passage of the bow shock (BS), the local interstellar gas becomes subsonic. Below, the solar wind–LISM interaction region composed of the HP, TS, and BS is called the heliospheric interface for short.

Note that when the effect of interstellar atoms is disregarded, the qualitative flow pattern in the tail region is more complex. The solar wind flow is subsonic in the nose of the region between the termination shock and the heliopause. The flow then passes through the sonic line (Baranov and Malama 1993) to become supersonic. As a result, a complex gas-dynamical structure with a Mach disk (MD), a tangential discontinuity (TD), and a reflected shock (RS) is formed in the tail region (Fig. 1a).

The neutral interstellar component, which consists mostly of hydrogen atoms, interacts with the plasma component through charge exchange and strongly affects the locations of the discontinuity surfaces and the heliospheric interface structure. The main difficulty in modeling the heliospheric interface is that the mean free path of neutral atoms is comparable to the characteristic size of the heliosphere.

[*]E-mail: `izmod@ipmnet.ru;http://delta.ipmnet.ru/~izmod/`
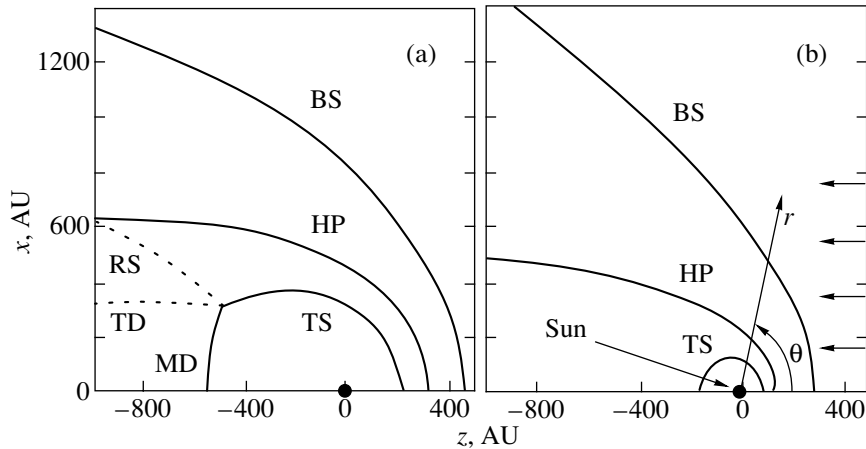[**]E-mail: `alexash@ipmnet.ru`

Fig. 1. The structure of the heliospheric interface: HP is the heliopause, TS is the heliospheric termination shock, BS is the bow shock, MD is the Mach disk, TD is the tangential discontinuity, and RS is the reflected shock. The left (a) and right (b) panels correspond to the calculations without interstellar hydrogen atoms and to the self-consistent solution with interstellar hydrogen atoms, respectively.

Therefore, a kinetic equation must be solved to describe the motion of the neutrals. A self-consistent two-component (plasma and hydrogen atoms) model of the heliospheric interface was proposed by Baranov *et al.* (1991) and realized by Baranov and Malama (1993). The latter authors also performed the first numerical simulations of the heliospheric tail. Figure 1 shows the locations of the discontinuity surfaces with and without an allowance for the effect of interstellar hydrogen atoms. The effect of atoms causes the discontinuity surfaces to approach the Sun. In the tail region, the flow structure changes qualitatively. The termination shock becomes more spherical and the Mach disk (MD), the reflected shock (RS), and the tangential discontinuity (TD) disappear (Fig. 1).

In particular, the model of the heliospheric interface allows us to answer the following two fundamental questions: (1) Where is the boundary of the Solar System? (2) How far does the influence of the Solar System on the surrounding interstellar medium extend?

Answering the first question requires defining the boundary of the Solar System. The heliopause, the surface that separates the solar wind from interstellar plasma, can be assumed to be the natural boundary of the Solar System. Note that the influence of the Solar System on the interstellar medium extends much farther than that of the heliopause. The secondary hydrogen atoms produced by charge exchange between interstellar atoms and solar wind protons play a significant role in this influence. The mutual effects of the charge and neutral components in the heliospheric interface were studied in detail by Baranov and Malama (1993, 1995, 1996), Baranov *et al.* (1998), and Izmodenov *et al.* (1999, 2000, 2001).

However, these authors focused mainly on the nose of the heliospheric interface. At the same time, studying the heliospheric tail region is also of considerable interest. For the heliospheric tail, the definition of the heliopause as the Solar System boundary is generally incorrect. Indeed, as can be seen from the calculations based on the Baranov−Malama model, the heliopause is not a closed surface and, hence, the solar wind region occupies unbounded space.

Here, our goal is to study the structure of the tail region of the heliospheric interface. We focus on the charge exchange processes.

THE MODEL

To investigate the effect of charge exchange on the structure of the heliospheric tail, we used the kinetic−gas-dynamical model by Baranov and Malama (1993). In this model, the solar wind at the Earth's orbit was assumed to be steady and spherically symmetric. The interstellar onflow was assumed to be uniform and plane-parallel. Under these conditions, the flow in the interaction region is steady and axisymmetric.

To describe the charged component (electrons and protons), we solved the hydrodynamic Euler equations with the source terms that took into account the effect of neutral atoms. The motion of interstellar atoms in the heliospheric interface was determined by solving the kinetic equation

$$\mathbf{w}_H \cdot \frac{\partial f_H(\mathbf{r}, \mathbf{w}_H)}{\partial \mathbf{r}} + \frac{\mathbf{F}}{m_H} \cdot \frac{\partial f_H(\mathbf{r}, \mathbf{w}_H)}{\partial \mathbf{w}_H} \quad (1)$$

$$= -f_H(\mathbf{r}, \mathbf{w}_H) \int |\mathbf{w}_H - \mathbf{w}_p| \sigma_{ex}^{HP} f_p(\mathbf{r}, \mathbf{w}_p) d\mathbf{w}_p$$

$$+ f_p(\mathbf{r}, \mathbf{w}_H) \int |\mathbf{w}_H^* - \mathbf{w}_H| \sigma_{\mathrm{ex}}^{\mathrm{HP}} f_H(\mathbf{r}, \mathbf{w}_H^*) d\mathbf{w}_H^*$$

$$- (\beta_i + \beta_{\mathrm{impact}}) f_H(\mathbf{r}, \mathbf{w}_H).$$

Here, $f_H(\mathbf{r}, \mathbf{w}_H)$ is the hydrogen atom velocity distribution function; $f_p(\mathbf{r}, \mathbf{w}_p)$ is the local Maxwellian proton velocity distribution function; $\mathbf{w}_p$ and $\mathbf{w}_H$ are the individual velocities of the protons and hydrogen atoms, respectively; $\sigma_{\mathrm{ex}}^{\mathrm{HP}}$ is the cross section for charge exchange between hydrogen atoms and protons; β_i is the photoionization rate; m_H is the mass of a hydrogen atom; β_{impact} is the electron impact ionization rate; and $\mathbf{F}$ is the sum of the solar gravitational force and the radiation pressure force.

The charged and neutral components interact mainly through charge exchange, $H + H^+ \to H^+ + H$. Nevertheless, photoionization and electron impact ionization are also included in Eq. (1). The interaction between charged and neutral particles results in the exchange of mass, momentum, and energy between the components. The source term $Q = (q_1, q_{2,z}, q_{2,r}, q_3)^T$ is on the right-hand sides of the Euler equations for the charged component, where q_1, $\vec{q_2} = (q_{2,z}, q_{2,r})^T$, and q_3 are the mass, momentum, and energy sources, respectively. The source terms are the integrals of the distribution function f_H:

$$q_1 = n_H(\beta_i + \beta_{\mathrm{impact}}), \quad n_H = \int f_H(\mathbf{w}_H) d\mathbf{w}_H,$$

$$q_2 = \int (\beta_i + \beta_{\mathrm{impact}}) \mathbf{w}_H f_H(\mathbf{w}_H) d\mathbf{w}_H \qquad (2)$$

$$+ \iint u \sigma_{\mathrm{ex}}^{\mathrm{HP}}(u)(\mathbf{w}_H - \mathbf{w}_p) f_H(\mathbf{w}_H) f_p(\mathbf{w}_p) d\mathbf{w}_H d\mathbf{w}_p,$$

$$q_3 = \int (\beta_i + \beta_{\mathrm{impact}}) \frac{\mathbf{w}_H^2}{2} f_H(\mathbf{w}_H) d\mathbf{w}_H \qquad (3)$$

$$+ \frac{1}{2} \iint u \sigma_{\mathrm{ex}}^{\mathrm{HP}}(u)(\mathbf{w}_H^2 - \mathbf{w}_p^2) f_H(\mathbf{w}_H) f_p(\mathbf{w}_p) d\mathbf{w}_H d\mathbf{w}_p.$$

Here, $u = |\mathbf{w}_H - \mathbf{w}_p|$ is the relative atom–proton velocity.

As the boundary conditions, we assumed that the velocity of the unperturbed local interstellar flow was $V_\infty = 25$ km s^{-1} and that the LISM hydrogen-atom and proton densities were 0.2 and 0.07 cm^{-3}, respectively. The LISM temperature was taken to be 6000 K. The solar wind velocity, density, and Mach number at the Earth's orbit were taken to be 450 km s^{-1}, 7 cm^{-3} and 10, respectively. The hydrogen-atom velocity distribution function in the unperturbed LISM was assumed to be Maxwellian.

The Euler equations with the source term Q were solved simultaneously with the kinetic equation for hydrogen atoms. To obtain a self-consistent solution, we used an iterative method. The kinetic equation was solved by the Monte-Carlo method with trajectory splitting. In contrast to the previous studies based on the Baranov–Malama model, we numerically computed the solar wind interaction with the LISM with various sizes of the tail region. In some cases, the size of the computational region reached 50 000 AU along the symmetry axis and 5000 AU perpendicular to the symmetry axis. To achieve the convergence of the iterations, we used computational grids with various resolutions. The dependence of the numerical solution on outer boundary conditions was estimated by varying the extent of the tail region.

QUALITATIVE ANALYSIS

Here, we consider the effect of charge exchange $(H + H^+ \to H^+ + H)$ on the plasma flow in the tail region of the heliospheric interface. The supersonic solar wind passes through the heliospheric termination shock, where its kinetic energy transforms into thermal energy. If the heliopause in the tail region is assumed to be parallel to the direction of the interstellar onflow (as follows from our numerical simulations), then the solar wind may be considered as a flow in a nozzle with a constant cross section. Our computations for the boundary conditions corresponding to the model described above show that in the case without hydrogen atoms, the solar wind pressure downstream the termination shock in the tail region is severalfold lower than the interstellar pressure. Under these conditions, the solar wind flow must decelerate, reaching a minimum velocity at infinity. As a result, the minimum velocity is determined only by the solar wind parameters downstream the termination shock and by the interstellar pressure; it depends neither on the LISM density nor on the relative Sun–LISM velocity. Thus, in the case without atoms, a solution in which the solar wind (and, hence, the Solar System) extends to infinity into the heliospheric tail is possible in terms of the hydrodynamic equations. Such qualitative reasoning also remains valid when the heliopause expands or contracts, because the solar wind flow may then be considered as a flow in an expanding or contracting nozzle.

A qualitatively different situation arises when the effect of interstellar hydrogen atoms is taken into account. Our computations show that in this case, the solar wind pressure downstream the termination shock is higher than the interstellar pressure. The solar wind should then be accelerated by the pressure gradient. However, interstellar atoms play a significant role here. They affect the solar wind flow through charge exchange: having mean free paths of the order of the size of the heliospheric interface,
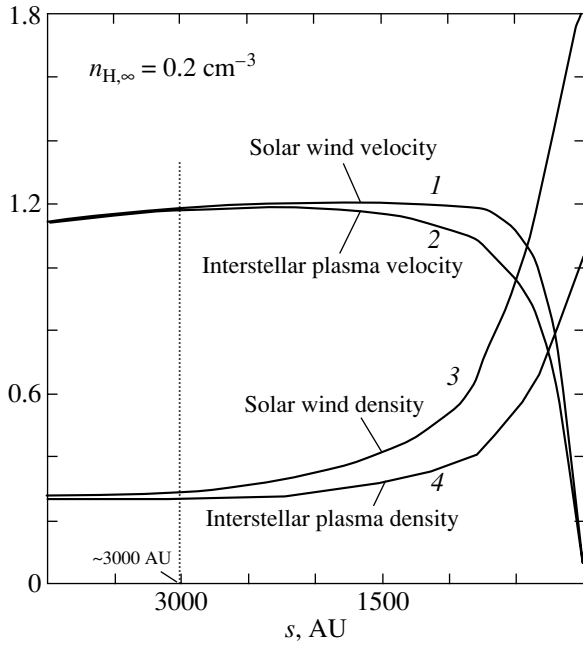
Fig. 2. The distributions of plasma velocity (curves *1* and *2*) and density (curves *3* and *4*) along the contact surface. Curves *2* and *4* correspond to the interstellar medium; curves *1* and *3* correspond to the solar wind. The velocities and densities are normalized to their interstellar values; *s* is the heliocentric distance along the contact surface.
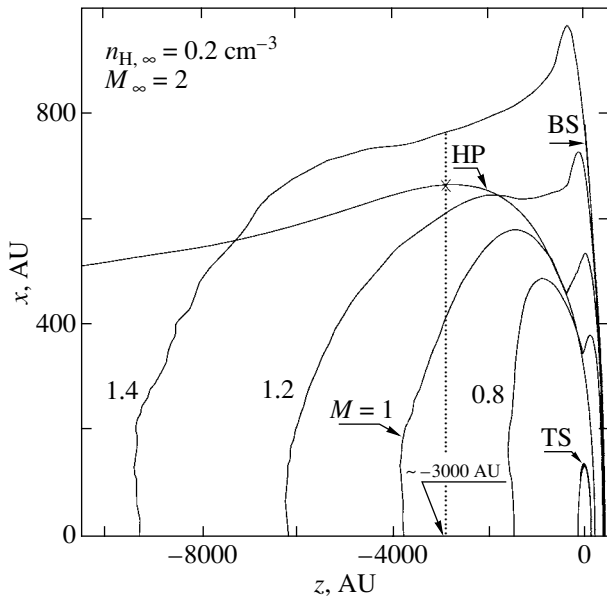

Fig. 3. Isolines of the gas-dynamical Mach number (M). The solar wind flow is supersonic at distances larger than 4000 AU. The Mach number approaches its value in the unperturbed LISM with increasing heliocentric distance.
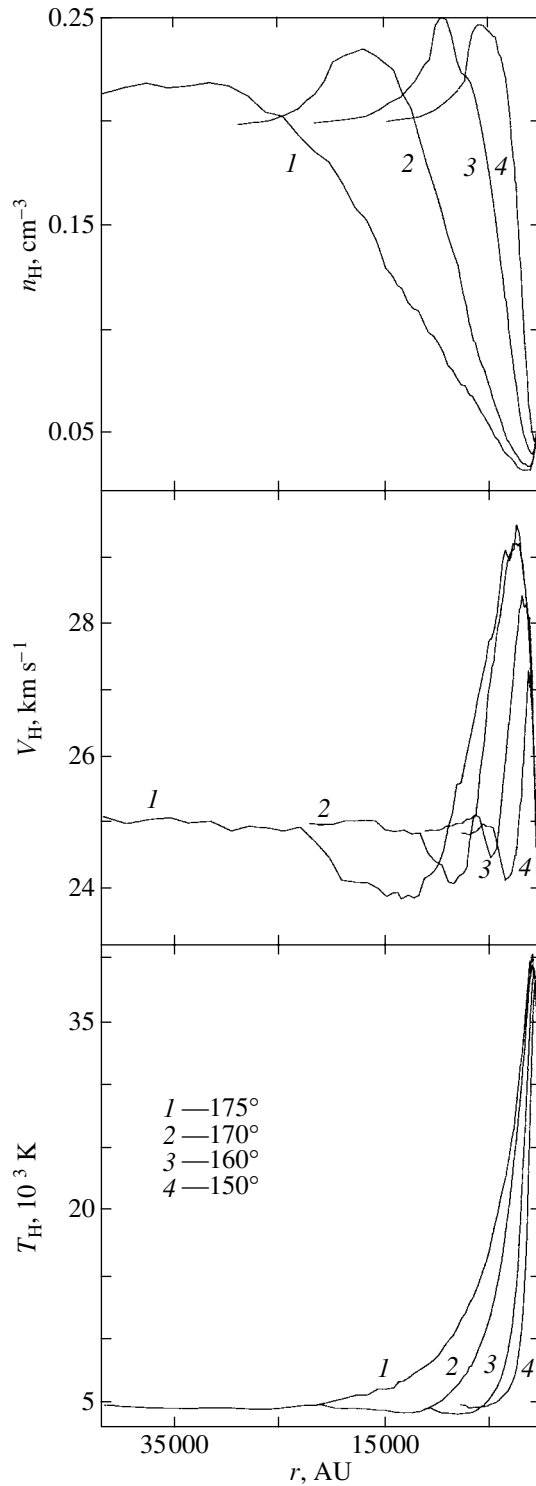
Fig. 4. The density, velocity, and temperature of the interstellar hydrogen atoms along the lines of sight with $\theta = 150°, 160°, 170°, 175°$ vs. heliocentric distance r.

the interstellar hydrogen atoms fill its tail region. The fraction of primary (which did not undergo charge exchange in the heliospheric interface) interstellar atoms increases with heliocentric distance. The temperature (6000 K) and velocity (25 km s^{-1}) of the primary interstellar atoms are lower than the temperature (100 000 K) and velocity (100 km s^{-1}) of the
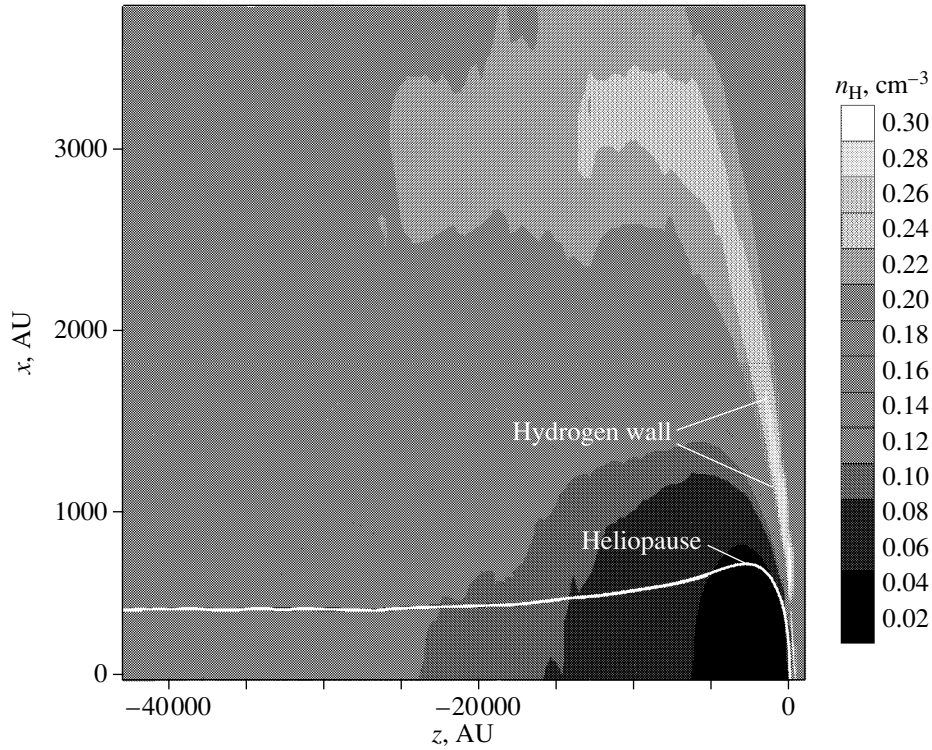
Fig. 5. The two-dimensional density distribution of hydrogen atoms in the heliospheric interface. At heliocentric distances ~40 000 AU, the atomic density is close to its value in the unperturbed LISM. The hydrogen wall, the increase in the density of hydrogen atoms in front of the heliopause, is also seen in the figure. The intensity of the hydrogen wall decreases with increasing heliocentric distance.

post-shock solar wind. Charge exchange produces new protons with lower average and thermal velocities than those of the primary solar protons. Thus, charge exchange leads to the effective cooling and deceleration of the solar wind. Because of the solar wind acceleration by the pressure gradient, on the one hand, and its deceleration by charge exchange, on the other hand, the heliopause is not always parallel to the onflow direction. Since the fraction of primary interstellar atoms increases with heliocentric distance, it would be natural to expect the solar wind velocity, density, and temperature to approach their interstellar values.

Despite many assumptions, the above qualitative analysis is confirmed by our numerical calculations. In the next section, we present and discuss the results of our numerical calculations.

RESULTS AND DISCUSSION

Our calculations confirm the above qualitative analysis. The distributions of plasma parameters in the heliotail region are shown in Figs. 2 and 3. Figure 2 presents the plasma-density and velocity distributions on both sides along the heliopause. In classical hydrodynamics, the conditions at a

tangential discontinuity, which the heliopause is, are (1) the absence of mass transport through the discontinuity and (2) a pressure balance on both sides of the discontinuity. These conditions admit a jump in density and tangential velocity when passing through the heliopause. In the presence of interstellar hydrogen atoms, momentum and energy are transferred between the solar wind and the interstellar medium via charge exchange. Therefore, the jumps in density and velocity become weaker with increasing distance calculated along the heliopause from its nose. At $z \approx -3000$ AU, where z is the distance along the symmetry axis and the minus sign denotes the direction along the LISM flow, the jumps in density and tangential velocity disappear (Fig. 2).

The plasma velocity downstream the termination shock is ≈ 100 km s^{-1}. This velocity then decreases as a result of charge exchange and approaches the interstellar velocity. The solar wind also effectively cools down through charge exchange. The interstellar Mach number is $M \approx 2$. Figure 3 shows isolines for Mach numbers in the heliospheric interface. We see that the solar wind passes through the speed of sound at $z \approx -4000$ AU. The Mach number then increases with distance from the Sun, approaching its interstellar value. The heliopause is also shown in Fig. 3. The

$z = -3000$ AU line indicates the boundary behind which there are no jumps in density and velocity at the heliopause.

Figures 4 and 5 present the distributions of interstellar hydrogen atoms in the heliospheric tail. Figure 4 shows the densities, velocities, and temperatures of the interstellar atoms along various lines of sight. The line-of-sight angle θ in these figures is measured from the LISM onflow direction (Fig. 1). The parameters of the hydrogen atoms approach their interstellar values at distances less than or of the order of 20 000 AU for all lines of sight. The approach is faster for smaller θ. It is also interesting to note that the hydrogen wall, the increase in the hydrogen-atom density in the region between the heliopause and the bow shock (Baranov *et al.* 1991; Izmodenov 2000), is noticeable even at large $\theta \approx 150°-170°$. The two-dimensional distribution of hydrogen atoms in the heliospheric tail is shown in Fig. 5.

Note that charge exchange significantly facilitates the numerical solution of our problem. An importance circumstance is that the solar wind becomes supersonic in the heliospheric tail, which allows us to set proper boundary conditions.

It should also be noted that here, we considered the effect of charge exchange alone. In the future, apart of charge exchange, the effects of various hydrodynamic and plasma instabilities on the flow structure should be considered. The interstellar and heliospheric magnetic fields can also affect the flow structure. Reconnection can be important as well.

CONCLUSIONS

We have studied the effect of interstellar hydrogen atoms on the structure of the heliotail region. In particular, we showed the following:

(1) Neutral hydrogen atoms qualitatively change the flow pattern of the solar wind and the LISM in the tail region via change exchange: the termination shock becomes more spherical and the Mach disk, the reflected shock, and the tangential discontinuity disappear (Fig. 1). The discontinuities, for example, the heliopause, that exist in a purely gas-dynamical solution in the entire tail region become weaker in the solution that takes into account atoms and disappear at distances larger than 3000 AU.

(2) The parameters of the hydrogen atoms, the solar wind plasma, and the LISM in the tail region at distances above 20 000 AU from the Sun approach their values in the unperturbed LISM because of charge exchange. This allows us to estimate the extent to which the Solar System affects the surrounding interstellar medium and, hence, to estimate the Solar System size in the tail region ($\approx 20\,000-40\,000$ AU). In contrast to the nose of the heliospheric interface, the Solar System boundary in its tail region is diffusive in nature.

(3) The effect of hydrogen atoms causes the solar wind to become supersonic with increasing heliocentric distance (from 4000 AU). This removes the difficulties in specifying boundary conditions and makes it possible to obtain a proper numerical solution.

REFERENCES

1. V. B. Baranov and Yu. G. Malama, J. Geophys. Res. **98** (A9), 15157 (1993).
2. V. B. Baranov and Yu. G. Malama, J. Geophys. Res. **100**, 14755 (1995).
3. V. B. Baranov and Yu. G. Malama, Space Sci. Rev. **78**, 305 (1996).
4. V. B. Baranov, K. V. Krasnobaev, and A. G. Kulikovskiĭ, Dokl. Akad. Nauk SSSR **194**, 41 (1970) [Sov. Phys. Dokl. **15**, 791 (1971)].
5. V. B. Baranov, M. G. Lebedev, and Yu. G. Malama, Astrophys. J. **375**, 347 (1991).
6. V. B. Baranov, V. V. Izmodenov, and Yu. G. Malama, J. Geophys. Res. **103** (A5), 9575 (1998).
7. V. V. Izmodenov, Astrophys. Space Sci. **274**, 55 (2000).
8. V. V. Izmodenov, in *Proceedings of the Special COSPAR Colloquium in Honour of Stanislaw Grzedzielski, Leaving Executive Director of COSPAR,* COSPAR Coll. Series (2002) (in press).
9. V. V. Izmodenov, R. Lallement, and Yu. G. Malama, Astron. Astrophys. **342**, L13 (1999).
10. V. V. Izmodenov, M. Gruntman, and Yu. G. Malama, J. Geophys. Res. **106** (A6), 10681 (2001).
11. R. Lallement, Space Sci. Rev. **78**, 361 (1996).
12. Yu. G. Malama, Astrophys. Space Sci. **176**, 21 (1991).
13. M. Witte, M. Banaszkiewicz, and H. Rosenbauer, Space Sci. Rev. **78**, 289 (1996).

Translated by V. Izmodenov

Observational Manifestations of Prerecombination Protoobjects

V. K. Dubrovich[*]

Special Astrophysical Observatory, Russian Academy of Sciences,
Nizhnii Arkhyz, Karachaevo-Cherkesskaya Republic, 357169 Russia
Received November 27, 2001; in final form, July 24, 2002

Abstract—We consider the image formation for an extremely distant source in an optically dense, homogeneous, and isotropic medium. We show that the angular size of the image would presently be $\theta_0 \approx 10'$, irrespective of the initial redshift z. Parameters of the inhomogeneities capable of producing the observed effect were estimated. We note that this effect should be taken into account for the baryon density fluctuations that were damped according to Silk at the prerecombination epoch. The spot radiation spectrum is shown to be a diluted Planckian spectrum with a dilution factor much larger than unity. We also point out the presence of peculiar tangential polarization in the spot, which reaches several tens of percent at the spot edge. All these observational features clearly distinguish the fluctuations under consideration from the standard fluctuations. © *2003 MAIK "Nauka/Interperiodica".*

Key words: *theoretical and observational cosmology.*

INTRODUCTION

The evolution of matter and radiation in the early Universe is accompanied by the various processes of the formation and damping of inhomogeneities and nonequilibria. These include matter density fluctuations at the inflation stage, primordial black holes, various nonuniformities in the distribution of matter and antimatter, strings, and many others (Khlopov *et al.* 2000, 2002; Dubrovich and Khlopov 1989; Polarski and Starobinsky 1994; Singh and Ma 2001; Naselsky and Novikov 2001; Brandenberger *et al.* 2002). Most of these inhomogeneities are local in nature and are small-scale perturbations. Some of the suggested types of perturbations are the so-called mass-compensated ones.

However, caution is needed in this case, because exact compensation can be achieved only at a single instant of time, while the rest of the time, due to the different evolution laws of the energy density for the mutually compensating components, there is a mismatch between their contributions (see, e.g., Naselsky and Novikov 2001). The evolution of the gravitational potential for such a protoobject can be described, for example, by the method of Bashlinsky and Bertschinger (2002).

RADIATIVE TRANSFER

We consider those inhomogeneities which emerge from under the horizon at the epoch of complete matter ionization, i.e., at redshifts $z_i > 10^4$. The fate of

such inhomogeneities has been repeatedly and extensively studied. The general conclusion reduces to the assertion that the energy contained in them dissipates and, hence, all the spatial fluctuations in the CMBR temperature attributable to them are completely absent: the fluctuations are "blurred" (Zel'dovich and Novikov 1975).

The simplest and obvious argument for this conclusion is an estimate of the optical depth τ_T, for example, for Thomson scattering. It becomes much larger than unity even at $z > 1300$ and increases with z (for $z > 10^4$):

$$\tau_T = n_e \sigma_T c t \approx 10^{-2}(1+z), \qquad (1)$$

where n_e is the electron number density, σ_T is the cross section for Thomson scattering by electrons, c is the speed of light, and t is the cosmological time.

However, in a homogeneous and isotropic Universe, it is improper to use the logic of the astrophysics of pointlike objects obscured by an opaque cloud. The point is that in a strongly scattering medium, the photons emitted by a point source cannot move far from the point of their production. Their motion is diffusive; i.e., the velocity of their recession from the center significantly depends on τ and is always effectively lower than the speed of light. The distance R traversed by a photon in time t for a constant n_e is

$$R \approx ct/\tau^{1/2}. \qquad (2)$$

As $n_e \sim 1/t^2$ decreases due to the expansion of the Universe, the photon mean free path increases and

the size of the region where all of the energy released by the source is localized is $R \sim t^{3/2}$. However, R is always smaller than the horizon size. The limiting size is L_0 at the time of hydrogen recombination, when the number of free electrons rapidly decreases and the Universe becomes transparent. The value of L_0 is equal to the mean free path before the last photon−electron collision. Numerical estimates yield $L_0 \approx (0.2−0.15)L$, where L is the horizon size at $z = 1100$. It is easy to see that in this logic, there is no specificity of the different times at which the sources begin to radiate if only this occurs much earlier than $z = 1100$. We emphasize once again that the above assertion is universal with a high accuracy; i.e., it is virtually independent of the details of energy transfer and transformation in the protoobject.

Indeed, let the radiation begin at an epoch with a high matter temperature, when, for example, electron−positron pairs are present in large quantities and the radiation spectrum is very hard. Then, this radiation can heat the surrounding matter, turn into pairs of particles and antiparticles, produce shock waves, or transform into other forms of energy. However, it is clear that none of these transformations allow us to remove the total radiation energy of a protoobject from a limited region around it. If there is a pressure excess in the fluctuation volume, then the hydrodynamic relaxation will proceed at a velocity equal to the speed of sound c_s at a given time. For large z, $c_s = c/\sqrt{3}$. However, in this case, complete thermalization within the perturbed volume can proceed only on long time scales and in a complicated way.

Subsequently, as a result of the cooling of the Universe, the electron−positron pairs annihilate, thereby returning the energy transferred to them, and the shock waves are damped, also giving their energy back to the matter and establishing a local value of their temperature because of its strong interaction with the background radiation. Thus, the entire evolution of the superequilibrium radiation reduces to its thermalization in a small region centered at the initial fluctuation position. This most likely occurs at $z \approx 10^8$ and the subsequent evolution will be purely diffusive. By this time, the radius of the region where the object energy is localized may significantly depend on the evolutionary track. However, it is clear that in any case, the radius is much smaller than the local horizon size and, hence, it does not affect the final (at $z = 1100$) size of the observed spot.

INTENSITY

The intensity I_0 in the spot is determined by the part of the energy that is transferred to photons. In principle, it depends on z_i because of photon reddening. The photon diffusion for a rapidly varying mean free path requires a special analysis. One may apparently expect a distribution of intensity I in spot radius r of the type

$$I = I_0 \exp(-r^2/2L_0^2). \qquad (3)$$

As was said above, L_0 does not depend on z. The specific I distribution also depends on the pattern of variations in the object luminosity with time. Clearly, for a variability times scale (recalculated for z) shorter than the photon mean free time, the distribution $I(r)$ is different.

Let us estimate I_0 for given initial fluctuation parameters I_i and R_i. First, note the obvious fact that if the expansion of the region occupied by an excess of photons follows the exact Friedmann law

$$R_F = R_i(1 + z_i)/(1 + z), \qquad (4)$$

then the deviation of the photon temperature in this region relative to the CMBR does not vary with time. This is due to the simultaneous "correct" variations in the photon frequency and number density. The quantity $\delta T/T$ varies with time, because there is a mismatch between the rate of change in the volume occupied by the fluctuation and the rate of photon reddening. The former is determined by the non-Friedmann component of the fluctuation expansion velocity because of diffusion (R_d) and the sound wave (R_s). The fluctuation radius R is

$$R = R_F + R_d + R_s. \qquad (5)$$

All three terms in this expression are functions of time. However, we are primarily concerned with their values at the time of the last scattering. Without going into details, we can assert that R_s is much smaller than $R_d = L_0$. Using this fact, we can easily estimate the final value of $\delta T/T$ due to the change in the protoobject surface area with the correct change in photon frequency:

$$\delta T_0/T \approx \delta T_i/T (R_F)^2/(R_F + L_0)^2. \qquad (6)$$

A detectability level $\delta T_0/T \approx 10^{-7}$ allows us to "see" a protoobject with an initial amplitude of, for example, $\delta T_i/T \approx 0.1$ and a size $R_F \approx 10^{-2}L_0$. Using expression (4), into which we must substitute z corresponding to the last photon collision, i.e., $z \approx 1000$, we obtain

$$R_i \approx L_0/(1 + z_i) \approx 3 \times 10^{22}/(1 + z_i) \text{ cm.} \qquad (7)$$

The size of the local horizon L_i is $\approx 10^{30}/(1 + z_i)^2$ cm and the object size becomes equal to it at $z = 3 \times 10^8$. This circumstance imposes no bans on z_i. The situation when $R_i > L_i$ is also possible. It only requires that condition (7) be satisfied. Note also another obvious fact: the regular spherical shape of the spot (as well as its main size L_0) is formed during the last collisions between diffusing photons. Therefore, the

form of the initial fluctuation intensity distribution (at $z = z_i$) when condition (7) is satisfied plays no role. Clearly, the initial asphericity is suppressed by a factor of $\sim R_F/L_0$.

SPECTRUM

A more detailed analysis of this process leads us to yet another important conclusion. The photon energy spectrum is not Planckian. This is a direct result of the non-Friedmann law of variation in the fluctuation-region radius. Indeed, the Planckian spectrum unambiguously determines the position of the intensity peak and the photon number density. In our case, however, the photon-frequency variation is determined only by the general expansion of the Universe, while the density variation is determined by a specific (non-Friedmann) expansion law of the perturbed region. This difference shows up most clearly at the last step when, because of the rapid decrease in the density of free electrons, the photon mean free path and, accordingly, R change by several factors as the photon frequency changes by $10-15\%$. A similar situation takes place in the envelopes or nebulae around stars.

The resulting spectrum is a diluted Planckian spectrum: this is a standard Planckian spectrum in which all photon frequencies do not change and the photon number density at all frequencies was reduced by the same factor. In this case, the color temperature of the radiation depends on frequency. More specifically, it is almost constant in the Rayleigh–Jeans region and the dependence is logarithmic in the Wien wing.

The spectrum of the observed spot could be determined by yet another factor. If the initial fluctuation is formed at $10^{10} > z > 10^4$, the thermalization of the superequilibrium radiation is incomplete (Sunyaev and Zel'dovich 1970; Illarionov and Sunyaev 1974a, 1974b). In the range $10^8 > z > 10^5$, the radiated energy transforms into the so-called μ disturbances. For even lower z, the observed spectrum is roughly the same as that at the time of its production with small so-called y disturbances. In both cases, there is also dilution.

Such sources must be, in particular, small-scale fluctuations in the matter density damped according to Silk. Actually, in this case, the peculiar velocities of primordial sound waves with small wavelength are damped. Clearly, the energy of these waves transforms into the heating of matter and photons, but it will again be unable to go far from the place of its generation. The contribution of this process to the spatial CMBR fluctuation spectrum is determined by the statistical summation of spots of identical sizes with random coordinates of their centers and with certain intensities. The separations between the spot centers and their intensities correspond to a set of damping harmonics l. However, the final result significantly depends on the initial power spectrum in the range of small scales.

POLARIZATION

An important consequence of the process considered is a peculiar polarization pattern of radiation in the spot. For point symmetry, scattering by electrons yields tangential polarization: the electric vector is perpendicular to the spot radius. The degree of polarization monotonically increases from zero at the spot center to $\sim 80\%$ at its edge, irrespective of the spot angular size.

CONCLUSIONS

Below, we summarize our main conclusions. In the presence of large temperature fluctuations or small-scale entropy inhomogeneities at early (pre-recombination) evolutionary stages of the Universe,

—a proper allowance for multiple scattering gives rise to spots of identical sizes in the observed CMBR intensity distribution; at the epoch of hydrogen recombination, this scale is $\theta \approx 10'$;

—the radiation spectrum in these spots is essentially non-Planckian;

—the radiation in a spot has a strong tangential polarization.

Naturally, to verify these conclusions by observations, a more detailed analysis of all the above model assumptions and detailed numerical calculations are required.

REFERENCES

1. S. Bashlinsky and E. Bertschinger, astro-ph/0202215 (2002).
2. B. H. Brandenberger, B. Carter, and A.-Ch. Davis, hep-ph/0202168 (2002).
3. V. K. Dubrovich and M. Yu. Khlopov, Astron. Zh. **66** (2), 232 (1989) [Sov. Astron. **33**, 116 (1989)].
4. A. F. Illarionov and R. A. Sunyaev, Astron. Zh. **51**, 698 (1974a) [Sov. Astron. **18**, 413 (1974a)].
5. A. F. Illarionov and R. A. Sunyaev, Astron. Zh. **51**, 1162 (1974b) [Sov. Astron. **18**, 691 (1974b)].

6. M. Yu. Khlopov, S. G. Rubin, and A. S. Sakharov, Phys. Rev. D **62**, 083505 (2000).
7. M. Yu. Khlopov, S. G. Rubin, and A. S. Sakharov, astro-ph/0202505 (2002).
8. P. Naselsky and I. Novikov, astro-ph/0112247 (2001).
9. D. Polarski and A. Starobinsky, Phys. Rev. D **50**, 6123 (1994).
10. S. Singh and C.-P. Ma, astro-ph/0111450 (2001).
11. R. A. Sunyaev and Ya. B. Zel'dovich, Astrophys. Space Sci. **7**, 3 (1970).
12. Ya. B. Zel'dovich and I. D. Novikov, *Structure and Evolution of the Universe* (Nauka, Moscow, 1975).

Translated by G. Rudnitskii